Design and Performance of a Two Arm Wire Chamber Spectrometer for Use at the Manitoba 50 MeV Cyclotron.

A thesis submitted to the Faculty of Graduate Studies in partial fulfilment of the requirements for the degree of Doctor of Philosophy.

by

Joseph McKeown

University of Manitoba, Winnipeg.

March, 1970.

ABSTRACT

A wire chamber spectrometer connected on-line to a PDP-9 and an IBM 360/65 computer has been developed to study (p,2p) reactions at incident energies in the range 30-50 MeV. It consists of two pairs of wire chambers, one pair on each side of the incident beam. Outgoing protons are detected in coincidence in large plastic scintillation counters, subtending solid angles as large as 0.16 sterad. at the centre of the target. As the events arrive, the PDP-9 calculates the proton trajectories and projects them into the target volume. When a gaseous target is employed so that the reaction volume is long in the beam direction, most chance coincidences and slit-scattered protons are rejected by testing for an event vertex. If a vertex is made, then the event pulse heights and coordinates are sent to the IBM 360/65, where the full kinematic analysis is performed.

For a pair of 21.0 MeV outgoing protons the energy resolution of the undetected third particle is 1.5 MeV HWHM and the angular resolution of each arm is 0.32^{o} HWHM. From the data collected during a test run preliminary results are presented on the application of the spectrometer to a study of the D(p,2p)N reaction and the proton-proton bremsstrahlung process.

ACKNOWLEDGEMENTS

The extent of this work was such that the combined effort of many people was necessary to bring the spectrometer to operational status. Detailed description of the work carried out mainly by others has been eliminated from this thesis but reasons of coherence have necessitated a review of some work which is not entirely my own.

I am particularly grateful for the guidance and enthusiasm of my advisor Prof. J. V. Jovanovich whose encouragement and active participation in all general aspects of the experiment made it a success.

Prof. K. G. Standing was actively involved during the design stages of the experiment. He gave me much useful advice with the initial interface design and he also worked in close collaboration with Mr. E. Lipson, who wrote the preliminary version of the VERTEX program.

Dr. J. C. Thompson designed and supervised the construction of the wire chambers and wrote much of the associated PDP-9 software. Drs. W. K. Prickett and S. Suen assisted during the final stages of spectrometer calibration.

Mr. L. G. Greeniaus wrote the CORRELATE program and together we shared the burdens of software debugging with both computers and off-line analysis of data from pre-

liminary runs. Many useful ideas grew from our frequent discussions on the spectrometer performance.

Messrs. T. Millar and D. G. Peterson gave vital assistance during cyclotron runs.

Messrs. D. Reimer, R. Kawchuk, R. King and P. O'Conner assisted in general software development both at PDP-9 and 360/65 level.

The technical support of the cyclotron staff and machine shop is greatly acknowledged. Special mention must be made of the cooperation and help so freely given by the personnel of the electronic laboratory working under the direction of Mr. G. Knote. We are particularly grateful for the skilful work done by Mr. A. Neufeld during wire chamber construction and slow electronics development.

The patient support of my wife, Paddy, made the publication of this thesis possible.

The encouragement of the Cyclotron Director, Prof. K. G. Standing, together with the financial support of the Atomic Energy Control Board are gratefully acknowledged.

TABLE OF CONTENTS

LIST OF TABLES

LIST OF FIGURES

INTRODUCTION

A fundamental problem in nuclear physics is the precise nature of the interaction between two nucleons. The theory is simplified if we assume that the interaction may be described by a potential. The task of defining the phenomenological nuclear potential involves the acquisition of large amounts of very precise nucleon-nucleon elastic scattering and bound state data. These experiments measure such quantities as the total and differential cross-sections, polarizations, correlation coefficients and triple scattering parameters, making possible the construction of a reasonably unique set of phase shifts which fit the data [1]. Phenomenological potentials which are quite different in character (momentum-dependent, hard core, separable etc.) may fit the phase shifts well, but a more critical demand must be imposed if a potential is to be found which more precisely describes the nucleon-nucleon interaction.

The analysis of elastic scattering data yields only information about the p-p interaction "on the energy shell". However, nuclear physics calculations involving the two nucleon interaction generally involve off-energy shell elements of the transition matrix. A determination of all of the on-shell matrix elements by high precision

elastic scattering experiments will still not completely determine the off-shell amplitude.

If a particular nuclear process involves matrix elements which are strongly off-energy-shell, then theoretical predictions for that process will be model dependent. Inelastic scattering between nucleons below the meson threshold is restricted to nucleon-nucleon Bremsstrahlung and the difficulty of working with neutrons has restricted the main experimental effort to the reaction

$$p + p \longrightarrow p + p + \gamma$$

which is known as proton-proton bremsstrahlung (PPB). The main interest in PPB a few years ago was to use this process to remove the degeneracy of the phenomenological potentials on the energy shell. The unforeseen difficulties with theory and experiment show that the fundamental nature of PPB demands a more general interpretation in which elastic scattering will be a limiting case. The primary motivation for undertaking this work was to investigate the PPB reaction in detail and to improve the statistical accuracy of existing measurements[2,3,4] near 45 MeV.

In 1963 Sobel and Cromer[5] showed that the cross sections for PPB were large enough to make a measurement possible and experimental results were first reported by B. Gottschalk et al.[6]. Many observations of the PPB process have since been made and all have detected the

two final state protons in coincidence telescopes which determine their energy and define their direction. The gamma ray is not detected (although a gamma ray detector was used in Gottschalk's first experiment). The experiment performed by Warner[2] is a typical example of this approach. Rothe et al.[7] performed an experiment quite different in character by using spark chambers and a gamma ray detector at 204 MeV to kinematically over-determine each event.

A major problem with all of these experiments is associated with the difficulty of isolating PPB events from background events. Real coincidences arise from elastically scattered protons which are rescattered before entering the detectors. Also competing (p,2p) reactions give real coincidences from outgoing protons with energies falling within the PPB region. Accidental coincidences arising from independent scattering events can be rescattered to appear in the detectors as PPB events. Pulse height selection by a pair of ΔE counters provides incomplete discrimination against elastic protons which give abnormally low pulse heights due to nuclear reactions in the plastic scintillators. The target thickness and beam current must therefore be kept at a level which allows separation of random coincidences from real events. This has restricted the observed PPB event rates to a few per hour.

In our experiment, where two wire chambers separated by a short distance define the proton trajectory, a large solid angle is responsible for an increase in the event rate. At the same time good geometric and energy definition is maintained. Background is rejected by demanding that both outgoing protons originate from a common vertex within the reaction volume. Kinematic analysis on an event by event basis permits the definition of a "goodness of fit" parameter related to the measured spectrometer properties. This is used to improve background rejection.

In the more conventional experiment where the proton directions are constrained and the proton energies are the only free parameters, almost complete feedback is available to the experimenter in the form of the two dimensional energy spectrum. This feedback is essential for experiments lasting for hundreds of hours. With large solid angles there are many free parameters and a high level of on-line computational power must be available if meaningful feedback is to be provided. The spectrometer to be described uses a PDP-9 computer, programmed in machine language, to select events which are good candidates for a full kinematic analysis to be performed on-line by the University of Manitoba IBM 360/65. During data-taking runs the information returned from the 360 provides the experimenter with an immediate

quantitative picture of the quality of the accepted data.

During the last few years interest has been developing in quasi-free proton-proton scattering for shell model studies of nuclei. By combining energy and angular selection of the outgoing proton pairs information on the momentum distribution of the protons in individual shells can be obtained. In addition, the summed energy spectrum of the emerging particle pairs is expected to show peaks at the separation energies corresponding to the various nuclear shells. These (p,2p) reactions generally have small cross sections and experimentally they present very similar problems to PPB experiments. Therefore, this spectrometer can be used to study (p,2p) reactions where the energy separation between levels is more than a few MeV.

The work described in this thesis gives a new approach to the experimental study of processes involving two outgoing protons in the final state. In addition, the results presented establish the feasibility of application of the system to a study of some (p,2p) reactions and in particular the PPB process at 45 MeV.

CHAPTER I

Design Criteria.

General Considerations.

In 1966 when the basic principle of the experiment was conceived, experiments at Brookhaven [8] had clearly demonstrated the applicability of an on-line wire chamber spectrometer to analyse particles of 5 to 30 BeV/c momentum. Our system makes use of the very considerable experience gained from those developments and much of our high voltage [9] and read out electronics [10] exist in only slightly modified form*. Nevertheless, the physical and technological problems in bringing a spectrometer, conceived for the 75-300 MeV/c range, to operational status were formidable and in this chapter some of these design considerations are discussed.

1.1 Environmental Problems.

(a) Effect of hydrogen gas close to the wire chamber.

The requirements to have large solid angle, small energy loss and multiple scattering of the outgoing protons in the target gas, demand that the wire chambers are located as close as possible to the target volume.

* We are grateful to Dr. J. C. Fisher and Dr. W. A. Higinbotham for advice and help given to Dr. J. C. Thompson during his stay at Brookhaven National Laboratory.

This creates a stringent environmental problem as the chambers must operate close to a primary beam of more than 10^{10} protons per second passing through a gaseous target. The general layout of the spectrometer is shown in Fig.II.2 and will be described in detail in Chapter II.

Protons from p-p elastic scattering in hydrogen gas produce a calculated flux of 4×10^4 protons/sec/nA through the front chamber and subsequent measurements have confirmed this value. Also electrons (delta rays) from elastic scattering of protons with the orbital electrons of the target gas are created in copious quantities. The number of delta rays with scattered energies greater than 50 KeV, all of which are able to reach the front chamber, when using H_2 gas as a target, is estimated to be much higher than the scattered proton flux.

(b) General Room Background.

Electrons from the radiation background existing in the experimental area will create charges inside the wire chambers. The gamma ray sensitivity of wire chambers was unknown and when designing our transport system it was difficult to predict the gamma ray level to be expected in the experimental area. Large solid angles demand the use of large scintillation counters and background, particularly fast neutrons produced by stopping the primary beam in the Faraday Cup might result in excessive sparking

of the wire chambers.

(c) Slit Scattering.

In addition to the background produced by the above physical processes, environmental problems were to be expected at small scattering angles from protons scattered from slits. Protons entering the scattering chamber, which have been deflected by multiple scattering in the HAVAR FOIL (see Fig.II.2) and rescattered into the wire chambers from the baffles defining the reaction volume, are potentially troublesome. This places a heavy responsibility on the beam transport design and its directional stability.

1.2 Wire Chamber Hodoscope.

The design of a wire chamber hodoscope for outgoing protons with energies around 10 MeV presents quite different problems from those at higher energy. A compromise must be reached in the design characteristics imposed by the following four design requirements.

(a) Low Energy Loss.

If low energy protons are to be observed the wire chambers must have very low mass. This demand imposes a limit on the number of wire planes which can be used and restricts the choice of construction materials to

extremely thin and correspondingly fragile foils. This in turn creates problems of containment and gaseous diffusion between the target gas, wire chamber gases and air.

(b) Angular Resolution.

The angular definition of the scattered proton track is important, as the angles of the outgoing protons must be known accurately for complete kinematical determination of the event. This restricts the mass of the scattering material which can be tolerated close to the reaction volume.

(c) Vertex Criteria.

In previous PPB experiments the data-taking rate was restricted by random background. An important characteristic of our hodoscope design is the region of vertex uncertainty, as this is a measure of the ability of the spectrometer to reject random events by this method. Multiple scattering, the spacing of the chamber wires and the distance between the chambers all contribute to this uncertainty.

(d) Low Redundancy.

It is apparent from consideration of the number of 'pile up' tracks produced by elastically scattered protons that a system for handling double tracks is vit-

ally necessary. This requires a third plane to determine unambiguously each coordinate and demands that each plane has a good double track efficiency. Enclosing the three planes within a single gas envelope helps to satisfy the requirement of low mass. However, for events having double tracks in one hodoscope there is zero redundancy left in our system i.e. all planes in that hodoscope must fire if a recognizable pattern is to be made. Under these conditions the total hodoscope efficiency, $\mathcal{E}_H$, is very sensitive to the plane efficiency, $\mathcal{E}_p$, and this will fall off exponentially with the number of planes n i.e. $\mathcal{E}_H = \mathcal{E}_p^n$. In the practical case a plane efficiency of 99% would result in $\mathcal{E}_H$ = 94%, while plane efficiencies of 95 or 90%, which are acceptable in spark chambers, result in $\mathcal{E}_H$ of only 74% and 53% respectively. Wire chamber hodoscopes designed for these energies must necessarily place a heavy responsibility on plane efficiency.

1.3 Energy Determination.

The energy of the outgoing protons is determined by depositing all of their energy in the scintillators. This is necessary if the kinematics of the event are to be determined. Also, to avoid triggering of the wire chambers on all random elastic events, triggering by selection on particle energies is highly desirable. Neither of these requirements have been encountered previously

with wire chambers, as scintillation counter outputs normally only provide timing signals and momentum determination is done magnetically.

There are three main problems to be solved :-

(a) With large area scintillation counters the raw energy resolution can be expected to be poor. To take advantage of the expected geometric resolution of the spectrometer this would have to be greatly improved.

(b) Fast pulse height analysis is necessary for selective triggering.

(c) The energy information in the pulse height must be preserved in the presence of noise generated by sparks from the wire chambers. In order to achieve good plane efficiency every effort is made to trigger the chambers as soon after event selection as possible and this does not allow time for the pulse heights to be amplified and digitized. A scheme for the isolation of this analog information must therefore be devised.

1.4 Computer Organisation.

There are many ways in which the raw spark data can be analysed. For instance, in the system at Brookhaven [8] the read out hardware was designed to find the flipped cores as quickly as possible and present their locations as binary address numbers to the PDP-6 computer as an 18-bit word. The computer performed on-line calcul-

ations of kinematics and cross sections from this data. In the Liverpool system described recently [11] control is maintained exclusively by hardware and all processing is done off-line. We have used a two computer system as an integral part of the spectrometer design and our hardware performance, data reduction and analysis is supervised on-line by software.

The role of the two computers is complementary. The principal role of the PDP-9 is to collect and preprocess data at bit level, to output the results or send them for further processing to the 360/65. The 360/65 computer then operates on the data, records results on magnetic tape and returns a sample of the results to the PDP-9. The types of output provided on-line by the PDP-9 are basically only those which meet the physicist's immediate needs.

From the discussions in this chapter it is evident that the design of a wire chamber spectrometer for use at intermediate energies presents some unique and interesting experimental problems. The next chapter describes the approach made towards the solution of some of these difficulties.

CHAPTER II

Experimental Arrangement.

2.1 Beam Transport.

The proton beam used by the experiments described in this work was provided by the University of Manitoba sector-focused cyclotron [12]. Hydrogen negative ions were accelerated to an energy in the range 25 MeV-45 MeV depending upon the position of an Al_2O_3 stripping foil 1.5×10^{-5}cm thick and were guided into an evacuated beam pipe by a correspondingly adjusted combination magnet adjacent to the cyclotron main magnet.

Fig.II.1 shows the general lay out of the beam transport system used in the PPB experiment. The first quadrupole pair (Q_1 and Q_2) situated about 4ft from the cyclotron exit port makes a horizontal focus at the first set of slits S_1 which are typically 2mm wide and 25mm high and a vertical focus in the middle of quadrupole singlet (Q_4). This quadrupole (Q_4), together with the switching magnet, makes a horizontal focus at the second set of slits (S_2), which are also typically 2mm wide and 25mm high. The bending magnet (BM) performs energy selection on the raw beam and the selected beam passes into the experimental area. The magnetic field of the bending magnet, which is measured using an NMR probe, was calibrated using time of flight methods to yield the beam energy

Figure II.1

The cyclotron experimental area showing the beam transport system for the proton-proton bremsstrahlung experiment. Details of other beam lines are not shown.

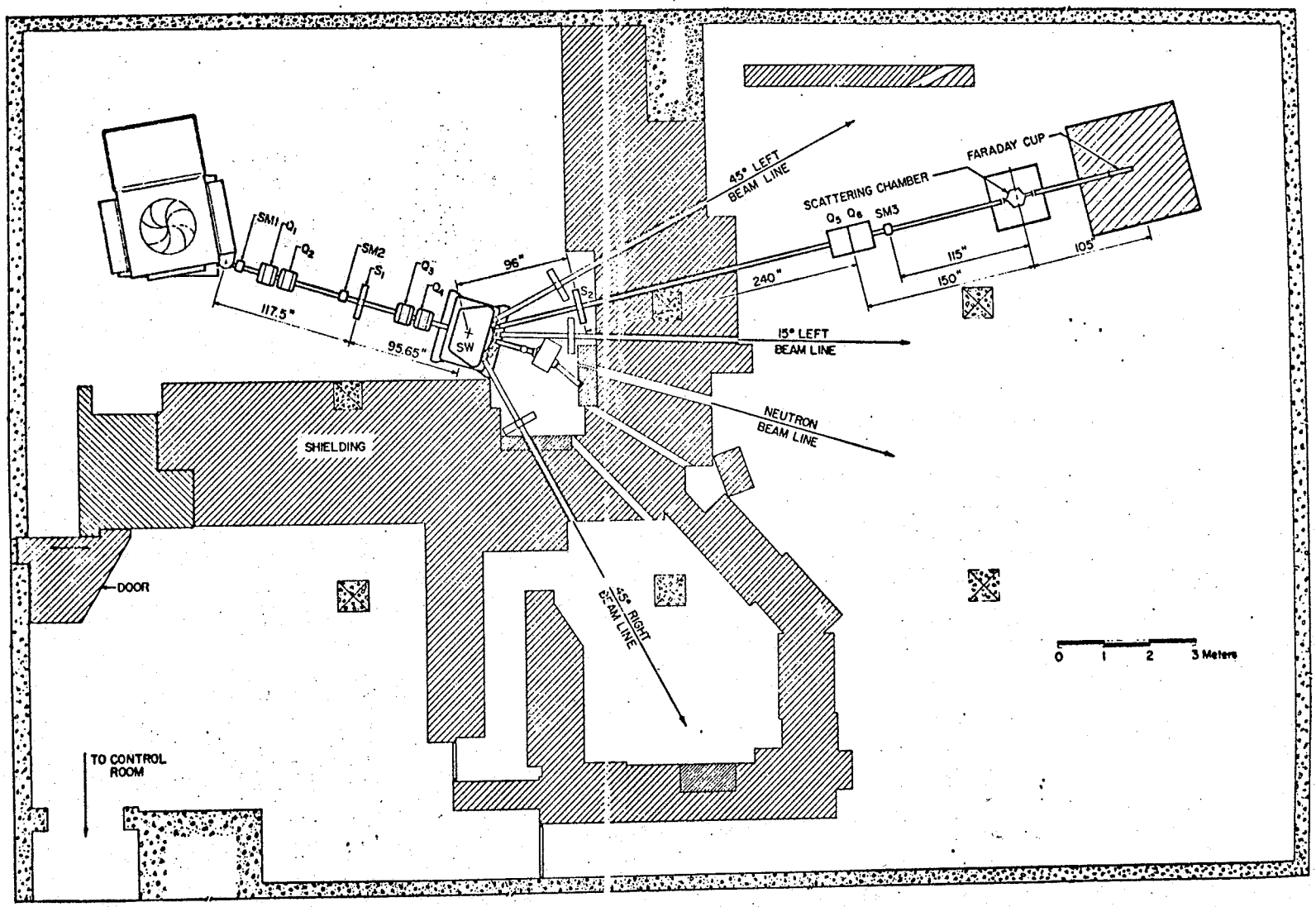
SM1
Q_1
Q_2
SM2
S_1
Q_3
Q_4
96"
117.5"
95.65"
SW
S_2
45° LEFT BEAM LINE
SCATTERING CHAMBER
FARADAY CUP
Q_5 Q_6 SM3
240"
115"
150"
105"
15° LEFT BEAM LINE
NEUTRON BEAM LINE
SHIELDING
DOOR
45° RIGHT BEAM LINE
TO CONTROL ROOM
0 1 2 3 Meters

passing through the analysing slits S_2. The energy resolution achieved was estimated to be 300-400 KeV at FWHM.

The final quadrupole doublet (Q_5 and Q_6) produces a ribbon beam 2mm wide (broadened by multiple scattering in the HAVAR FOILS) and 4 cm high in the scattering chamber. During the measurements reported in this work the steering magnet (SM) was adjusted manually before a run, but more recently dynamic control has been provided by BEAM POSITIONING COUNTERS allowing the PDP-9 to precisely steer the beam through the scattering chamber[13]. Ten feet further downstream is the heavily shielded Faraday Cup for beam current measurement. The beam current used for spectrometer development and cross section determination was in the range 5×10^{-12}A to 10^{-8}A.

The transport system is designed in such a way that unwanted beam is not deposited on any slits within the experimental area. With each scintillation counter having a volume of 81 cubic ins., a high level of neutron and γ ray background would produce too many unnecessary firings of the wire chambers. Also secondary interactions on the slits could produce a large flux of charged particles through the chambers if these slits are close to the chambers.

The beam profile at various stages along the transport system was observed on a series of zinc sulphide screens. Particular interest was directed to the shape

of the beam inside the scattering chamber and this was investigated with a zinc sulphide screen, the beam positioning detectors mentioned above, colouring of perspex plates, scattering of protons from stainless steel wire probes and finally the wire chambers themselves. Detailed results of these investigations will be given elsewhere [13].

2.2 Scattering Chamber and Hodoscopes.

The main features of the spectrometer are shown in Fig.II.2. The scattering chamber is normally filled with target gas at atmospheric pressure. The nuclear interaction takes place in a 17cm long ribbon-like reaction volume defined by the beam profile and the upstream and downstream baffles positioned to intercept only scattered protons. Each of the two outgoing protons pass through two wire chambers defining their trajectories and into plastic scintillation counters where their energies are determined. The scattering chamber, which may be seen in the centre of the photograph Fig.II.3 and in more detail in the photograph Fig.II.4, was made with six flat sides to allow the wire chambers to be moved around thereby permitting investigations in the polar angular range 12^{o}-168^{o}. The solid angle subtended by the rear chamber is usually determined by the requirements of the reaction undergoing investigation. The range extends to an upper limit of 0.55st. in the special case when the outgoing particles

Figure II.2

Scale drawing of the spectrometer showing scattering chamber, wire chambers and scintillation counters. The chamber is filled with the investigated gas (hydrogen at present) at atmospheric pressure. Propane and He jackets are used to separate the Ne-He mixture from the target gas and to decrease multiple scattering.

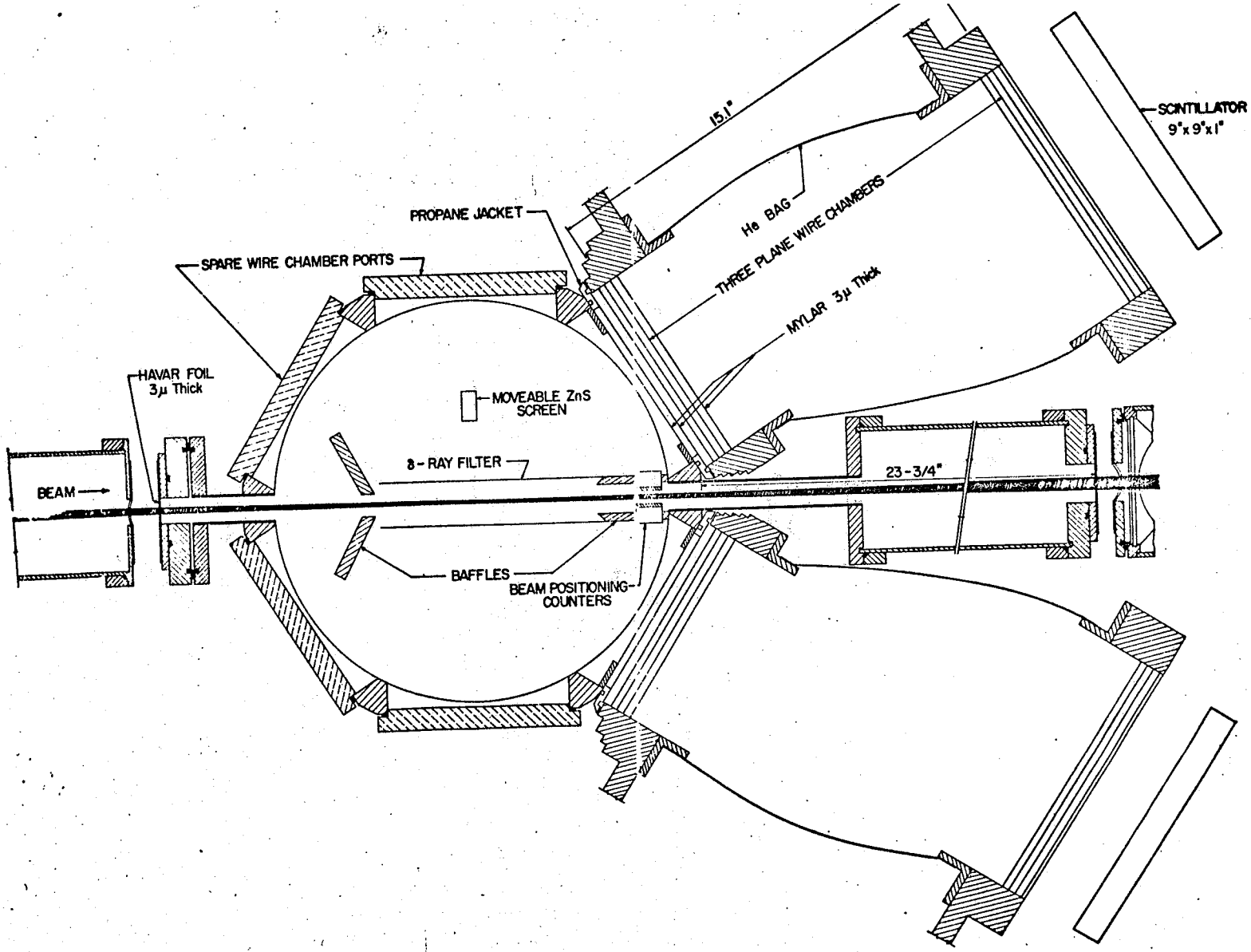
15.1°
SCINTILLATOR
9"x 9"x 1"
He BAG
THREE PLANE WIRE CHAMBERS
MYLAR 3μ Thick
PROPANE JACKET
SPARE WIRE CHAMBER PORTS
HAVAR FOIL
3μ Thick
MOVEABLE ZnS
SCREEN
β - RAY FILTER
23-3/4"
BEAM
BAFFLES
BEAM POSITIONING
COUNTERS

Figure II.3.

Photograph of the spectrometer hardware taken from a position close to the quadrupole pair, Q_5 and Q_6, in Fig.II.1. The beam coming from the left enters the scattering chamber just to the left of the centre of the picture. The high voltage pulsers and core driver boards for the front right wire chamber may be seen mounted on the vertical aluminum plate at the centre of the picture. Some of the fast electronics and read-out electronics are shown on the rack at the extreme right.

Figure II.4.

Photograph of the inside of the scattering chamber taken from above. The beam enters from the bottom right, passes through the mylar trough, which acts as the delta ray filter and leaves at the top left. The opening presented by the front right chamber can be clearly seen. The white object close to the downstream baffles is the light pipe of one of the beam positioning detectors which are mounted on 2" photomultipliers seen as black vertical cyclinders. The top corner of the movable ZnS screen may be seen just below the centre of the picture.

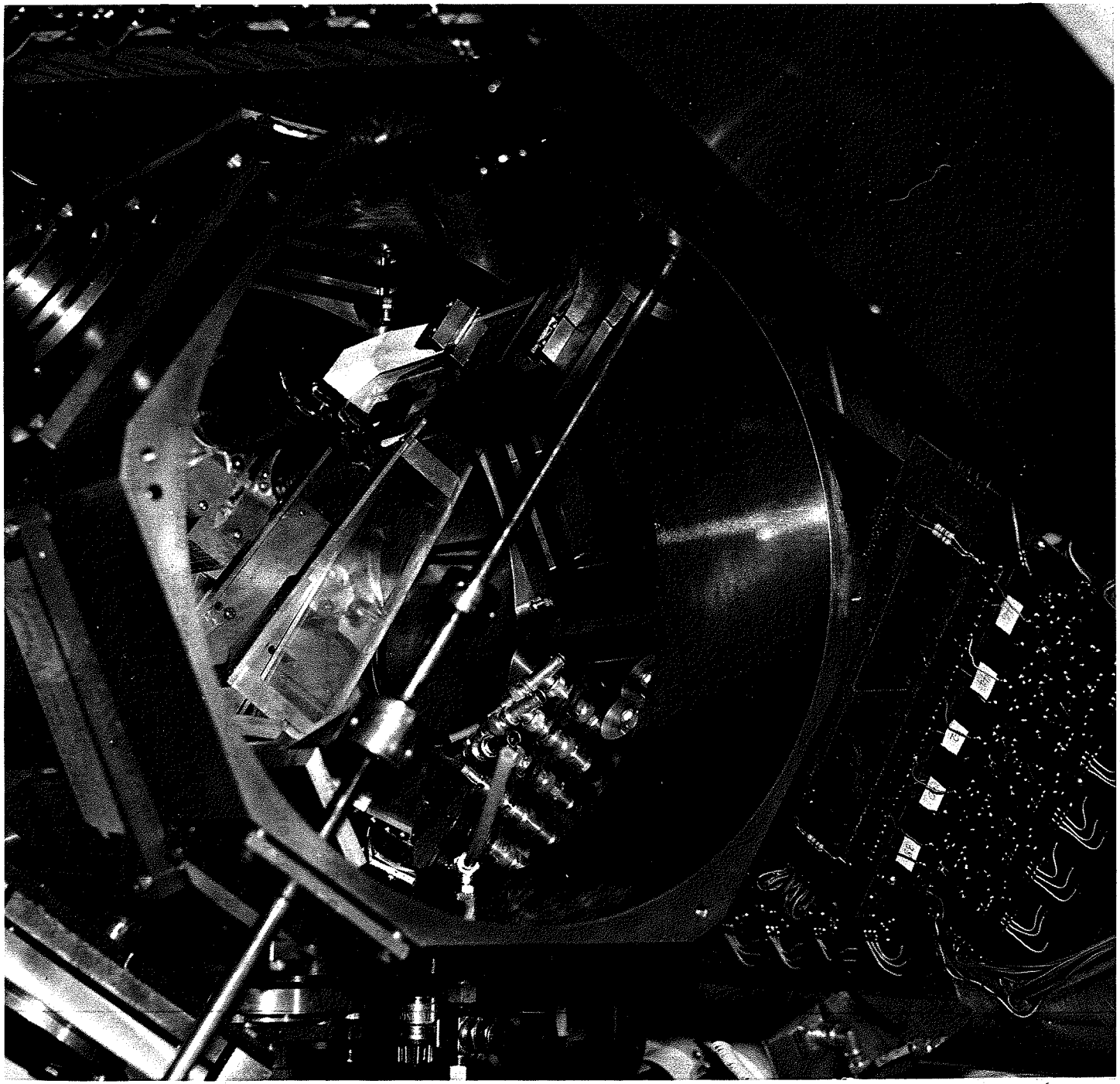

from a solid target are viewed with the front chamber only. Fig. II.2 shows the position of the wire chambers used during the development and testing of the spectrometer. For the same geometry Fig.II.5 gives the relative length of the target volume as a function of the scattering angle, θ, and the azimuthal angle, ϕ.

As it is desirable to reduce multiple scattering of the primary proton beam to a minimum, 3μ thick HAVAR FOILS are used to isolate the cyclotron vacuum from the chamber gas. The foils cover openings 3" x 0.9" and the beam line is broken, as shown in Fig.II.2, at the scattering chamber in order to protect the wire chambers from possible foil fracture.

2.3 Wire Chambers.

(a) Construction.

The spectrometer uses two wire chamber hodoscopes each consisting of two wire chambers specially designed for operation with fluxes of low energy protons. Low mass has been an over-riding design consideration in order to minimise energy loss and multiple scattering. Fig.II.6 shows that the lower energy cut-off limit of the spectrometer for protons is only a few MeV. When the delta ray absorber shown in Fig.II.2 is not in place the principal contribution to the angular resolution comes from multiple scattering in the front chamber. Fig.II.6 shows the var-

iation in the root mean square of the projected angle with energy to be expected with and without a 0.002" thick delta ray filter.

Each wire chamber was built with three planes, a common ground electrode and two high voltage electrodes all made from strung wires. Ferrite core read-out is used with the core contents directly transferred into the PDP-9. The techniques used were essentially those developed at Brookhaven [9,10] and a detailed description of the design parameters together with the essential methods used in the construction of the four wire spark chambers may be found elsewhere [14].

Each plane in the two front chambers was strung with copper coated (7% by weight) tungsten wires, 2 mils in diameter and spaced at intervals of 50 mils. The central ground plane, henceforth called the diagonal plane, was oriented at an angle of 45° to the horizontal plane and was separated by $\frac{1}{4}$" from the high voltage planes strung with horizontal and vertical wires. The wires were strung by hand on fibre glass frames and the frames were glued together. The wire chamber assembly was contained within a gas envelope having mylar entrance and exit windows 0.15 mils thick. The larger rear chambers were constructed in a similar way although here 3 mils thick aluminum wires with a Zn-Cu-Au coating (7% by weight) were used. In order to overcome diffusion the thickness

Figure II.5

Angular ranges resulting from the geometry shown in Fig.II.2.

Curve (a) gives the relative length of the target, called geometric efficiency, plotted as a function of the polar scattering angle, θ. The maximum target length was chosen to be 15cms, with the centre of the scattering chamber acting as the target centre.

Curve (b) gives the geometric efficiency as a function of the azimuthal angle, ϕ.

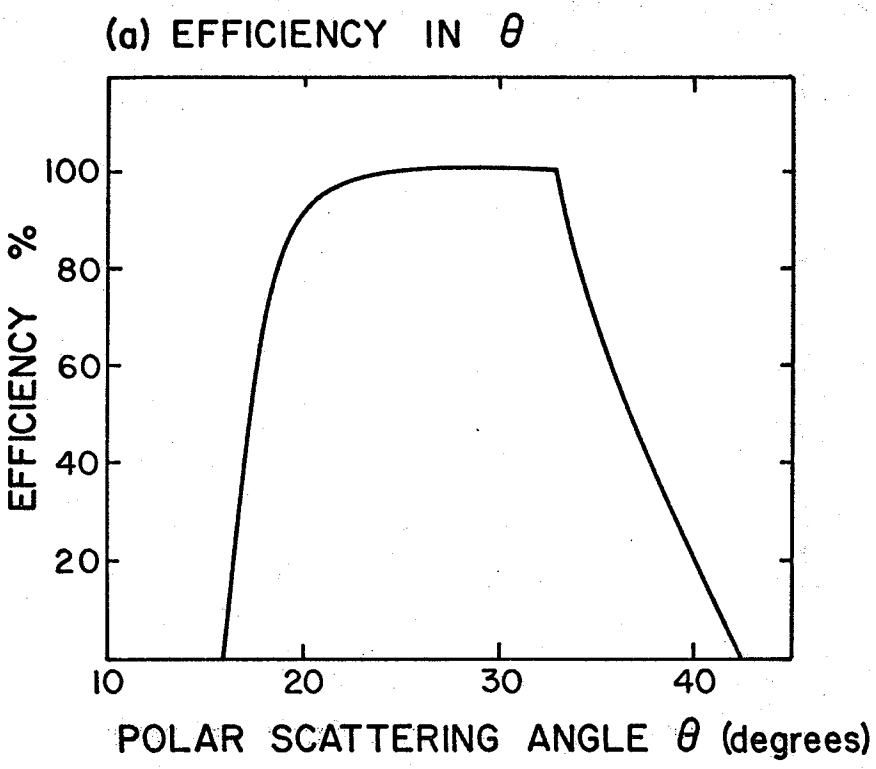
(a) EFFICIENCY IN θ
EFFICIENCY %
100
80
60
40
20
10
20
30
40
POLAR SCATTERING ANGLE θ (degrees)

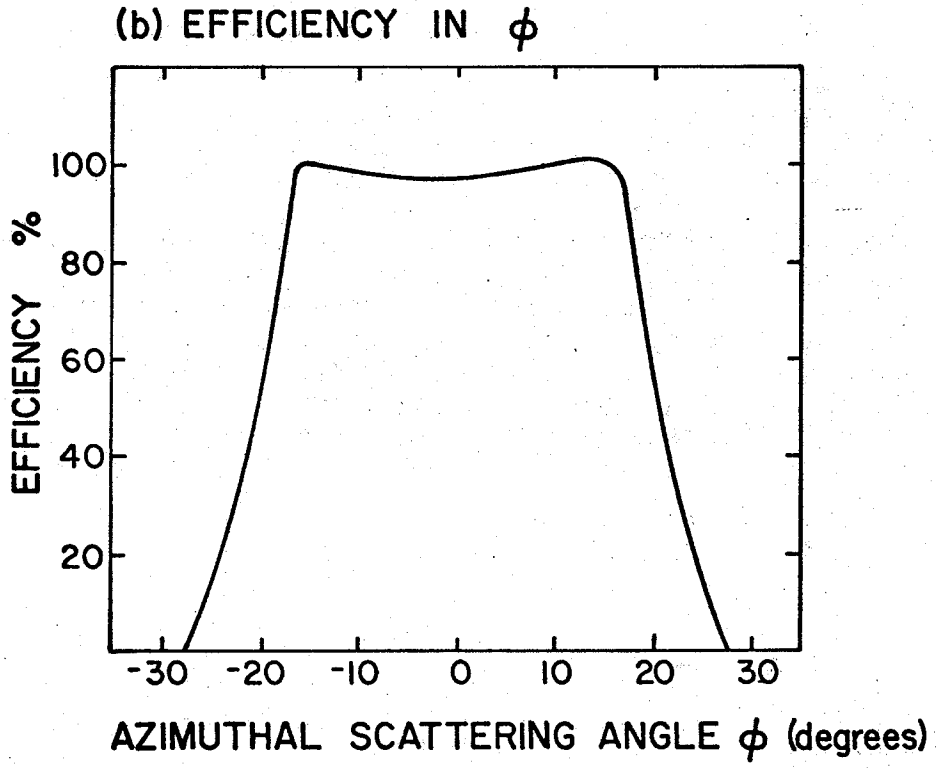
(b) EFFICIENCY IN φ
EFFICIENCY %
100
80
60
40
20
-30
-20
-10
0
10
20
30
AZIMUTHAL SCATTERING ANGLE φ (degrees)

Figure II.6.

The smooth curves give the energy lost by protons, deuterons, tritons and α-particles in passing from the reaction volume to the scintillator.

The dashed curves give the root mean square projected angle of multiple scattering for protons as a function of the scattered energy. Curve (a) has been calculated for protons scattered from hydrogen gas at 32.5° and passing through a delta ray filter 2 mils thick. Curve (b) has been calculated for protons scattered at 45° from hydrogen gas but with the delta ray filter removed.

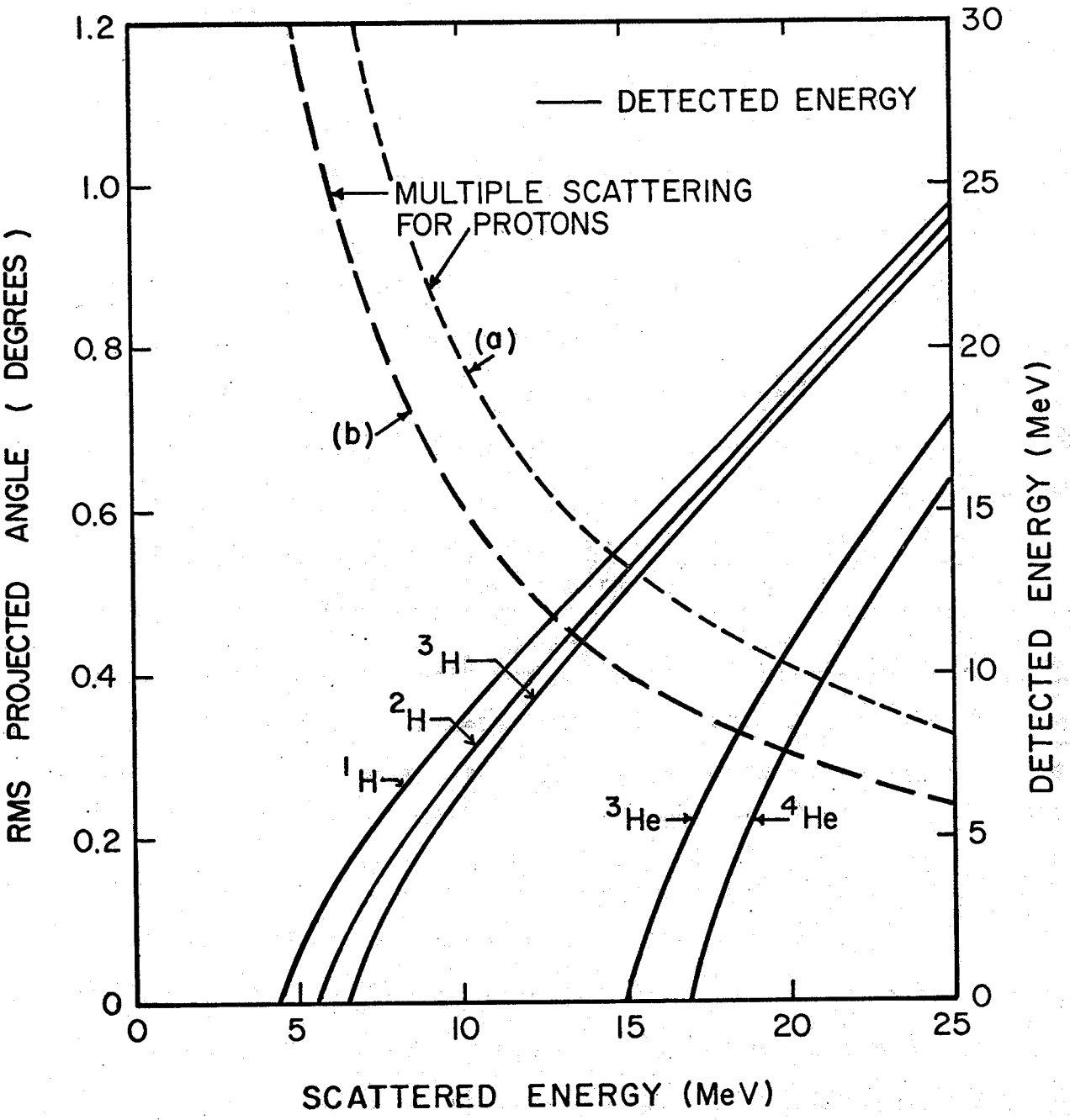
DETECTED ENERGY
MULTIPLE SCATTERING FOR PROTONS
(a)
(b)
^{3}H
^{2}H
^{1}H
^{3}He
^{4}He
RMS PROJECTED ANGLE (DEGREES)
DETECTED ENERGY (MeV)
SCATTERED ENERGY (MeV)
0
0.2
0.4
0.6
0.8
1.0
1.2
5
10
15
20
25
30

of the entrance and exit mylar windows was increased to 0.25 mils and 1.0 mils respectively. The wire chambers are mounted in accurately machined apertures cut in 4 vertical aluminum plates which rest on a 1" thick 4ft square aluminum plate.

The magnetic cores used in the experiment are divided into 108 groups of 18 cores each. The cores are mounted with the 'write', 'read' and 'sense' lines on a 'coreboard' containing the required number of groups for each plane and attached to the vertical aluminum plate adjacent to the plane. Electrical connection is made between each wire in the wire chamber and the appropriate 'write' wire on the coreboard. The electronic circuits used for sending the 'read' current through the ferrite cores are assembled on 'core driver boards' and mounted nearby on the vertical aluminum plate. A photograph of the back right wire chamber and its peripheral equipment is given elsewhere [17].

(b) High Voltage Pulses and Pulse Bias.

The high voltage pulsing system used for the four wire chambers is a somewhat modified version of that described in reference 14. The system at present in use is divided into three quite distinct parts.

(i) Two master pulsers are triggered from two simultaneous 700 mV fast electronic pulses and each delivers

six 800 volt positive pulses 20 nsec wide. These pulses are longer than the chamber charging time but shorter than the spark formation time.

(ii) Twelve high voltage pulsers, which are triggered by the master pulser outputs, deliver current to the wire chamber planes at a sufficient rate to raise their voltage to a few thousand volts before a spark has time to form. In order to provide sufficient current to charge the front chambers to 3,000 volts in 25 nsec three 6DN6 vacuum tubes each providing 25 amps were necessary for each high voltage plane. The higher capacitance inherent in the larger rear chamber was judged to require six 6DN6 vacuum tubes per high voltage plane to provide a similar performance

(iii) The sensitive time of the chamber is controlled by the D.C. clearing field hence ions created by tracks not of particular interest are not allowed to linger within the chamber volume. The field also assists in the 'cleaning up' process after a spark but for operation of the chambers at high repetition rates it is necessary to provide a higher potential in order to decrease the chamber dead time. In our experiment pulsed bias is used following the read-in of the information stored in the magnetic cores. This removes lingering ions even though the sparking rate for the data presented never exceeded 100 pulses per sec.

2.4 Spectrometer Control Logic.

(a) Computer and Control Hardware.

The Manitoba cyclotron computer system as used in the PPB experiment is shown in Fig.II.7 [15, 16]. The trajectories of the two outgoing protons are defined by the information from the wire chambers and the proton energies are defined by the pulse heights from the scintillation counters. The PDP-9 assembly program tries to reconstruct a vertex from the proton trajectories and if successful the relevant coordinates of the proton trajectories and counter pulse heights are sent to the IBM 360/65 computer, otherwise the event is rejected. The latter computer then performs a full kinematic and statistical analysis of the event using Fortran programs and returns some histograms of interest to the PDP-9 for visual on-line display on the oscilloscope, storing on DEC TAPE or for plotting on an x-y plotter (CALCOMP). Data computed from each good event is also stored on a magnetic tape (MAG. TAPE) by the IBM 360/65 for later off-line sorting, selecting and histogramming. A sample of the processed data is recorded on the line printer (PRINTER) which also keeps a comprehensive bookkeeping record of each run.

The logic controlling the operation of the spectrometer is organised through an intimate relationship between software and hardware. The PDP-9 assumes full administrative responsibility through the interfaces to the

wire chambers, fast electronics, pulse height analog to digital converters and the data link to the 360/65. In this way the experiment utilises the economic and reliable characteristics of software whenever possible and it also provides the flexibility necessary during the development stages. There are nevertheless some very important decisions to be made within a few tens of nanoseconds, where fast electronic hardware is vitally necessary, and here the computer controls only the time when these operations may begin. Once the wire chambers have sparked and some preparatory hardware operations completed, control is again invested in the PDP-9 which retains executive responsibility until the next sequence.

The event timing sequence is shown in Fig.II.8. It is represented as a logarithmetic plot and although care has been taken to specify the time accurately, it is mainly intended to show the chronology of the operations. When a random or true coincidence occurs between pulses within the selected energy range, the fast electronic circuits trigger the chambers, stop the data-taking and initiate the ferrite core read-in circuitry. The spark will form within the next hundred nanoseconds causing substantial noise in the experimental area. The analog pulses however, are isolated electronically from this noise and during this time they are being prepared for digital conversion. The exact time taken for conversion

Figure II.7

Manitoba cyclotron computer system as used on-line to the wire chamber spectrometer

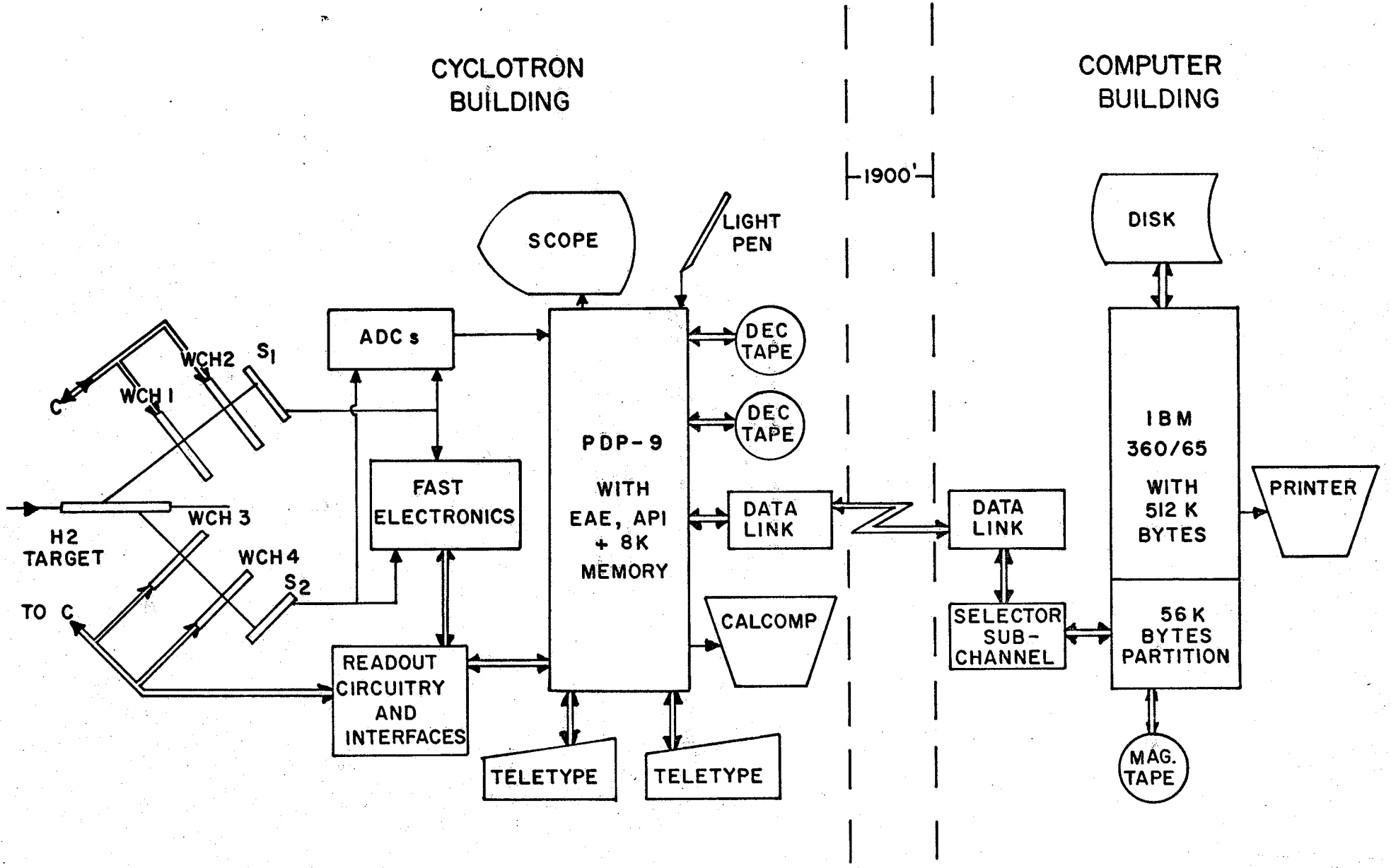
CYCLOTRON BUILDING
COMPUTER BUILDING
1900'
SCOPE
LIGHT PEN
DISK
ADC s
DEC TAPE
DEC TAPE
WCH2
S1
WCH 1
C
PDP-9 WITH EAE, API + 8K MEMORY
IBM 360/65 WITH 512 K BYTES
PRINTER
FAST ELECTRONICS
WCH 3
H2 TARGET
DATA LINK
DATA LINK
WCH 4
S2
TO C
CALCOMP
SELECTOR SUB-CHANNEL
56 K BYTES PARTITION
READOUT CIRCUITRY AND INTERFACES
TELETYPE
TELETYPE
MAG. TAPE

Figure II.8

Event timing sequence.

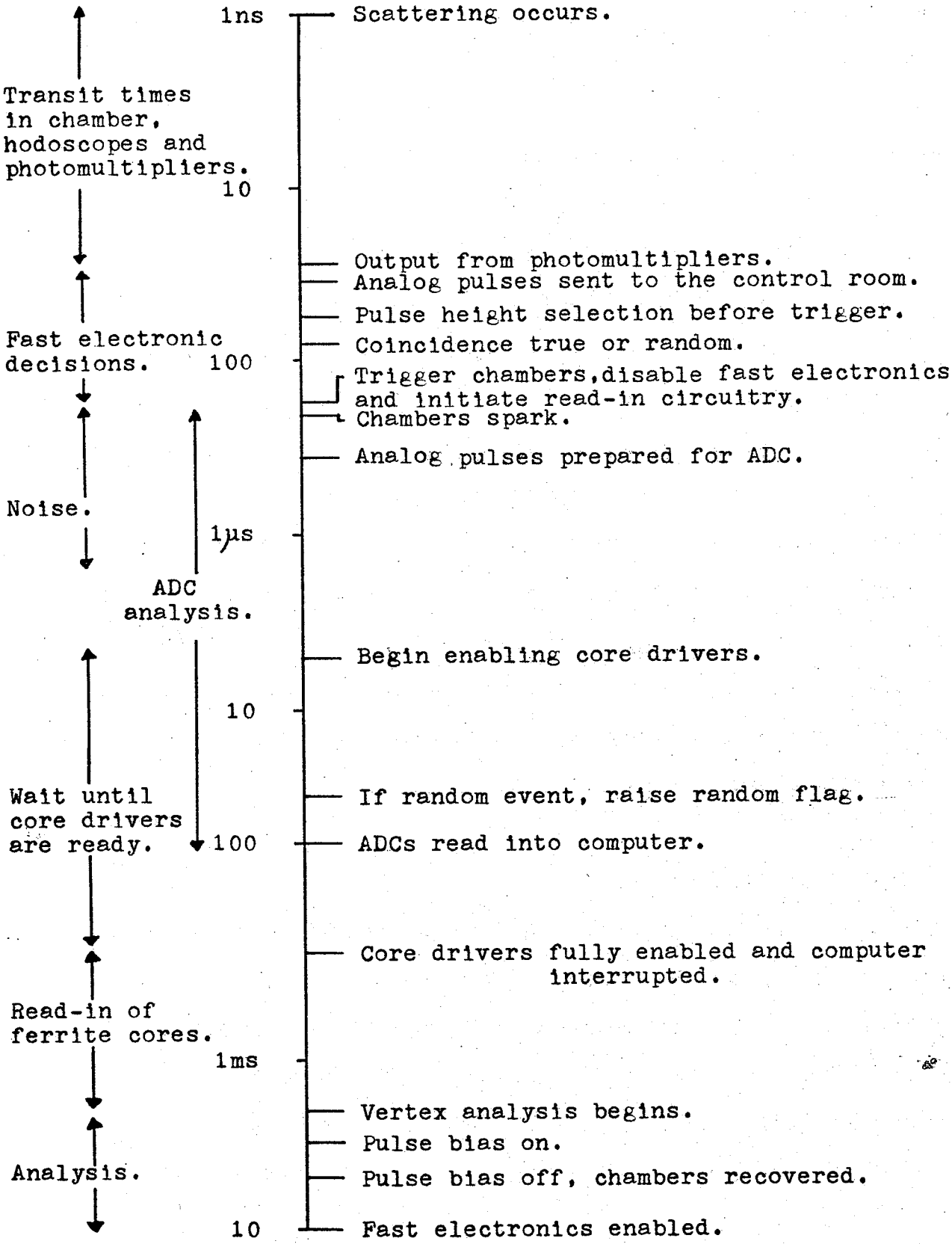
1ns
Scattering occurs.
Transit times in chamber, hodoscopes and photomultipliers.
10
Output from photomultipliers.
Analog pulses sent to the control room.
Pulse height selection before trigger.
Coincidence true or random.
Fast electronic decisions.
100
Trigger chambers, disable fast electronics and initiate read-in circuitry.
Chambers spark.
Analog pulses prepared for ADC.
Noise.
1μs
ADC analysis.
Begin enabling core drivers.
10
Wait until core drivers are ready.
If random event, raise random flag.
100
ADCs read into computer.
Core drivers fully enabled and computer interrupted.
Read-in of ferrite cores.
1ms
Vertex analysis begins.
Pulse bias on.
Analysis.
Pulse bias off, chambers recovered.
10
Fast electronics enabled.

is of course dependent on the pulse height but within the next 100 microseconds they are digitised. At the completion of this operation an Automatic Priority Interrupt is produced in the PDP-9 and the pulse heights are stored into the computer memory.

When the noise has subsided the core driver enabling procedure is begun. This takes 180 μsec and the system must wait for this period. However, if the fast electronics specifies the event to be a random event, the random flag is raised 50 μsec after the chambers were triggered. When the core drivers are fully ready for interrogation, the ferrite cores are read into the computer memory. This takes approximately 2 msec and on completion the computer analysis is begun. During this period pulse bias is switched on for 1 msec to speed the recovery of the chambers. On completion of the analysis the computer enables the fast electronics and the system begins again its wait for a new event.

(b) Fast Electronics.

The practical advantages to be gained by locating all of the fast electronics in the control room is incompatible with the requirement to trigger the chambers as soon as possible after the passage of the particle of interest. This requirement is imposed in order to keep the sensitive time of the chambers to a minimum as this

reduces the probability of multiple tracks. This is particularly inconvenient with low energy accelerators as it is usually not possible to reside in the experimental area when the beam is on.

The schematics for the fast electronics is shown in Fig.II.9. The anode pulses from the XP 1040 phototubes are used for event selection by pulse height as well as for timing purposes. The negative pulse heights from the mixed anode pulses from each tube must lie within the range set by the differential discriminators (DIFF DISC) before passing to the coincidence circuit C1. When the anode pulses from each arm arrive within a resolving time of 28 nsec the decision is made to trigger the wire chambers.

The circuitry required to trigger the chambers with random coincidences only is also available. A delay of 35 nsec (the cyclotron RF cycle time) is imposed on pulses from the right counter to the input of C2, while the left side is prompt. The output pulses from C1 are delayed by 35 nsec and in this way the random events may be slightly overestimated as delay in triggering the wire chambers means operation of the chambers at lower efficiency. This however is expected to be very small in a period of only one RF cycle [9].

The outputs of C1 and C2 are followed by integral discriminators and after passing through a fan-in, they

Figure II.9.

Schematics of fast electronics.

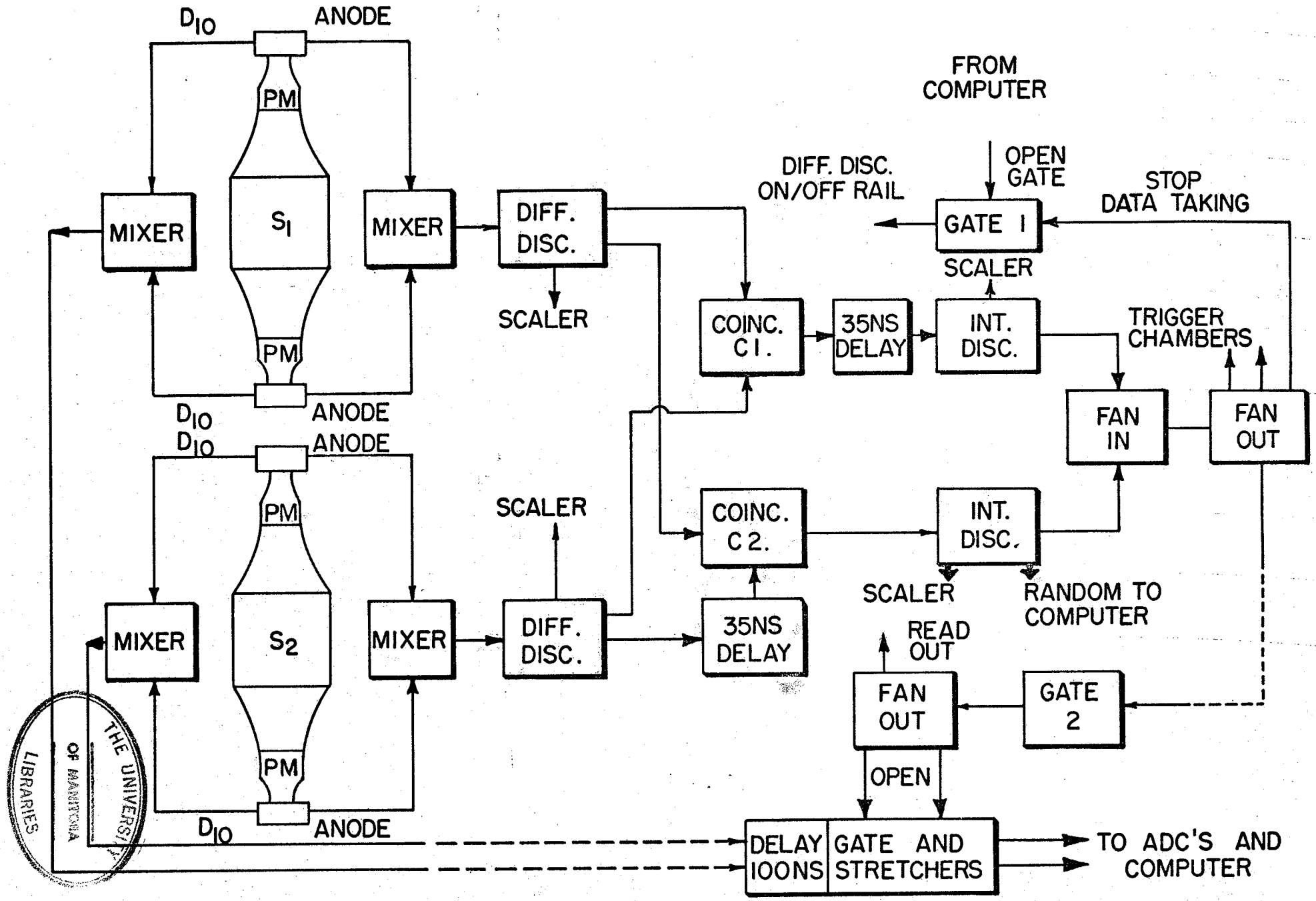

trigger logic fan-outs which send pulses to (1) GATE 1 which closes the fast electronics thereby stopping the data-taking (2) the two high voltage master pulsers (see Fig.II.9) which in turn trigger the wire chambers via the set of high voltage pulsers and (3) GATE 2 whose role is described below.

The dynode pulses from the phototubes are inverted by pulse transformers and sent via 250 feet long double shielded cables to the control room. GATE 2 is opened 20 nsec before the arrival of the analog pulses and after lengthening in a pair of STRETCHERS and digitising in a pair of N.D. ADCs, they pass to the computer memory via the ADC interface. GATE 2 is open for only 150 nsec and the noise from the chamber sparks carried along the cables is thus prevented from reaching the stretchers. The pulse from GATE 2 is also sent to the experimental room to initiate the interface read-out circuitry.

(c) Core Read-out Logic and Interfaces to the PDP-9

After the chambers have been sparked the information required to reconstruct the trajectory of the ionizing particle through the wire chamber hodoscope is contained in the ferrite cores. The problem is to transfer this information from the memory core boards, which are physically attached to the wire chambers, to known locations in the PDP-9 memory.

The sequence of operations, when a particular event is identified by the fast electronics to have the characteristics necessary for a full analysis to be carried out, is implemented by the electronics shown schematically in Fig.II.10. A more detailed description showing the physical lay-out, individual circuitry, operating and programming documentation, together with testing and maintainance instructions is given elsewhere [17].

After the noise from the wire chamber sparks has subsided, the TIMING CIRCUITS send an enabling pulse (A) to the CORE DRIVERS preparing them for interrogation, and approximately 50 μsec later send pulse (B) to clear the UP COUNTER (see below). The TIMING CIRCUITS then interrupt the computer by sending a pulse to the INTERFACES.

The spark information contained in the ferrite cores is read into the computer memory by interrogating the core drivers in a sequential manner. This is accomplished by meeting the demands of a unique combination of inputs controlled by the UP COUNTER and some associated logical gates (DECODERS). The current from the energised core driver passes through a 'read' wire resetting any cores which were 'written' by the chamber spark. The voltage induced by resetting the core from a 'one' to a 'zero' state, called the 'sense' pulse, is amplified (18 SENSE AMP) and sent to the INTERFACE in the control room, where the information is read into the computer memory under program

Figure II.10.

Simplified schematics of the scintillation counters, fast and slow electronics, wire chambers, ferrite core read-out circuits and interfaces to the PDP-9.

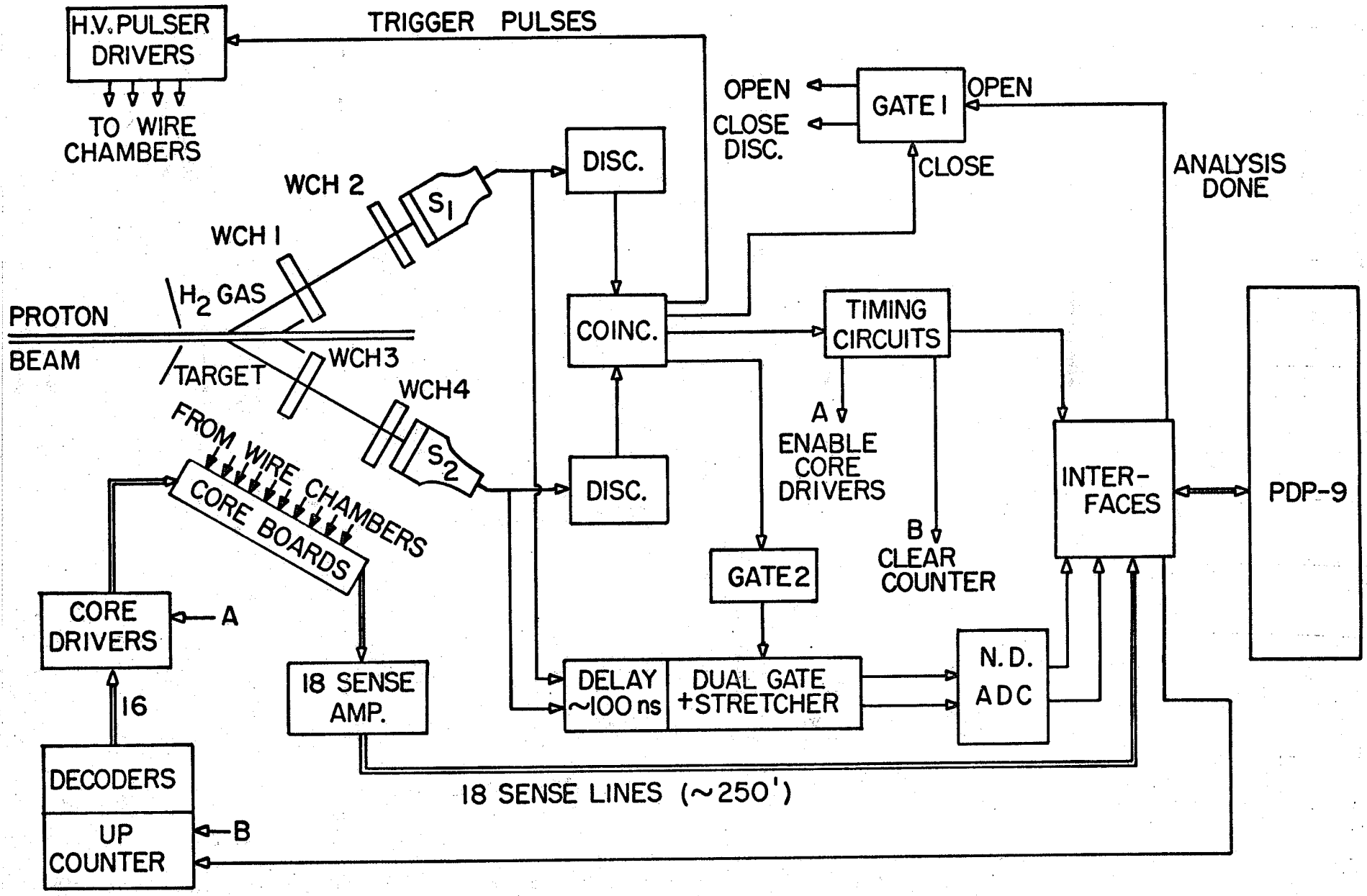
H.V. PULSER DRIVERS
TRIGGER PULSES
TO WIRE CHAMBERS
OPEN
CLOSE DISC.
GATE 1
OPEN
CLOSE
ANALYSIS DONE
DISC.
WCH 2
S1
WCH 1
H2 GAS
PROTON BEAM
TARGET
WCH3
WCH4
S2
COINC.
TIMING CIRCUITS
A
ENABLE CORE DRIVERS
B
CLEAR COUNTER
INTER-FACES
PDP-9
FROM WIRE CHAMBERS
CORE BOARDS
DISC.
GATE2
CORE DRIVERS
A
16
18 SENSE AMP.
DELAY ~100 ns
DUAL GATE +STRETCHER
N.D. ADC
DECODERS
UP COUNTER
B
18 SENSE LINES (~250')

control. The program then causes a signal to be sent from the INTERFACE to increment the UP COUNTER so that the next group is interrogated. This process is repeated and on completion of the interrogation of all the ferrite core groups, the core drivers are automatically disabled and the software analysis begins. At the end of the software analysis a pulse is sent from the INTERFACE to open GATE 1 which enables the fast electronics.

CHAPTER III

Software Identification of Event.

3.1 General Description of Software.

Each time the spectrometer detects an event, 2,016 bits of raw data are obtained. At event rates of 100 per second, a 2,400 ft. magnetic tape would be filled in about 10 minutes if a permanent record of all this information was made. In an experiment lasting for maybe 100 hours, considerations of economy and practicality make a strong argument for some on-line data reduction.

In all nuclear scattering experiments some data is selected by the hardware for further investigation and the rest is discarded. There is nothing unusual about the selection performed at this level in our experiment, but the logical complexity usually inherent in software reductions of data, greatly exceeds that of fast electronics imposing a proportionate increase in risk by using this method. For this reason a primary condition for on-line work is that the data reduction software must be trustworthy and a necessary preliminary is the thorough off-line testing with raw data stored on magnetic tape.

In our experiment the PDP-9 is dedicated to data collection and software data reduction while the 360/65 is used to provide the complete kinematic and statistic-

al processing needed for feedback as well as bulk storage of preprocessed and fully processed data. Although details of the software will be described later in this chapter, it is appropriate here to summarise in Fig.III.1 the general arrangement used for the acquisition and processing of data. Route 1 is used for hardware debugging. Route 3 along with routes A and B were used in the development stages for software debugging and preliminary data-taking. Route 2 is used for normal data-taking.

Software plays such an integral part of the spectrometer's performance that it will be considered in some detail. It is organised within the framework of two specially written monitors, SALMON (Symbolic Assembler Language Monitor) for the PDP-9 and FORMON (FORtran MONitor) for the 360/65. SALMON is present all the time in the PDP-9 memory and handles three basic input-output devices, namely, teletype, DEC tape and data-link. It performs some preliminary bookkeeping and requests and accepts control messages from the experimenter. By typing appropriate mnemonics of two characters, SALMON loads the selected program from DEC tape into a predesignated section of the PDP-9 memory and starts its execution. This feature enables us to "overlay" programs without disturbing areas of memory which might include the collected data or constant parameters. Efficient use is therefore made of the 8K memory words available. FORMON is

a very short program written in Fortran. It is based entirely on a feature of the 360 system of overlaying Fortran subroutines. Therefore, all Fortran programs in use are declared as subroutines and the overlay structure can be arranged to restrict the size of 360 memory required to 60K bytes. FORMON then merely selects the subroutine which was called from the PDP-9 by typing its four character name.

Several programs performing very different functions are in use and their roles are explained briefly.

(a) PDP-9 programs on-line to the wire chambers.

These programs are used mainly for testing of experimental equipment. We have four programs of this kind.

(i) PLNHST checks the program controlled interface, ferrite core read-out logic and circuitry. If requested it stores all raw information from the ferrite cores and ADCs on DEC tape for future use, mainly for debugging purposes. This program also histograms the ADC information and the frequency of firing of each individual wire in all 12 planes. These wire maps provide information on sparking efficiency and are a valuable test for the presence of edge sparks and "dead" wires.

(ii) CHEF provides the experimenter with a more detailed picture of wire chamber characters for given operating parameters. At the level of each individual wire plane, the program lists cluster multiplicities* and

* The term 'cluster' refers to the condition where adjacent cores have been set. 'Multiplicity' is defined as being the number of adjacent cores flipped in one cluster. It is assumed that one spark produces one cluster.

Figure III.1

Flow diagram of basic software used for the on-line and off-line data collection and processing.

Taking route 1 the spectrometer performance can be investigated by processing the data in real time.

Route 2 follows the normal data-taking procedure with vertex and kinematic analysis performed by both computers in real time. Samples of processed and correlated data are returned to the PDP-9 for display and plotting. Processed data can be reprocessed, correlated and returned to the PDP-9 for detailed investigation by the experimenter.

Taking route 3 the raw data, containing all original ferrite core (spark) and pulse height information, may be stored on tape by the IBM 360/65. This raw data is later processed off-line. Taking route B the spectrometer's performance can be investigated and taking route A the raw data can be processed through the VERTEX and KINEMATICS programs.

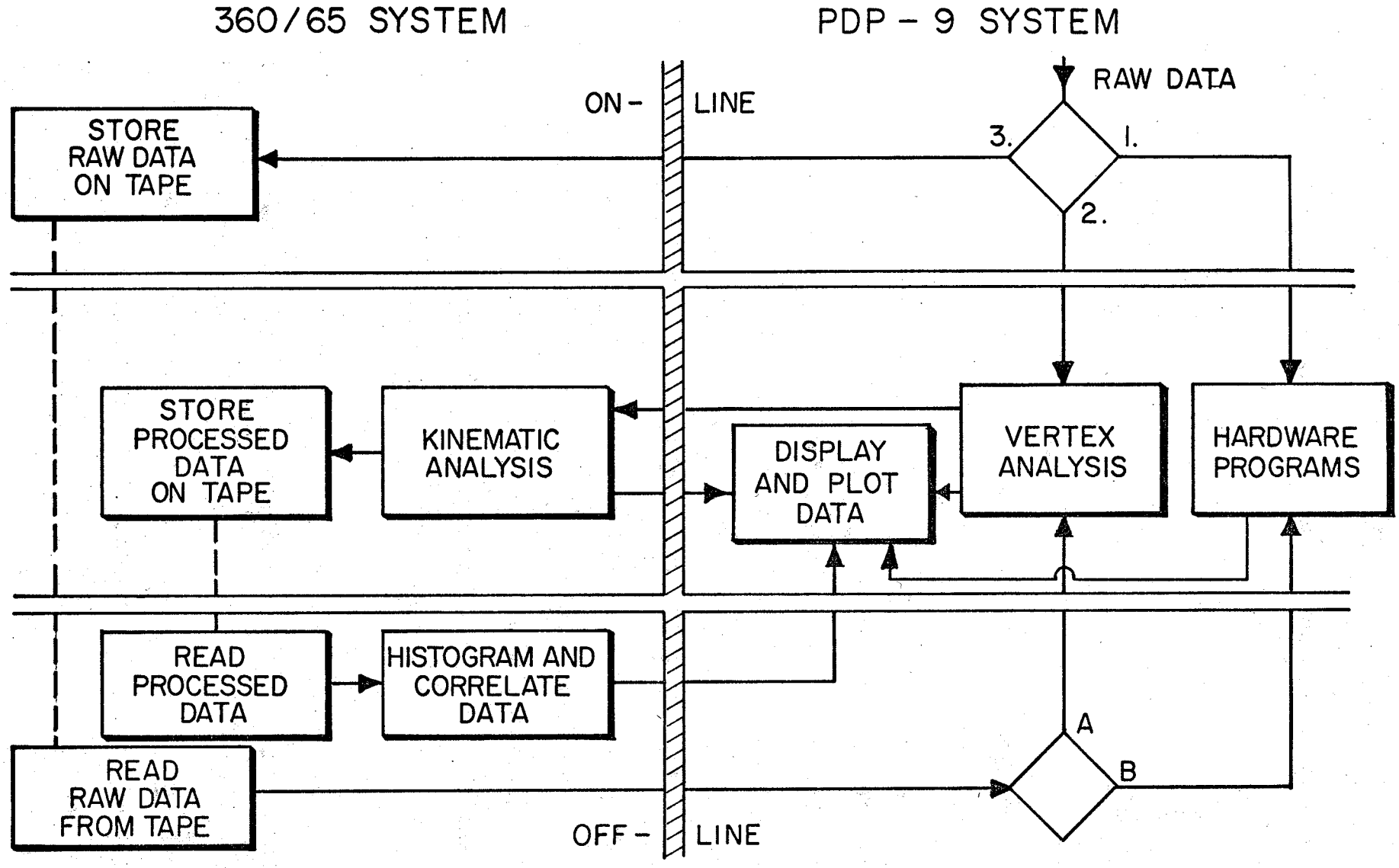
360/65 SYSTEM
PDP - 9 SYSTEM
RAW DATA
ON -
LINE
STORE RAW DATA ON TAPE
3.
1.
2.
STORE PROCESSED DATA ON TAPE
KINEMATIC ANALYSIS
DISPLAY AND PLOT DATA
VERTEX ANALYSIS
HARDWARE PROGRAMS
READ PROCESSED DATA
HISTOGRAM AND CORRELATE DATA
A
B
READ RAW DATA FROM TAPE
OFF -
LINE

tabulates the number of misses, single, double, triple and quadruple clusters found. The program also identifies cluster patterns in each wire chamber and ascertains whether there is just sufficient information to determine the coordinates of as many as two tracks unambiguously. Finally, it histograms the calculated horizontal and vertical spark coordinates from each wire chamber.

(iii) VERTEX reconstructs particle tracks and tests if they make a vertex in the reaction volume. The vertex coordinates can be histogrammed in a variety of ways to suit the experiment. All rejected events are monitored to provide some information of the wire chambers' behaviour during the run (explained in section 3.2(b)).

(iv) NS Program. This is a program which handles only pulse height information from Nuclear Data ADCs. It produces two single pulse height spectra, a two dimensional coincident spectrum with an arbitrary (within memory available) number of channels in each dimension. It also lists coincident information from the ADCs in sequential order in memory.

All four programs mentioned above can display formed histograms on the oscilloscope which can be operated upon with a light pen. Futhermore, single histograms from all programs as well as scatter plots from the ADCs can be plotted on an incremental plotter (CALCOMP).

(b) PDP-9 and 360/65 programs on-line to the wire chambers.

There are two types of programs which serve the following purposes.

(i) STAR which simply controls the transfer of raw data from the ferrite cores and the ADCs to large capacity IBM tape. The large quantities of raw information can be repeatedly analysed later off-line from the wire chambers, which is very convenient for initial testing of software and data analysing procedures.

(ii) The VERTEX-KINEMATICS programs are the most important ones as they are used for on-line real time data-taking and analysis with the two computers. They employ virtually all available processing facilities and they will therefore be described in more detail.

A simplified flow diagram of the Vertex-kinematics program is given in Fig.III.2. The following procedure is used in loading and executing these programs: with SALMON residing in the memory of PDP-9, the experimenter types the mnemonic 'W3' which loads a special initialisation program together with the vertex program. The initialisation program is used first to receive constants from the teletype or paper tape and store them in the memory. These constants are used by the vertex program to specify the geometry (see Appendix B) and to impose the constraints on the acceptance of good events. At the start of execution FORMON requests the 360 operator

Figure III.2.

Simplified flow diagram of the VERTEX-KINEMATICS program combination which uses both computers for on-line data reduction and analysis.

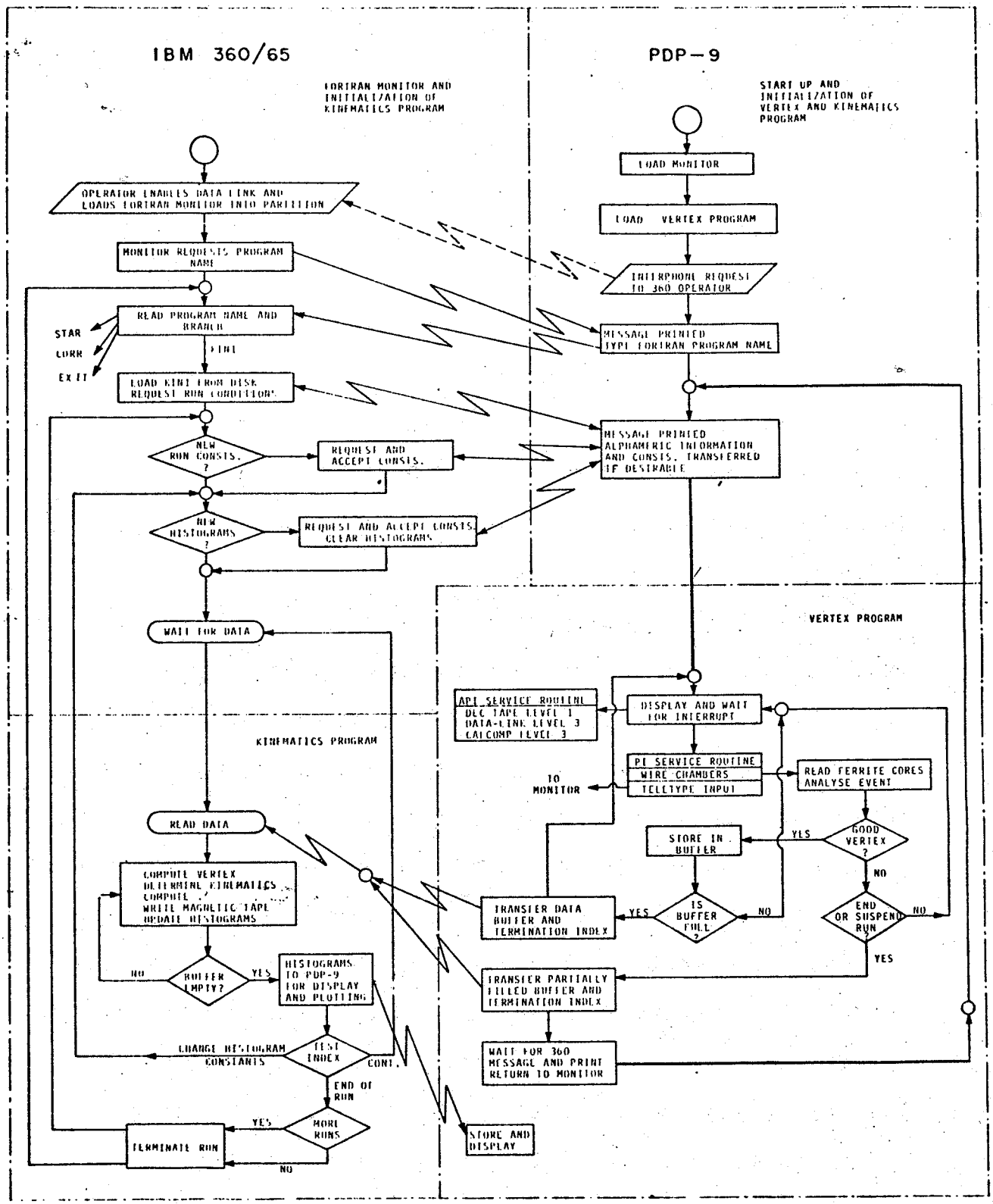
IBM 360/65
FORTRAN MONITOR AND INITIALIZATION OF KINEMATICS PROGRAM
OPERATOR ENABLES DATA LINK AND LOADS FORTRAN MONITOR INTO PARTITION
MONITOR REQUESTS PROGRAM NAME
READ PROGRAM NAME AND BRANCH
STAR
CORR
EXIT
KINI
LOAD KINI FROM DISK REQUEST RUN CONDITIONS
NEW RUN CONSTS. ?
REQUEST AND ACCEPT CONSTS.
NEW HISTOGRAMS ?
REQUEST AND ACCEPT CONSTS. CLEAR HISTOGRAMS
WAIT FOR DATA
KINEMATICS PROGRAM
READ DATA
COMPUTE VERTEX DETERMINE KINEMATICS COMPUTE WRITE MAGNETIC TAPE UPDATE HISTOGRAMS
BUFFER EMPTY?
NO
YES
HISTOGRAMS TO PDP-9 FOR DISPLAY AND PLOTTING
TEST INDEX
CHANGE HISTOGRAM CONSTANTS
CONT.
END OF RUN
MORE RUNS
YES
NO
TERMINATE RUN
STORE AND DISPLAY
PDP-9
START UP AND INITIALIZATION OF VERTEX AND KINEMATICS PROGRAM
LOAD MONITOR
LOAD VERTEX PROGRAM
INTERPHONE REQUEST TO 360 OPERATOR
MESSAGE PRINTED TYPE FORTRAN PROGRAM NAME
MESSAGE PRINTED ALPHAMERIC INFORMATION AND CONSTS. TRANSFERRED IF DESIRABLE
VERTEX PROGRAM
API SERVICE ROUTINE
DEC TAPE LEVEL 1
DATA-LINK LEVEL 3
CALCOMP LEVEL 3
DISPLAY AND WAIT FOR INTERRUPT
PI SERVICE ROUTINE
WIRE CHAMBERS
TELETYPE INPUT
TO MONITOR
READ FERRITE CORES ANALYSE EVENT
GOOD VERTEX ?
YES
NO
STORE IN BUFFER
IS BUFFER FULL ?
YES
NO
END OR SUSPEND RUN
NO
YES
TRANSFER DATA BUFFER AND TERMINATION INDEX
TRANSFER PARTIALLY FILLED BUFFER AND TERMINATION INDEX
WAIT FOR 360 MESSAGE AND PRINT RETURN TO MONITOR

to enable the data link and release the program to engage the PDP-9 program. It then requests from the experimenter the name of the program to be executed by the 360/65. The experimenter responds by typing a four character name of the program (say KIN1) which is loaded from disk into the 360 memory. The execution of KIN1 is begun at this point and the experimenter must type the bookkeeping information essential for a complete record of the run. In addition, miscellaneous constants needed to define the experimental conditions are sent to KIN1 as well as some constants needed to specify the histograms to be formed and returned to the PDP-9 for display on the oscilloscope.

When KIN1 is ready to accept data the vertex program performs the following functions. It turns on the fast electronic gates, jumps into an oscilloscope display routine and waits for an interrupt. When a wire chamber interrupt comes, the ferrite cores are read into the computer, decoded, track coordinates computed, double track ambiguities resolved and an attempt is made to reconstruct a vertex. If successful the track coordinates, scintillation counter pulse heights and event number are stored in a buffer whereupon the PDP-9 returns to the display routine. When this buffer is full its contents are transferred to the 360/65. After the data is received from the PDP-9 KIN1 computes, in both the laboratory and

centre of mass system, the angles and energies of the outgoing protons (corrected for energy lost before reaching the scintillators) and the third particle in the final state. In addition from the errors of these quantities a χ^2 value is computed. At this point all of the information received from the PDP-9 and that computed by KIN1 is stored on magnetic tape. Finally, some histograms are updated and after all the data from a given transfer have been processed the histograms are sent back to the PDP-9 which displays them on the oscilloscope. If the termination index, as set by the experimenter, is recognised, some bookkeeping information and the histograms are returned to the PDP-9, whereupon the run is terminated.

(c) Off-line programs.

Among the off-line programs CORRELATE (CORR) is the most important. CORR reads from magnetic tape data taken in past runs, stores it temporarily on disk, combines it as requested and produces histograms in a manner very similar to that of KIN1. The histogram constants are read in from the PDP-9. The formed histograms are returned to the PDP-9 for display on the oscilloscope or plotting on the CALCOMP plotter. For practical reasons it is very important to be able to call and run CORR from the PDP-9 console as it provides a facility for "quasi-on-line" data processing.

During the initial stages of the spectrometer development, CHEF and the VERTEX-KIN1 programs were adapted

for off-line processing (called AKIN) of raw wire chamber and ADC data stored on IBM tape. This was vitally necessary in order to satisfy the condition of trust in the software and hardware performance discussed at the beginning of this chapter.

In a different category, many programs exist which run in batch processing on the 360/65 quite independently from the PDP-9. The most important of these is OKIN where the preprocessed data can be reprocessed with slightly modified geometric,energy and statistical constants or modified output parameters. The existence of this program is desirable for more refined processing following a searching off-line investigation of the data by CORR. Many other off-line programs have been used during the development stages and all have either been incorporated into the on-line programs or have played their part in the spectrometer design and are no longer active.

3.2 Vertex Analysis by the PDP-9.

(a) Event acceptance criteria.

After the decision has been made by the fast electronics that an event of interest has occurred the four wire chambers are triggered. The VERTEX program is designed to read the ferrite cores into the computer memory, decode the raw data, compute track coordinates, resolve double track ambiguities and attempt to construct

a vertex. An event must obey a set of clearly defined criteria if it is to be accepted for further processing. Some of these criteria are demanded by the nature of the event to be investigated (eg. in the PPB case we require to know the trajectories of the two outgoing protons) but in addition some acceptance criteria are imposed by computational complexity. To pass the demands of the vertex program all of the following properties must be met:-

1. Not more than two non-empty groups per plane.
2. Not more than one empty plane per wire chamber.
3. In the case of a wire chamber with one empty plane only one coordinate can exist in the other two planes.
4. Not more than two coordinate points per plane.
5. Where all three planes in a wire chamber are non-empty only those coordinate points which satisfy $H + V - \sqrt{2}D \leq \varepsilon'$ where H,V and D are the horizontal vertical and diagonal coordinates respectively and ε' is a predetermined constant.
6. Not more than two coordinate points per wire chamber.
7. Not more than a total of six coordinate points in all four wire chambers in any combination.
8. Each track must intersect the beam / vertical plane within a clearly defined area (target volume).
9. For any two tracks being compared it is required that each track must intersect the beam / vertical plane within a small error of one another.

The vertex program is organised to investigate the properties of each wire chamber in turn rather than the event as a whole. Acceptance criteria 1,2,3,4 and 5 are applied to the Front Left (FL), Front Right (FR), Back Left (BL) and Back Right (BR) wire chambers in turn and events are discarded when any violation occurs.

If an event is rejected by the VERTEX program the event characteristics up to the point of rejection are recorded in a set of quality counters. These counters are useful for monitoring drifts and changes in the instrumental properties of the spectrometer during a run, besides providing a convenient means of testing the logic of the program itself.

(b) Testing of VERTEX program.

In the PPB experiment most of the raw data from the wire chambers will be discarded on-line by the VERTEX program. This program consists of approximately 2,000 instructions and during operation a very large number of logical decisions are made before an event is classified and accepted. It is most important that the program is free from errors which might bias the data and considerable attention has therefore been paid to testing this program.

(i) Experimental conditions.

During testing and preliminary calibration the wire chambers were placed in a position where true elastic

coincidences from a solid CH_2 target could be recorded. A collimator with an 1/8" diameter circular hole was placed between the rear chamber and the scintillation counter consequently the proton trajectories triggering the wire chambers were accurately defined. A detailed investigation was made of a small sample of 99 events which formed part of a set of data recorded on magnetic tape using the STAR program. A larger sample was also investigated in less detail in order to find events with special characteristics. The raw data was subsequently read out onto the line printer on the 360/65 for detailed investigation by hand and in addition was transferred to DEC tape for off-line investigation by the VERTEX program. The program was modified to output on the teletype the quality counters after processing each event hence the status awarded to each event could be easily identified.

The data chosen for these tests were taken under very different flux conditions. They were selected from three files recorded when beam currents of 0.05 nA, 0.2 nA and 1.5 nA were incident on the solid target. The delta ray absorber was not in place during these runs. This provided a range of plane cluster frequency from which the program was expected to identify the vertex elastic event known to be present. Detailed analysis by hand was performed on the 99 events from the 1.5 nA file as it was expected that this would provide events of greater

complexity. The data sample was found to encompass all of the possibilities to which the vertex program could be exposed.

(ii) Cluster combinations.

The VERTEX program begins by searching for non-empty groups in the three planes of the front left chamber. The results of the investigations are given in Table 1 and reference will be made to this table as the appropriate sections are discussed. The table 1(a) applies to this section and here the results for the FL, FR, BL and BR are tabulated by dividing the events into the following 4 categories:- (starting from the left) events with a cluster combination which satisfy all criteria at this level, violations of criteria 2 and 3, complete misses in all 3 planes (violation of criterion 2) and greater than two clusters per plane (violation of criterion 1). The top line of table 1(a) shows that 13 events were rejected by criterion 1, 2 events were rejected by criteria 1 and 3 and 84 had good combinations. A careful check by hand of the raw sparks agreed with these numbers, although during the initial tests it was discovered that the program yielded a total which was in excess of the hand processed data by one event. An error in software logic was discovered so that the particular configuration of event No. 85 could increment two quality counters.

The programs then compute the coordinates of accepted

events by studying the non-empty groups. The coordinate u_1 is given by:-

$$u_1 = (n_g - 1)\ 18 + n_o + \frac{n_1 + 1}{2}$$

where n_g = number of the group in the plane

n_o = number of wires in the group to the left of the first fired wire.

n_1 = multiplicity i.e. the number of adjacent wires fired for a single coordinate point.

The smallest coordinate count of the wire chamber is assumed to be half a wire spacing.

(iii) Coordinate consistency.

Two crossed planes are required to determine a point in space and a third plane placed at an angle to these two planes will overdetermine it. For example, with the horizontal and vertical planes giving x and y coordinates, the diagonal coordinate must agree and if the accuracy is high it is possible to identify as many sparks as one wishes. The section of the program which tests the coordinates for consistency is divided into two parts. The first part treats the special case when only two planes were found to be non-empty and each contains one coordinate only. The H and V coordinates are determined from the equation $H + V = \sqrt{2}D$.

The second part is used when all three planes have been found to be non-empty and therefore contain one or

Table 1.

Quality counters accumulated by the vertex program for a test sample of 99 events. There are 3 main divisions:-

(a) Cluster Combinations. Events are rejected for violation of the plane cluster combinations shown. Good events pass to the next wire chamber for further analysis.

(b) Coordinate consistency check by the demand that $H + V - \sqrt{2}D < \varepsilon'$. The categories of acceptance or rejection are explained in the text in subsection (b)(iii).

(c) Track projection and tests for vertex.

two coordinates. A table is set up in the program to accomodate the eight possible combinations of the horizontal, vertical and diagonal coordinates (H,V,D) and a test of consistency is made by demanding that $H + V - \sqrt{2}D \leq \varepsilon'$ where ε' is a small error.

In addition to providing a check on the accuracy of the wire positions within the chamber, the ε' distribution is a measure of how faithfully the spark propagates along the proton trajectory. Fig.III.3 shows the bias which results when protons from elastic scattering pass at an angle of 12^{o} to the plane of the chamber. The bias of 1.5mm is close enough to $d\tan 12^{o}$ where d is the interplane gap (1/4") to conclude that the spark follows the proton track within the resolution provided by the wire spacing. The distribution for protons from the D(p,2p)N reaction which illuminate all of the chamber at incident angles from -12^{o} to 12^{o} (although not uniformly) is seen to be centered at zero. Any inaccuracy in the relative location of the wire chamber frames could of course be corrected by software.

The success or failure at these consistency checks is monitored by a set of quality counters covering this part of the program. Each event will fall into one of the following categories:-

(a) one track zero coordinates (1T0C)

(b) one track one coordinate (1T1C)

(c) two tracks zero coordinates (2T0C)

(a) Cluster Combinations

	Good	Reject		
		Insufficient information	Complete miss	2 clusters
FL	84	1	1	13
FR	54	8	0	7
BL	37	0	0	0
BR	37	0	0	0

(b) Coordinate Consistency

	Good			Reject	
	1T1C	2T1C	2T2C	1T0C	2T0C, $2T_{,} > 2C$
FL	42	22	5	1	14
FR	19	13	5	6	11
BL	30	3	4	0	0
BR	31	1	1	0	4

(c) Track Projections

Too complex	No vertex	Outside reaction volume	Good vertex	Event number	No. of events analysed
0	8	2	23	99	99

Figure III.3

Coordinate consistency distributions for (p,p) elastic and (p,2p)reactions. The (p,p) elastic protons were collimated so that they passed through the chambers at an angle of 12° to the chamber normal. The bias amounts to 1 wire spacing. The D(p,2p)N events are distributed within a range of 12° on both sides of the chamber normal.

(d) two tracks one coordinate (2T1C)

(e) two tracks two coordinates (2T2C)

(f) two tracks greater than two coordinates (2T, >2C)

(a), (c) and (f) are rejected. Table 1(b) gives the results of these investigations by the VERTEX program on the test data. They are tabulated according to the definitions given above.

Comparison with the raw data is not quite so easy at this level. The data must be processed either by hand calculation or the events may be reconstructed graphically. The latter method was chosen as it yields a more readily interpretable picture of the wire chamber sparks. The spark patterns from 30 wire chamber triggers were accurately reconstructed not only to test the program but also to investigate the wire chamber properties. There were some events taken with high flux intensity where the 'pile-up tracks' (i.e. the track of a charged particle which passes through the chamber during its sensitive time) rob the 'firing' track (i.e. the track of the proton which gave a coincidence and caused the chambers to be triggered), giving a coordinate point displaced from the expected region. This is a property of the environment and in all cases investigated the program interpreted the pattern correctly. A typical example of coordinate reconstruction is given in Fig.III.4 and the detailed analysis of this event will be discussed in detail in subsection (v).

FRONT CHAMBERS

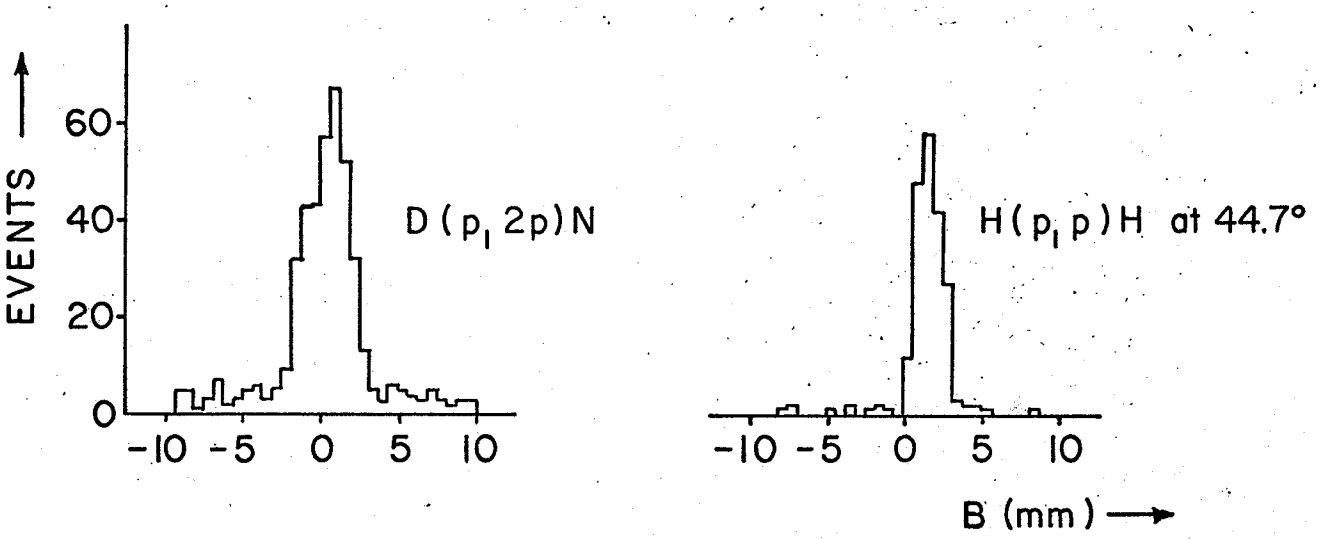

REAR CHAMBERS

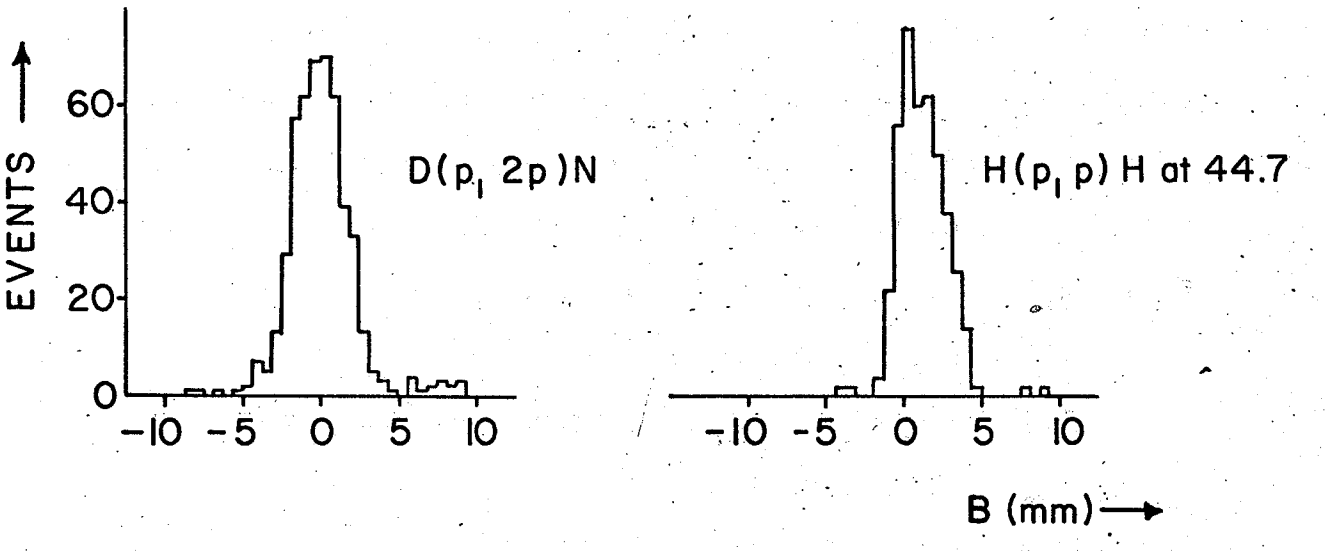

(iv) Track reconstruction.

After finding coordinate points in space the VERTEX program computes and compares all pairs of possible tracks until a pair is found to have a vertex within a certain error. With a maximum of 6 coordinate points there are 11 different configurations possible, from the simple case of a single pair of tracks, to the case where the track on one arm must be compared with 4 possible tracks on the other arm. Unlikely, but, logical construction is greatly reduced by demanding that all constructed tracks must originate within a clearly defined target region. The equations used in the calculations performed by the PDP-9 are given in Appendix B.2.

This part of the program was again tested by graphic reconstruction but it was also found convenient to format the raw data on the line printer in such a way that clusters displaced from the expected position could be easily identified. In this way a much larger volume of data could be analysed. Particular attention was paid to those events in our collimated elastic data which

(a) did not make a vertex

(b) where the projected track lay outside the reaction volume.

From Table 1(c) we see that 33 events were analysed through this part of the program, 8 of which were rejected by the vertex demand and 2 events were rejected because

the computed track did not lie within the reaction volume. These computer decisions were verified by hand calculation where graphical construction did not yield an unambiguous result. In every case it was found that the 'pile-up track' robbed the 'firing track' and the spark occurred at a point well removed from the collimated area. These competing tracks are closely bound up with wire chamber efficiency and will be studied in the next chapter.

During the early stages of this investigation one event in our sample was judged by the program to be a vertex reject yet graphical construction showed that it must make a vertex at the position of the solid target. It was later revealed that with this particluar geometry overflow could occur with a small proportion of events when the 18 bit capacity of the computer was exceeded in the calculation. This problem was subsequently corrected.

The demands imposed upon a program designed to analyse raw data, which can present itself in a large number of quite independent logical configurations, are considerable. The chosen data exposed all of these properties and it can be concluded that the program is free from logical errors that could materially affect the present measurements.

(v) Analysis of a typical event.

Fig.III.4 shows a reconstruction of event number 98, whose character illustrates the pattern recognition

Figure III.4

Spark pattern of a typical event showing the wires which fired when the chambers were triggered by a (p,p) elastic coincidence from a spot beam incident on a CH_2 target. The scattered protons were collimated on the left side by a collimator 1/8" in diameter.

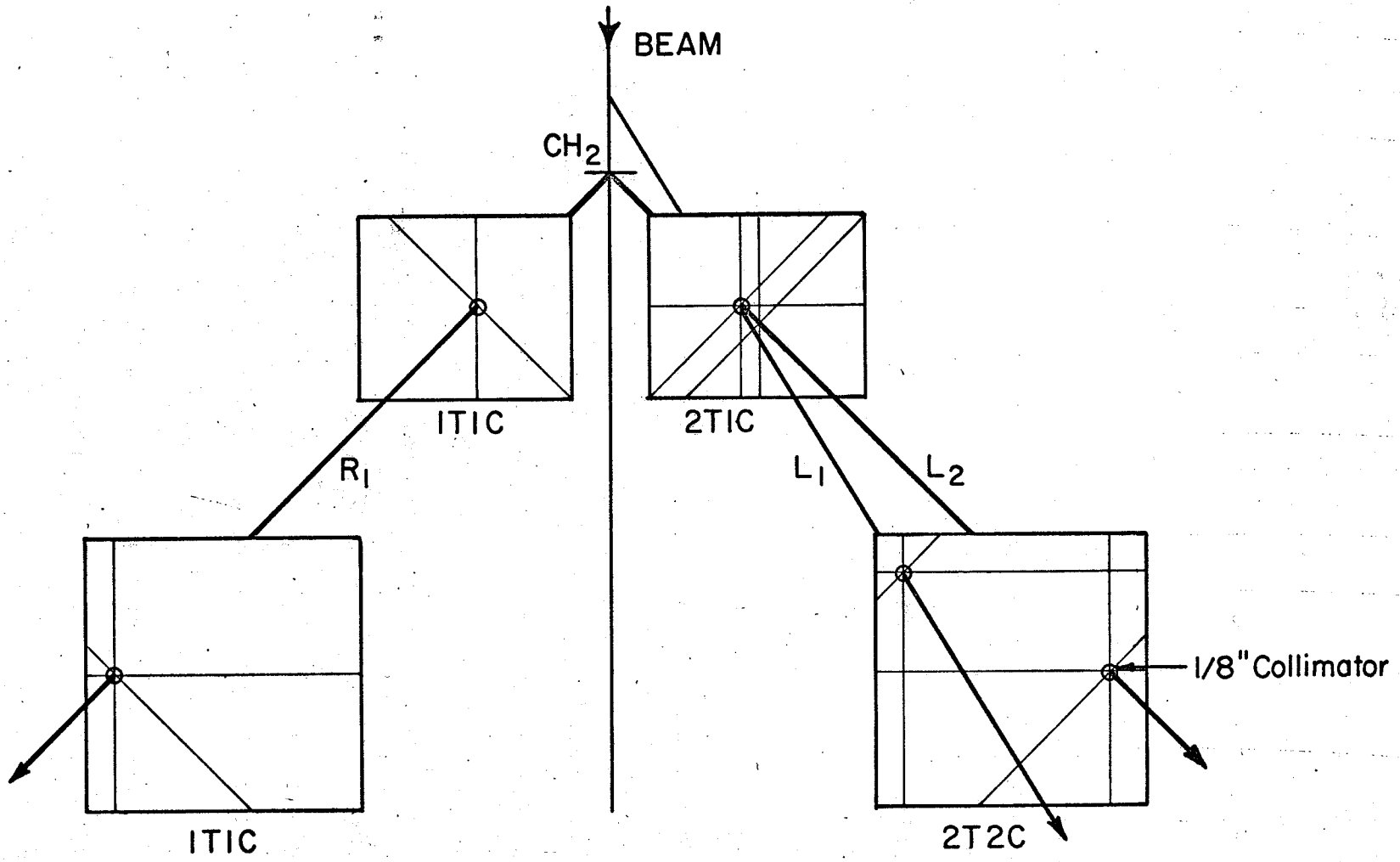
BEAM
CH_2
1TIC
2TIC
R_1
L_1
L_2
1/8" Collimator
1TIC
2T2C

and track reconstruction properties of the program. In the FL chamber 2 clusters are present on the horizontal coordinate plane (vertical wires), 1 cluster on the vertical plane and 2 on the diagonal. Each intersection is tested by the program for consistency and of the 4 possibilities only 1 lies within the required limits. Thus the program concludes that 1 coordinate point is present in this chamber, although two sparks must have occurred. The event is then designated to have a 2T1C configuration for the FL and the horizontal and vertical coordinates are stored for use in the track reconstruction part of the program.

In the BL chamber with two wires firing on each plane, there are 8 possibilities which must be tested for consistency. Fig.III.4 shows that 2 coordinate points are present, one of which is at the point where a proton is known to have passed. The program recognises this pattern to represent a 2T2C configuration in the BL chamber.

The FR chamber is an example of the special case mentioned in subsection (iii) where one wire fires on each of two planes. Here the redundancy invested in the 3 plane design must be exercised, and the assumption is made that the intersection of the vertical wire and diagonal wire defines the point through which a particle has passed. The vertical coordinate is calculated from the equation $V = \sqrt{2}D - H$, stored with the known horizontal

coordinate and the pattern is designated by the program to have a 1T1C configuration in the FR chamber. The pattern found in the BR chamber is quite straight forward and the one possibility is clearly a 1T1C configuration.

There are, therefore, 5 coordinate points from which a pair of tracks (L_1 and L_2) in the left arm of the spectrometer and a single track (R_1) in the right arm can be constructed. The program chooses the simpler side first, which in this case is the right track, and calculates the coordinates Y_R and Z_R of the intersection with the reaction volume. If the values obtained are not within the allowed range the event is discarded. The program tests each left track in turn for intersection with the reaction volume and compares the Y_L and Z_L coordinates of this intersection with Y_R and Z_R. The track L_1 is discarded because $(Y_L - Y_R) > \varepsilon_Y$ where ε_Y is the allowed error in the Y coordinate but the track L_2 is accepted and the 8 coordinates together with the event number and the ADC channel numbers are stored for further processing by the KINEMATICS program.

3.3 Event Analysis by the 360/65.

The computational details on geometry as performed by the KIN1 program are given in Appendix B.3. The proton trajectories are calculated and the intersections with the Y-Z plane are determined. In addition the shortest

distance between the two straight lines in space is also calculated and finally the event is specified in a spherical coordinate system. The energy-momentum conservation relations are used to determine the momentum and the expected error in the momentum of the third particle. Details of these calculations are given in Appendix C.

(a) Calculation of the proton energies.

The energies of the detected protons are determined in three distinct stages:-

(i) The raw pulse heights are corrected for the distribution in pulse height response over the surface of the large scintillation counter using the geometric information supplied by the wire chambers. Details of this procedure are given elsewhere [18].

(ii) The energy deposited by the proton in the scintillator is determined from the assumed straight line dependence between pulse height and energy. This calibration is performed before the run begins and is described elsewhere [18].

(iii) The energy lost by the proton in passing through the hodoscope arm is calculated in order to find the scattered energy. Fig.II.2 shows that from the point where the nuclear interaction occurs the protons must pass through thirteen media consisting of mylar foils, several different gases and aluminum foil before reaching the scin-

tillator. The stopping power, $\frac{dE}{dx}$, is calculated for each medium using the Bethe-Block formula:-

$$-\frac{dE}{dx} = \frac{4\pi z^2 e^4}{m v^2} NZ \left\{ \log \frac{2mv^2}{I} - \log(1-\beta^2) - \beta^2 \right\}$$

where .....(1)

E = energy of the incident particle.

x = thickness of the medium in cm.

m,v,z,e = mass, velocity. atomic no., and charge of the incident particle.

N = number of atoms per cm^3 in the target.

Z = atomic no. of the target.

I = is a parameter related to the mean atomic excitation potential [19].

A small correction can be applied for thick media and the energy loss ΔE_i for the i^{th} medium is then given by the first two terms of the Taylor expansion,

$$\Delta E_i = \frac{dE}{dx} \rho_i x_i \left(1 - 0.5 \frac{d^2E}{d^2x^2} \rho_i x_i\right) \quad ....(2)$$

where the second term is important for media giving large energy losses and ρ_i is the density of the mdeium.

The procedure followed is to find the energy (E) of the proton as it leaves the i^{th} medium and then calculate ΔE_i. Then the energy lost in the $E_{(i-1)}$ medium can be determined using $E + \Delta E_i$ in the calculations. For example the energy determined from the pulse height information makes possible the calculation of $\frac{dE}{dx}$ and $\frac{d^2E}{dx^2}$ for

the aluminum foil. Using equation (2) the energy lost in the aluminum foil can be determined and hence the proton energy leaving the previous medium, in this case air is known. This process is continued for all the media until the scattered energy is found. As $\frac{dE}{dx}$ and $\frac{d^2E}{dx^2}$ are functions of energy, the energy loss must be calculated on an event by event basis.

(b) Goodness of fit.

Six kinematic variables are measured in the final state and using momentum conservation the momentum (and hence the energy E_3) of the third particle can be determined. The total energy, (E_F), including rest masses, in the final state is then given by

$$E_F = E_1 + E_2 + E_3 \qquad \ldots\ldots\ldots(1)$$

where E_1 and E_2 are the total energies of the outgoing protons. As the incident proton energy is known the event is overdetermined. Using energy conservation the deviation from the total energy in the initial state (E_I) must be governed by the kinematic resolution of the spectrometer. We can define a 'goodness of fit' parameter, which we call chi square (χ^2), to relate this deviation to the expected error in the total final state energy, ΔE_F, i.e. we define

$$\chi^2 = \left(\frac{E_I - E_F}{\Delta E_F} \right)^2 \qquad \ldots\ldots\ldots(2)$$

It is not expected that this simple definition will allow

chi square to be governed by well known statistical distributions.

The analysis used in the KIN1 program is a simplified version of the approach used in bubble chamber work [20]. There a program combines the geometrical information about all tracks connected to one point and

(i) makes a hypothesis as to the nature (i.e. mass) of the particles involved.

(ii) introduces the conservation of four-momentum as equations of constraints.

(iii) if the number of constraints is higher than the number of unknowns, the parameters derived from measurements are varied according to the method of least squares and a χ^2 is calculated for the hypothesis in question.

(iv) the whole procedure is repeated for every other possible hypothesis (i.e. set of other particles).

For the present work the assumption is made that each event is either a PPB event or a D(p,2p)N event, as deuterium is the only contaminant known to be always present. A χ^2 value is calculated for each reaction.

The calculations for ΔE_F are carried out in a separate subroutine in the KIN1 program. In the final state

$$E_F = E_1 + E_2 + (P_3^2 + m_3^2)^{\frac{1}{2}} \qquad \ldots\ldots\ldots(3)$$

The error in the azimuthal angle, $\Delta\phi$, is a function

of θ, but as protons are scattered within a restricted angular range we have chosen an average value. The uncertainties in the outgoing proton energies make the most significant contribution to the error ΔE_F. These are certainly independent and if we assume to a first approximation that all errors are independent then

$$\Delta E_F^2 = \left(\frac{\partial E_F}{\partial E_1}\right)^2 \Delta E_1^2 + \left(\frac{\partial E_F}{\partial E_2}\right)^2 \Delta E_2^2 + \left(\frac{\partial E_F}{\partial E_0}\right)^2 \Delta E_0^2 + \left(\frac{\partial E_F}{\partial \theta_1}\right)^2 \Delta \theta_1^2 + \left(\frac{\partial E_F}{\partial \theta_2}\right)^2 \Delta \theta_2^2 + \left(\frac{\partial E_F}{\partial \phi_1}\right)^2 \Delta \phi_1^2 + \left(\frac{\partial E_F}{\partial \phi_2}\right)^2 \Delta \phi_2^2$$

where all the errors are determined experimentally. Performing the above partial differentiation where

$P_3 = f(E_1, E_2)$

$$\Delta E_F^2 = \left(1 + \frac{P_3}{E_3}\frac{\partial P_3}{\partial E_1}\right)^2 \Delta E_1^2 + \left(1 + \frac{P_3}{E_3}\frac{\partial P_3}{\partial E_2}\right)^2 \Delta E_2^2 + \left(\frac{P_3}{E_3}\frac{\partial P_3}{\partial E_0}\Delta E_0\right)^2 + \left(\frac{P_3}{E_3}\frac{\partial P_3}{\partial \theta_1}\Delta \theta_1\right)^2 + \left(\frac{P_3}{E_3}\frac{\partial P_3}{\partial \theta_2}\Delta \theta_2\right)^2 + \left(\frac{P_3}{E_3}\frac{\partial P_3}{\partial \phi_1}\Delta \phi_1\right)^2 + \left(\frac{P_3}{E_3}\frac{\partial P_3}{\partial \phi_2}\Delta \phi_2\right)^2$$

Rearranging

$$\Delta E_F^2 = \Delta E_1^2 + \Delta E_2^2 + \Delta P_3^2 \frac{P_3^2}{E_3} + 2\left(\frac{\partial P_3}{\partial E_1}\Delta E_1^2 + \frac{\partial P_3}{\partial E_2}\Delta E_2^2\right)\frac{P_3}{E_3}$$

where

$$\Delta P_3^2 = \left(\frac{\partial P_3}{\partial E_1}\right)^2 \Delta E_1^2 + \left(\frac{\partial P_3}{\partial E_2}\right)^2 \Delta E_2^2 + \left(\frac{\partial P_3}{\partial \theta_1}\right)^2 \Delta \theta_1^2 + \left(\frac{\partial P_3}{\partial \theta_2}\right)^2 \Delta \theta_2^2 + \left(\frac{\partial P_3}{\partial \phi_1}\right)^2 \Delta \phi_1^2 + \left(\frac{\partial P_3}{\partial \phi_2}\right)^2 \Delta \phi_2^2 + \left(\frac{\partial P_3}{\partial E_0}\right)^2 \Delta E_0^2 \quad \ldots\ldots (4)$$

The details of the calculation to evaluate ΔP_3 are given in Appendix C.

Before using the χ^2 parameter to separate and reject data it is important to test the program and to obtain some measure of its sensitivity to the measured variables of the outgoing protons. The uncertainties in these variables were determined experimentally and are discussed in the next chapter. The results of these tests are shown in Fig.III.5.

In Fig.III.5(a) the two closed curves (henceforth referred to as 'ellipses') are the kinematic loci for PPB for polar scattering angles $\theta_1=20^\circ$ and $\theta_2=30^\circ$. The dashed 'ellipse' is the locus for coplanar events ($\bar{\phi}=0^\circ$) and the smooth 'ellipse' is for events with non-coplanar angle $\bar{\phi}=14^\circ$. The variation of χ^2 as a function of E_1, with E_2 = 10MeV is plotted for $\bar{\phi}=0$ (dashed curve) and $\bar{\phi}=14^\circ$ (smooth curve). It is seen that χ^2 is zero as it intersects the curve and increases rapidly as E_1 moves away from the kinematic locus.

Fig.III.5(b) gives the variation of χ^2 with $\bar{\phi}$ for $\theta_1=20^\circ$ and $\theta_2=30^\circ$ and for two sets of energies as shown in the figure. In neither case does χ^2 exceed the value 2 until the value of $\bar{\phi}$ goes beyond the kinematically allowed range, whereupon it increases very rapidly. Although this suggests that χ^2 is relatively insensitive to $\bar{\phi}$ the curves behave in a way which lends some credibility to the χ^2 calculation.

Fig.III.5(c) shows the sensitivity of χ^2 to changes

Figure III.5

Calculated dependence of χ^2 on kinematic variables for test events from PPB and D(p,2p)N reactions

(a) χ^2 as a function of E_1 for PPB.

(b) χ^2 as a function of $\bar{\phi}$ for PPB.

(c) χ^2 as a function of θ for PPB.

(d) χ^2 as a function of E_1 for D(p,2p)N.

The errors used in the calculations for the incident proton and final state proton are

$$\Delta E_o = 0.3 \text{ MeV}$$

$$\Delta E = 0.3 \ E \text{ MeV}$$

$$\Delta \theta = \Delta \phi = 0.3^\circ$$

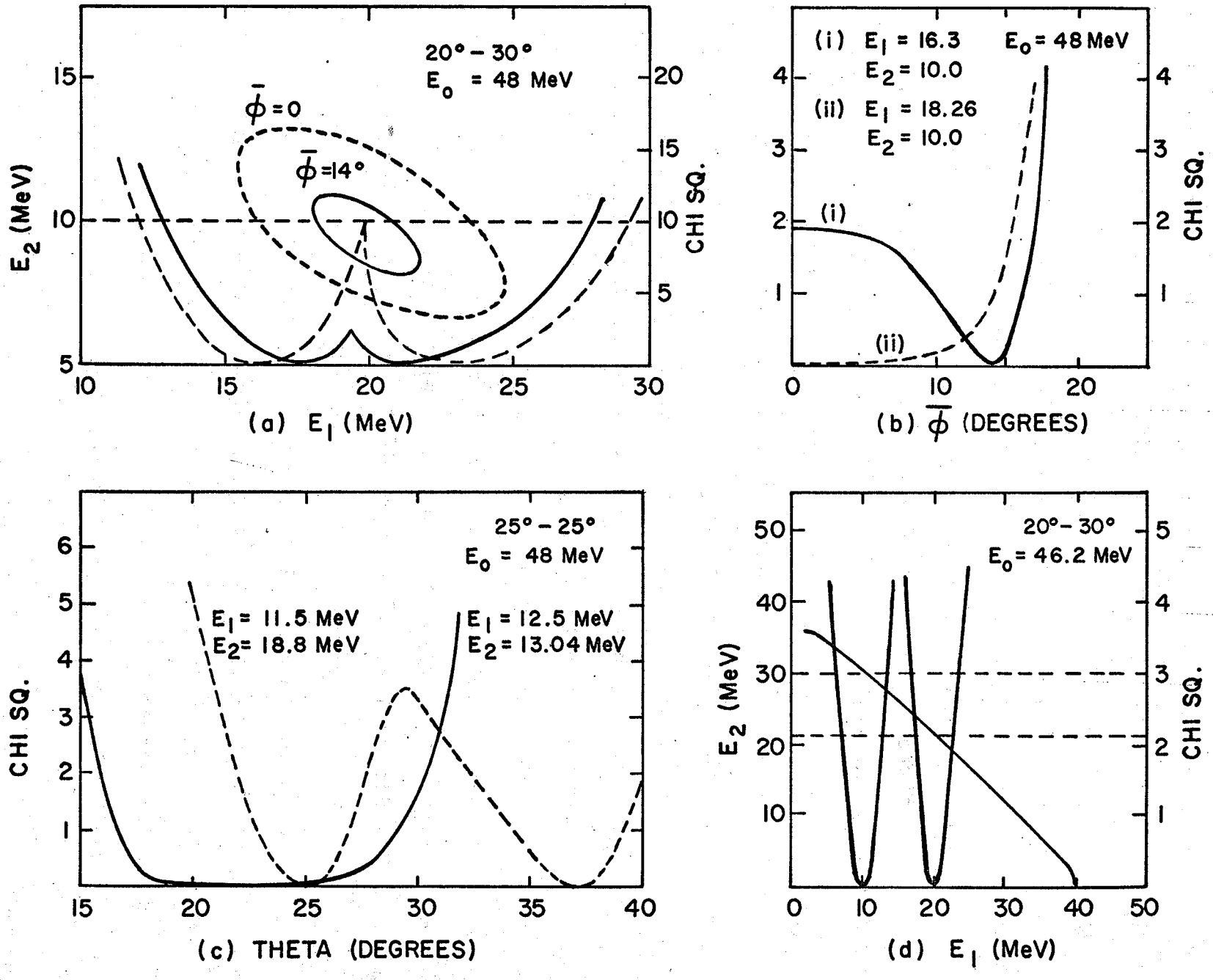
20° – 30°
E0 = 48 MeV
φ̄ = 0
φ̄ = 14°
E2 (MeV)
CHI SQ.
(a) E1 (MeV)
(i) E1 = 16.3 E0 = 48 MeV
E2 = 10.0
(ii) E1 = 18.26
E2 = 10.0
(i)
(ii)
(b) φ̄ (DEGREES)
25° – 25°
E0 = 48 MeV
E1 = 11.5 MeV
E2 = 18.8 MeV
E1 = 12.5 MeV
E2 = 13.04 MeV
CHI SQ.
(c) THETA (DEGREES)
20° – 30°
E0 = 46.2 MeV
E2 (MeV)
CHI SQ.
(d) E1 (MeV)

in θ . Two points have been chosen on the kinematic locus for PPB events with $\theta_1 = \theta_2 = 25^\circ$, $\bar{\phi} = 0$ and with energies as shown in the figure. The kinematic locus tends to move parallel to the major axis of the 'ellipse' when one polar angle is kept constant and the other is varied. The two energy points were chosen to be at the extreme ends of the major and minor axes of the energy locus. The dashed curve gives the variation of χ^2 with θ_1 for $\theta_2 = 25^\circ$ and the energy point on the major axis. The value of χ^2 falls to zero at two points where the kinematic locus, moving parallel to the major axis, passes through the point. The smooth curve shows the variation in χ^2 for the energy point on the minor axis and the single broad minimum indicates that under these conditions χ^2 is relatively insensitive to changes in θ .

The behaviour of χ^2 for coplanar events from deuterium break-up was evaluated for $\theta_1 = 20^\circ$ and $\theta_2 = 30^\circ$ at two different energy points on the D(p,2p)N kinematic locus. The diagonal curve on Fig.III.5(d) is the kinematic locus and the two curves, each with a single minimum, shows the variation of χ^2 with E_1 for $E_2 = 30.1$MeV and $E_2 = 21.2$MeV.

A more sophisticated calculation with a complete kinematic fit for each event may increase the discriminating properties of χ^2. Work on the adjustment of the kinematic variables to minimise χ^2 is in progress but has

not been used in the present calculations. It may be concluded, that although χ^2 as calculated above is not expected to obey exactly the statistical distribution for PPB, it does have the ability to separate events within the PPB region.

CHAPTER IV

Calibration and Measured Properties of the Spectrometer.

4.1 Wire Chamber Properties.

As wire chamber hodoscopes have not previously been used in low energy nuclear physics experiments, their performance under actual operating conditions is of some interest. The ability of the hodoscope to reproduce accurately the trajectory of the scattered particle depends on multiple scattering and spatial resolution of the chamber. The variation of multiplicity with pulse voltage is given in subsection (a), although the low redundancy of our system precludes a measurement of the spatial resolution.

A critical property of the spectrometer, which is directly related to wire chamber performance, is the fraction of events which make a vertex. This problem of spectrometer efficiency is approached in the discussion which follows in three steps. In subsection (b)(i) plane efficiency is discussed. The ability of the chamber to define a consistent set of coordinates is investigated in subsection (b)(ii). Finally, the efficiencies of all four wire chambers are joined in subsection (b)(iii) which deals with vertex efficiency.

Although wire chamber efficiency depends on a large number of parameters, it is not always necessary and

worthwhile to optimize each of them. For example, the quantity of alcohol vapour in the chamber gas is known to be important, but in our case the Ne/He gas mixture was simply bubbled continuously through alcohol at $0^{o}C$. In practice our operating conditions were determined by the three easily variable parameters pulse voltage, operating flux and clearing field. A high clearing field will decrease the sensitive time and hence the probability of multiple tracks but will also tend to decrease single track efficiency. The compromise to be reached is strongly dependent on the beam current which in turn is influenced by considerations other than wire chamber efficiency. At this stage we have not investigated the effect of clearing field in any detail. The variation in spectrometer efficiency with beam current is discussed in subsection (c). The effect of pulse bias on the chambers has not been investigated.

(a) Multiplicity.

As the high voltage increases the average number of cores set per spark increases. Fig.IV.1 shows how multiplicity varies with applied voltage for the horizontal and diagonal planes on the back right chamber. These planes are representative of the pulsed and ground planes for the other chambers. The voltage scale is the D.C. input to the pulser but the voltage level on the plane just

Figure IV.1

The multiplicity of pulsed and ground planes as a function of chamber voltage for the back right chamber.

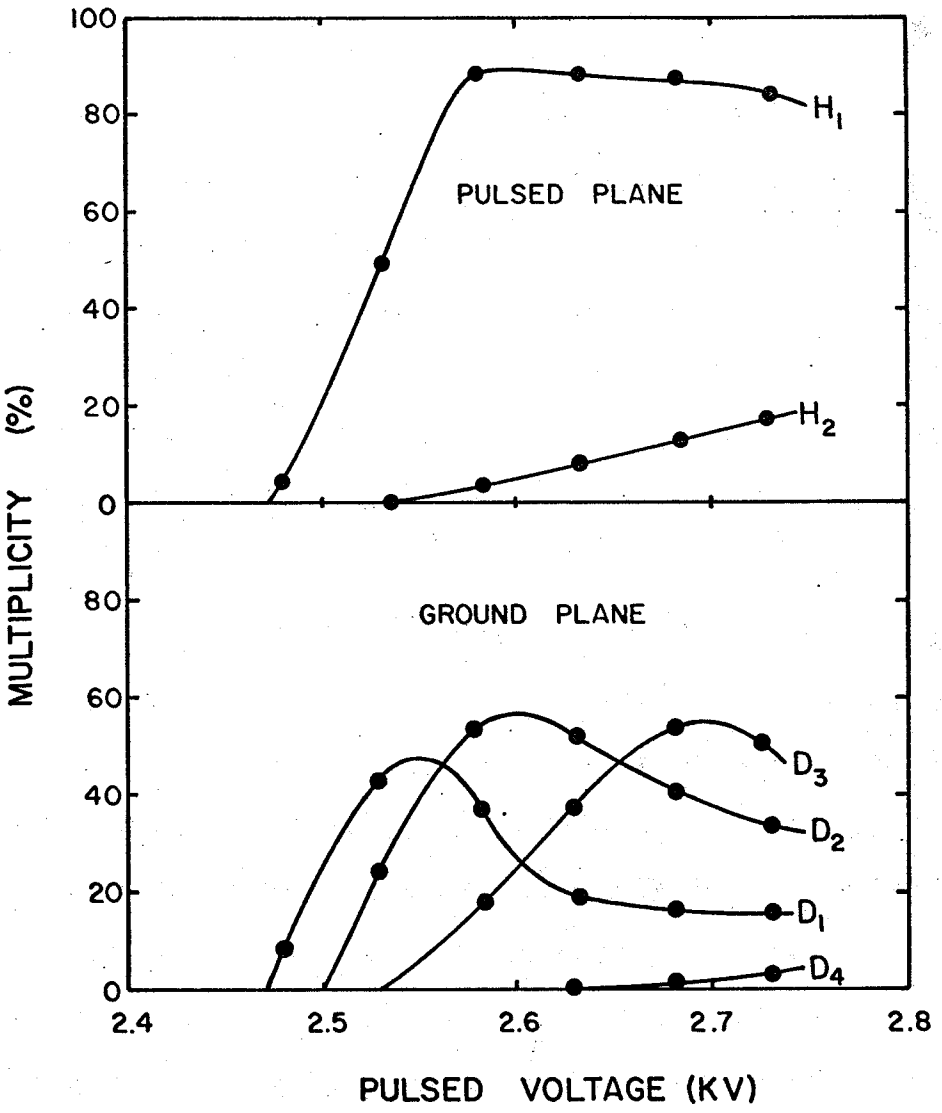
100
80
60
40
20
0
PULSED PLANE
H_1
H_2
GROUND PLANE
D_3
D_2
D_1
D_4
2.4
2.5
2.6
2.7
2.8
MULTIPLICITY (%)
PULSED VOLTAGE (KV)

before the spark develops is not known accurately. The sample of 1,000 triggers includes events with two clusters.

On the plateau the pulsed plane multiplicity is almost independent of applied voltage with 90% singles and 10% doubles at the operating potential of 2,630 volts. The higher multiplicities on the diagonal plane are due to this central ground plane collecting current from both H and V planes simultaneously. As the diagonal plane is used only for the coordinate consistency check, except for the special and infrequent (0,1,1) case, the higher multiplicities on this plane do not affect the spatial resolution. The multiplicity results for pulsed and ground planes are in basic agreement with the results found by Blieden et al.[21].

(b) Wire Chamber Efficiency.

(i) Plane efficiency.

The plane efficiency is influenced by many factors which have been studied in detail by several workers[22,23]. If the experimental conditions are such as to ensure that all chamber triggers are due to genuine proton elastic coincident tracks then we can define the plane efficiency, ε_p, as the fraction of events, not rejected by software, that produce a spark. Hence

$$\varepsilon_p = \frac{N_p}{T - N_s}$$

where

N_p = number of events producing a spark.

T = number of triggers.

N_s = number of events with greater than 2 clusters, i.e. events rejected by software.

N_s represents a software constraint and is not a property of the chamber but of the environment.

Investigations of wire chamber efficiency were made with the rear wire chambers placed in a position so that true elastic coincidences could be observed. A 0.2 nA proton beam incident on a 0.006" CH_2 solid target was used. The flux of scattered protons passing through the front and rear wire chambers under these conditions was measured previously to be 3.4×10^4/sec and 1.1×10^4/sec respectively. The delta ray absorbers were not in place during these runs so the flux of ionizing particles from this source was unknown, but later measurements (see Fig.IV.7) have shown that at this beam intensity it was relatively small. The raw data was stored on magnetic tape using STAR program and later processed off-line with the CHEF and AKIN programs.

The variation of plane efficiency, ε_p, with chamber pulse voltage for a clearing field of 120 volts is shown in Fig.IV.2. At the operating points more than 99% of triggers produced a spark. The larger rear chambers reach

Figure IV.2

Variation of plane efficiency with chamber voltage. The voltage scale is the D.C. voltage input to the H.V. pulser.

PLANE EFFICIENCY ϵ_p

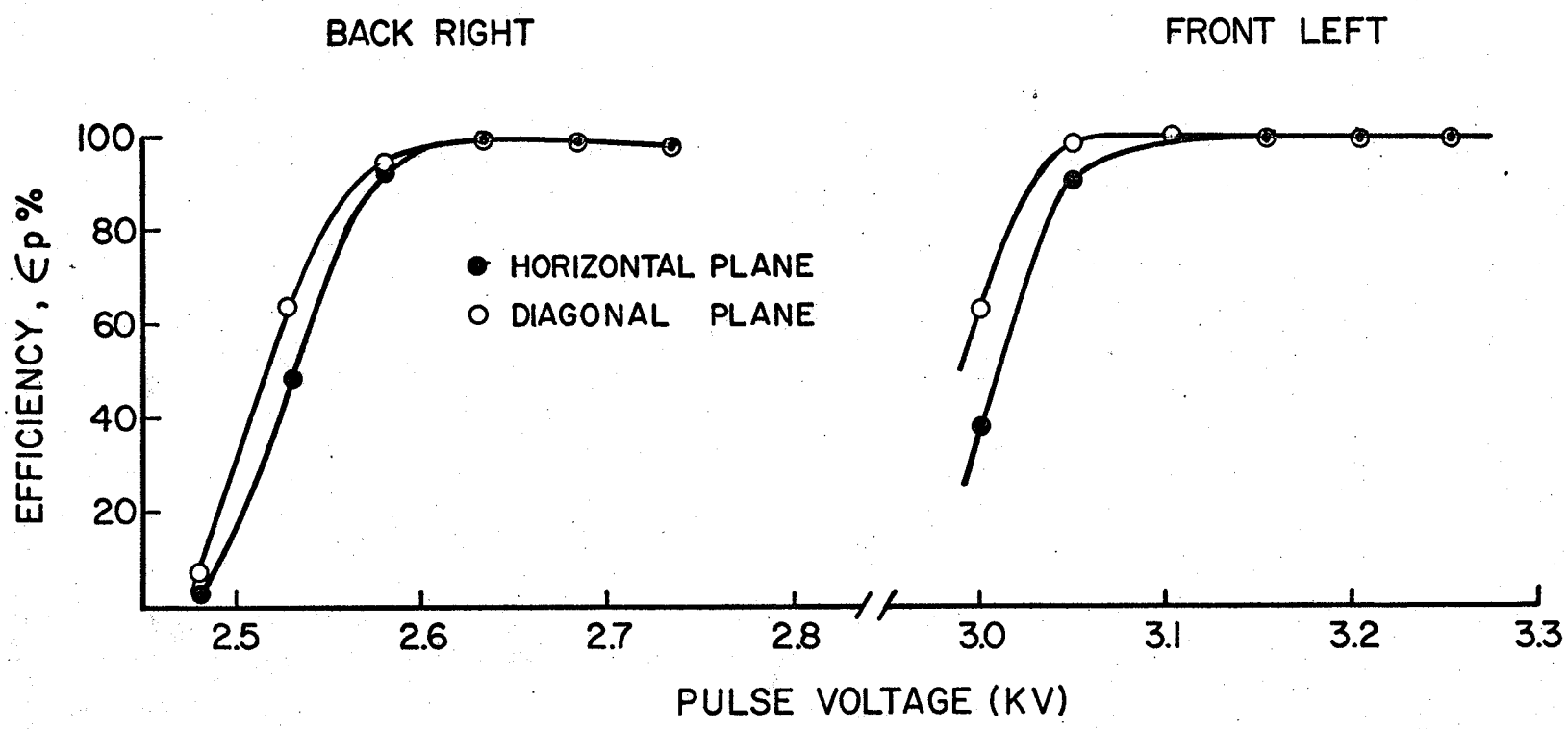

a plateau at 2,650 volts, 450 volts lower than the corresponding point for the front chambers. As the diagonal plane collects charge from both pulsed planes, it is reasonable to expect that these planes will reach a plateau at lower voltages than horizontal and vertical planes.

(ii) Coordinate efficiency.

The test for consistent coordinates to resolve ambiguity from double tracks can lead to rejection, if the coordinates are not consistent within the allowed range, (see subsection 3.2(b)(iii)). Also as this allowed range is $\pm$ 3 wire spacings (see Fig.III.3) there is a finite chance of overlap for simultaneous tracks. Miyamoto[24] has shown that the probability, P, for unresolved multiple tracks is given by

$$P = \frac{n(n-1)^2}{(N_h N_v)/B^2}$$

where n = number of tracks.

N_h = number of wires in the horizontal plane.

N_v = number of wires in the vertical plane.

$B = H + V - \sqrt{2}D$ i.e. the FWHM of the coordinate consistency distribution in wire spacings.

For example, with 2 simultaneous tracks in the front chamber, P = 0.02 and for 3 simultaneous tracks, P = 0.12.

For a particular event which has passed the tests at plane level, the probability of passing through all of the coordinate consistency tests, ε_c, is shown as a function

of applied voltage in Fig.IV.3. At the operating point ε_c, is 94% for both front and rear chambers, with most of the rejections falling into the two track, zero coordinate category. This is probably due to the robbing of one track by another. Fig.IV.3 also gives the wire chamber efficiency, ε_w, as a function of applied voltage. ε_w is the probability of a 'less-than- three-cluster' event giving a consistent set of coordinates , hence,

$$\varepsilon_w = \varepsilon_p \varepsilon_c$$

as $\varepsilon_p = 99\%$ the wire chamber efficiency is controlled by ε_c.

(iii) Vertex efficiency.

The software is organised to investigate all 4 wire chambers in turn and then the probability, ε_T, that a particular event will reach that point in the program where sufficient information allows proton trajectories to be compared is given by

$$\varepsilon_T = \left(\varepsilon_p \varepsilon_c\right)^4$$

The above simple power relationship for ε_T does not take correlations into account. At the operating point in the case discussed above, the FL, FR, BL and BR had values of 93.5%, 94.0%, 93.4%, and 99% for ε_w. Hence 81% of these events could be expected to undergo track analysis. In effect the measurement gave $\varepsilon_T = 0.87$. This could be easily understood if one keeps in mind that some events will violate the acceptance criteria in more than one chamber.

Figure IV.3

For those events which qualify for test at coordinate consistency level the variation of the percentage which survive, ε_c, is plotted as a function of applied chamber voltage for the back right and front left chambers. The product of the plane efficiency ε_p and ε_c gives the probability ε_w that an event with consistent coordinates will be found.

COORDINATE AND CHAMBER EFFICIENCY

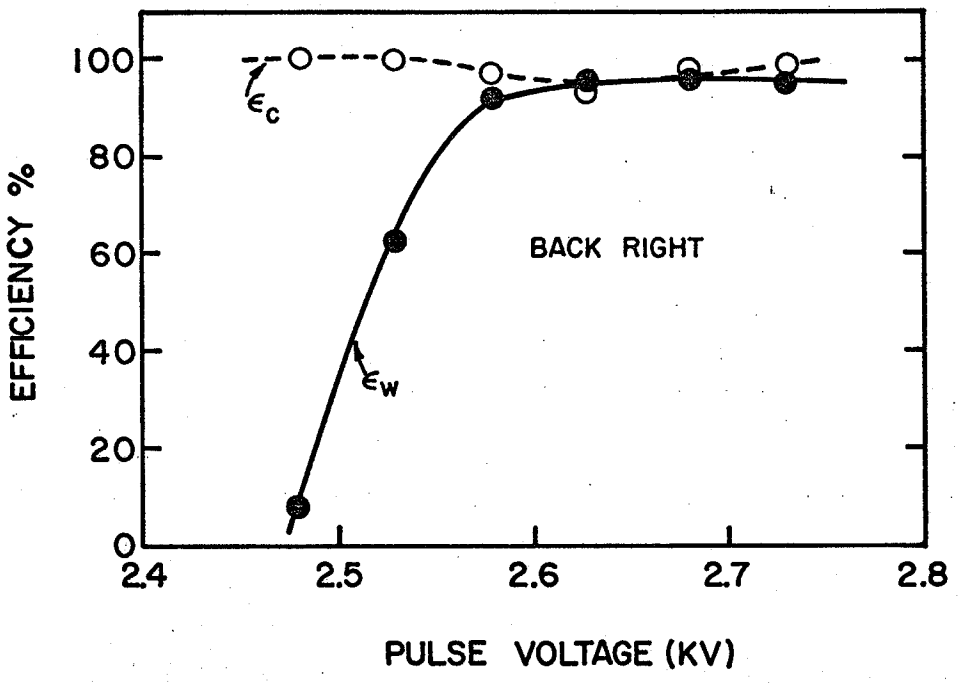

(a)

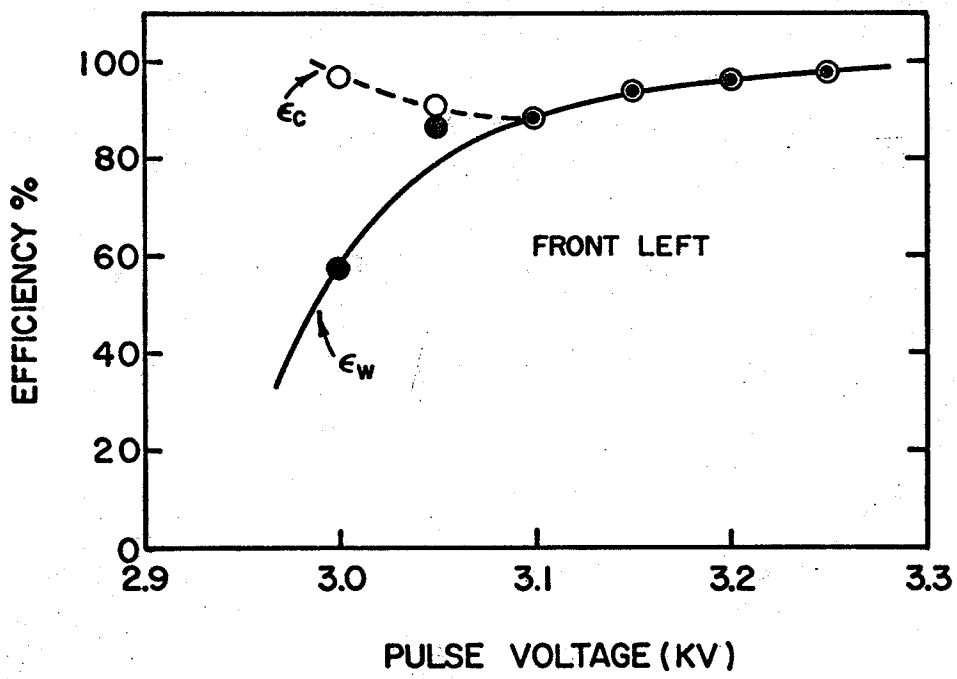

(b)

Figure IV.4

(a) Variation of vertex efficiency with pulse voltage for events with vertical and horizontal vertex errors less than 1" when a 0.2 nA proton beam was incident on a 6 mil thick CH_2 target.

The curve with closed dots is normalised to include only those events with less than 3 clusters in any plane. The curve with open circles is the efficiency of good vertex events for all chamber triggers.

(b) Variation of conditions responsible for rejection with chamber pulse voltage.

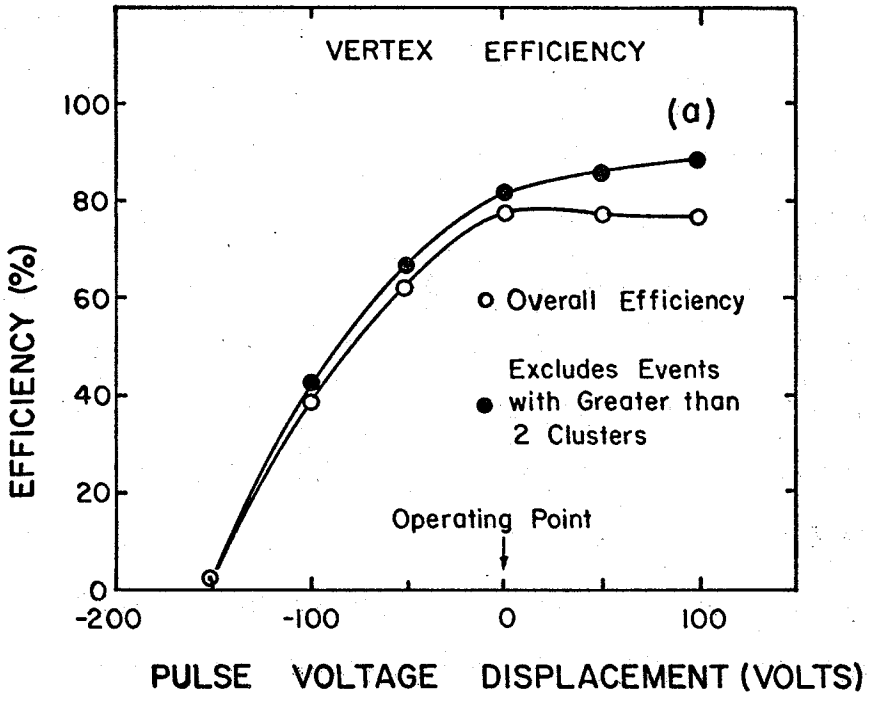
VERTEX EFFICIENCY
(a)
EFFICIENCY (%)
100
80
60
40
20
0
-200
-100
0
100
o Overall Efficiency
Excludes Events
● with Greater than
2 Clusters
Operating Point
PULSE VOLTAGE DISPLACEMENT (VOLTS)

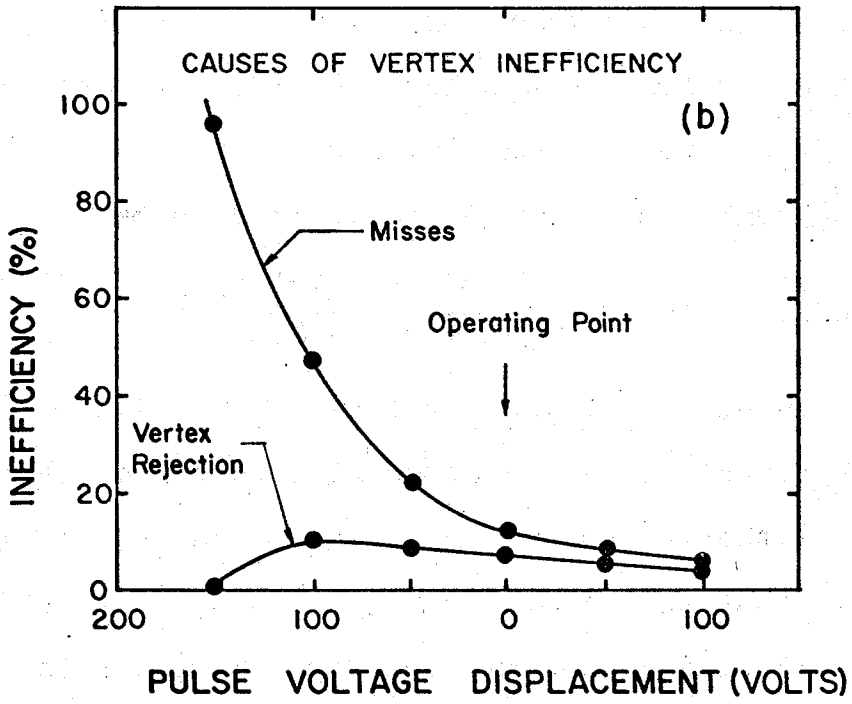
CAUSES OF VERTEX INEFFICIENCY
(b)
INEFFICIENCY (%)
100
80
60
40
20
0
200
100
0
100
Misses
Operating Point
Vertex
Rejection
PULSE VOLTAGE DISPLACEMENT (VOLTS)

Fig.IV.4(a) shows the variation of vertex efficiency with voltage for all events (open circles) and for events which had less-than-three-clusters (full circles) in any wire chamber. It is instructive to note that excluding less-than-three-cluster events a higher voltage above the operating point increased the vertex efficiency to 89%. The overall vertex efficiency remained unaffected when the less-than-three-cluster events were included.

The cause of vertex inefficiency is illustrated in Fig.IV.4(b). The lower curve labelled 'vertex rejection' gives the percentage of the total number of less-than-three-cluster events which are rejected on vertex. This rejection initially rises to 10% and then decreases with an increase in applied voltage. Some events are undoubtedly rejected in the case where the triggering track is robbed by a 'pile-up' track and a larger applied voltage may increase the double track efficiency.

The number of 'MISSES' is defined to be

$$\text{MISSES} = \frac{\text{number of events } \underline{\text{not}} \text{ reaching tracks}}{T - N_S}$$

where T and N_S are defined in subsection (b)(i). Fig.IV.4(b) shows that the greatest contribution to vertex inefficiency comes from the various types of misses which can occur. It is concluded that the maximum overall spectrometer efficiency will be achieved at the higher operating potentials providing the beam intensity is not so high as to produce many more-than-two-cluster events.

(c) Beam Current Dependence.

In experiments with low cross sections the data-taking rate is of considerable importance. In practice this is controlled by the magnitude of the primary beam as the target is usually determined by other considerations. It is important, therefore, to determine how the wire chambers perform over a wide range of beam current.

In the discussion in this subsection, vertex efficiency is defined as the number of events making vertex divided by the number of chamber triggers. Some preliminary results on the variation of vertex efficiency with beam current are shown in Fig.IV.5. The open circles represent vertex efficiencies taken when a 0.2 nA proton beam was incident on a 0.006" thick CH_2 solid target placed 3" downstream from the centre of the scattering chamber. The chambers were triggered on elastic proton-proton coincidences. The delta ray absorbers were not in place during these three runs.

The closed circles represent data points taken under simulated PPB data-taking conditions. With the scattering chamber filled with hydrogen gas, the beam transport was adjusted to provide a beam profile in the chamber identical to the PPB data-taking conditions. The geometry and electronics were arranged to trigger on p-p elastic scattering from the hydrogen gas target. A 0.001" thick delta ray filter was in place for these runs.

Figure IV.5

Vertex efficiency as a function of beam current.

Curve with open circles was taken when a 0.006" CH_2 target was used and the chambers were triggered on hydrogen elastic coincidences with the delta ray filter removed.

Curve with closed circles was taken by triggering on elastic coincidences from a hydrogen gas target but with a 0.001" delta ray filter in position.

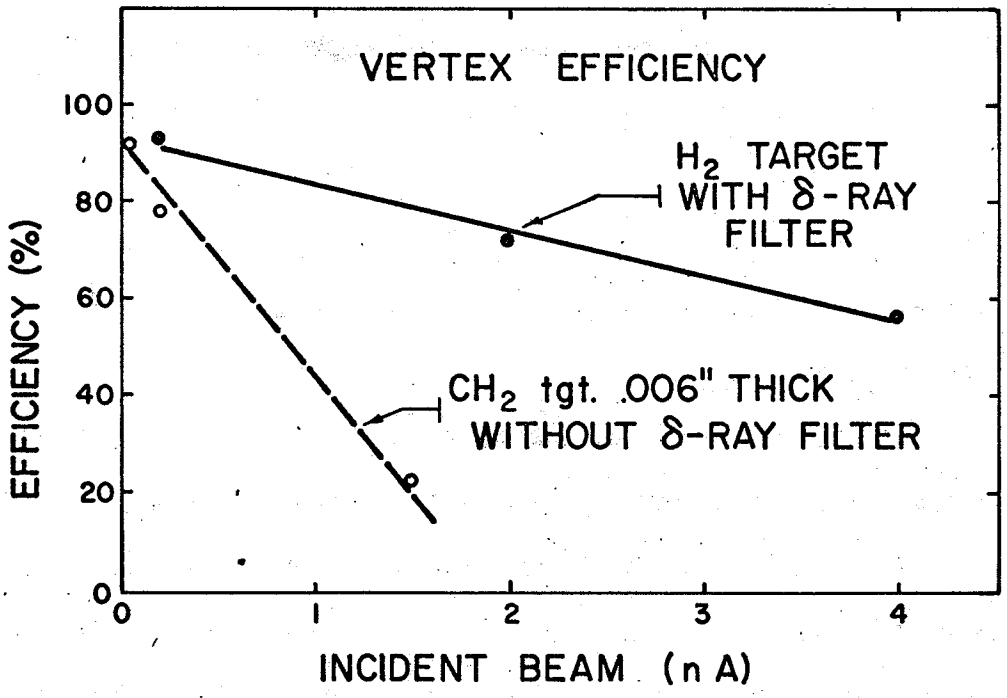
VERTEX EFFICIENCY
EFFICIENCY (%)
100
80
60
40
20
0
0
1
2
3
4
INCIDENT BEAM (n A)
H_2 TARGET WITH δ-RAY FILTER
CH_2 tgt. .006" THICK WITHOUT δ-RAY FILTER

The deterioration in overall efficiency at higher fluxes is attributed mainly to the robbing of the tracks giving the triggers.

The background to be expected from elastically scattered protons, delta rays and gamma rays was mentioned in Chapter I. The effect of delta rays is illustrated in Fig.IV.6. The chambers were triggered by coincidences from collimated elastic protons when a current of 1.5 nA was incident on the 0.006" thick CH_2 target. If the delta ray filter was removed the efficiency of the horizontal plane of the front right chamber dropped to 18% of its original peak value.

The independent contributions from delta rays and gamma rays were investigated by triggering the chambers at a rate of 60 times/sec with a pulse generator. The beam profile and geometry were those used for PPB data-taking with hydrogen gas as the target. A series of runs of 1,000 triggers each was taken at different beam currents under control of the PLNHST program. The integrated number of set cores on each plane was typed out on completion of each run. With the delta ray absorber completely removed the integrated values were found to be identical on both spectrometer arms. A 0.002" mylar foil sufficient to stop 50 KeV delta rays from reaching the front chamber, was then placed along the length of the beam so that the delta rays were filtered

on the left side but the right side remained open.

Fig.IV.7 shows how the number of set cores varies with the primary beam intensity. It is apparent that delta rays are sufficient to saturate the chambers almost completely at 1.0 nA. We know from Fig,IV.1 that on the pulsed planes over 90% of the sparks have single multiplicity, hence, we can conclude that approximately every trigger,which was a random trigger, produced a spark. The 0.002" mylar foil reduced the number of sparks by more than an order of magnitude at 0.1 nA and a factor of 4 at saturation. Some delta rays are obviously sufficiently energetic to penetrate the mylar and reach the front left chamber where saturation becomes complete at 10 nA. If it is desired to take data at higher currents the thickness of the mylar absorber can be increased at the expense of angular resolution.

Fig.IV.7 also shows that gamma rays produce a background within the chamber volume which create sparks on triggering the chambers. Runs were taken with brass plates positioned in front of the front chambers. These were sufficiently thick to stop protons from entering the hodoscopes. The wire chambers were triggered with the pulser as before. The open circles are data points taken with PLNHST under these conditions. They show that at 5 nA the number of sparks will reach 7.5%. The background level of gamma radiation between the front and rear chambers

Figure IV.6

Distribution of raw sparks for collimated elastic scattering for a 1.5 nA beam on a 0.006" CH_2 target showing the effect of delta rays and other pile-up tracks.

In figure (a) the delta ray filter, 0.001" thick, was in position and the chamber was triggered 5,000 times with scattered protons passing through a 1" collimator placed behind the rear wire chamber. As the beam had a ribbon type profile the sparks are localised in the horizontal plane but broad in the vertical plane.

In figure (b) the delta ray filter was removed and the efficiency of the horizontal plane dropped to 18% of its original peak value. The vertical and diagonal planes dropped to 70% and 55% respectively of their original peak values.

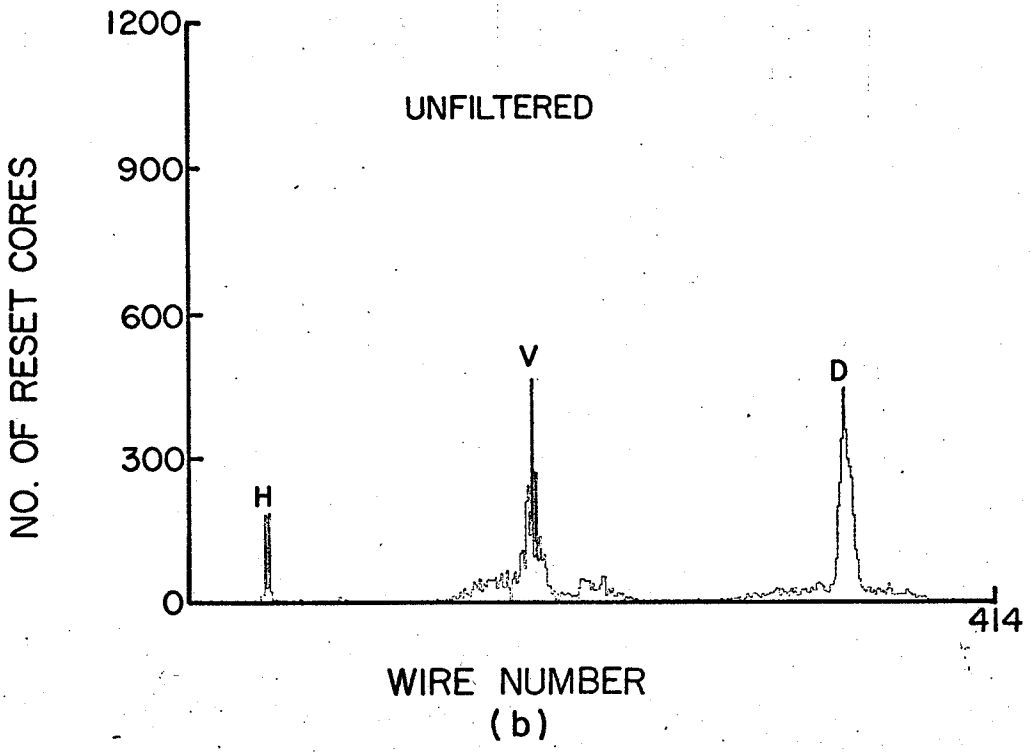
1200
900
600
300
0
NO. OF RESET CORES
UNFILTERED
H
V
D
414
WIRE NUMBER

(b)

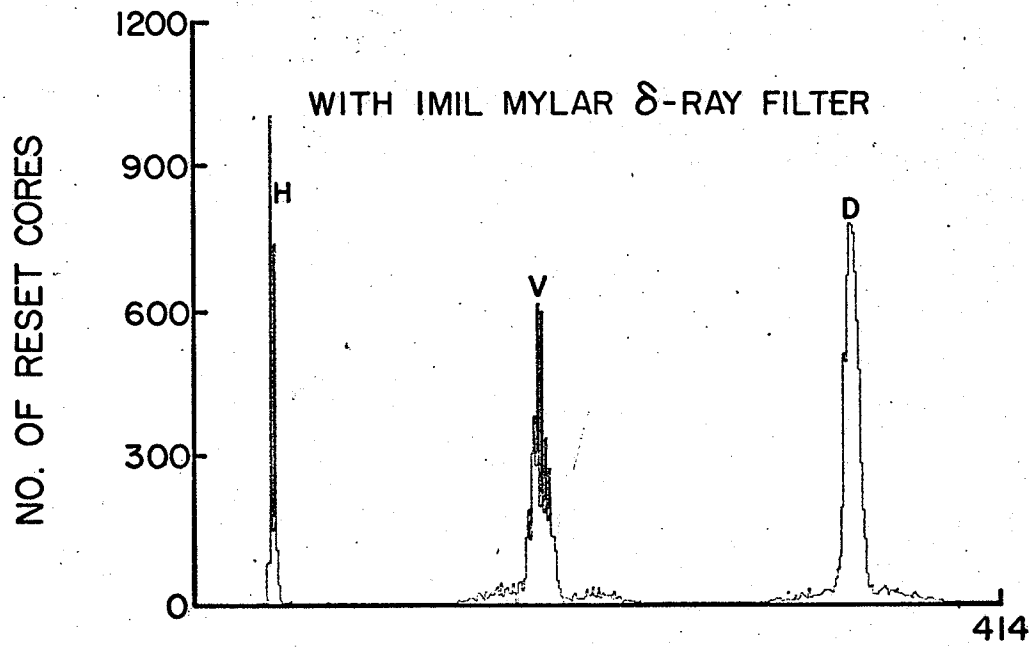
1200
900
600
300
0
NO. OF RESET CORES
WITH IMIL MYLAR δ-RAY FILTER
H
V
D
414
WIRE NUMBER

(a)

Figure IV.7

Spark contributions from delta rays, protons and gamma rays as a function of beam current.

Curve (a)(b) and (c) were taken with the chambers triggered with a pulse generator.

Curve (d) gives the number of cores set by the 'pile-up' tracks when the chambers were triggered by elastic proton coincidences under the control of the VERTEX program.

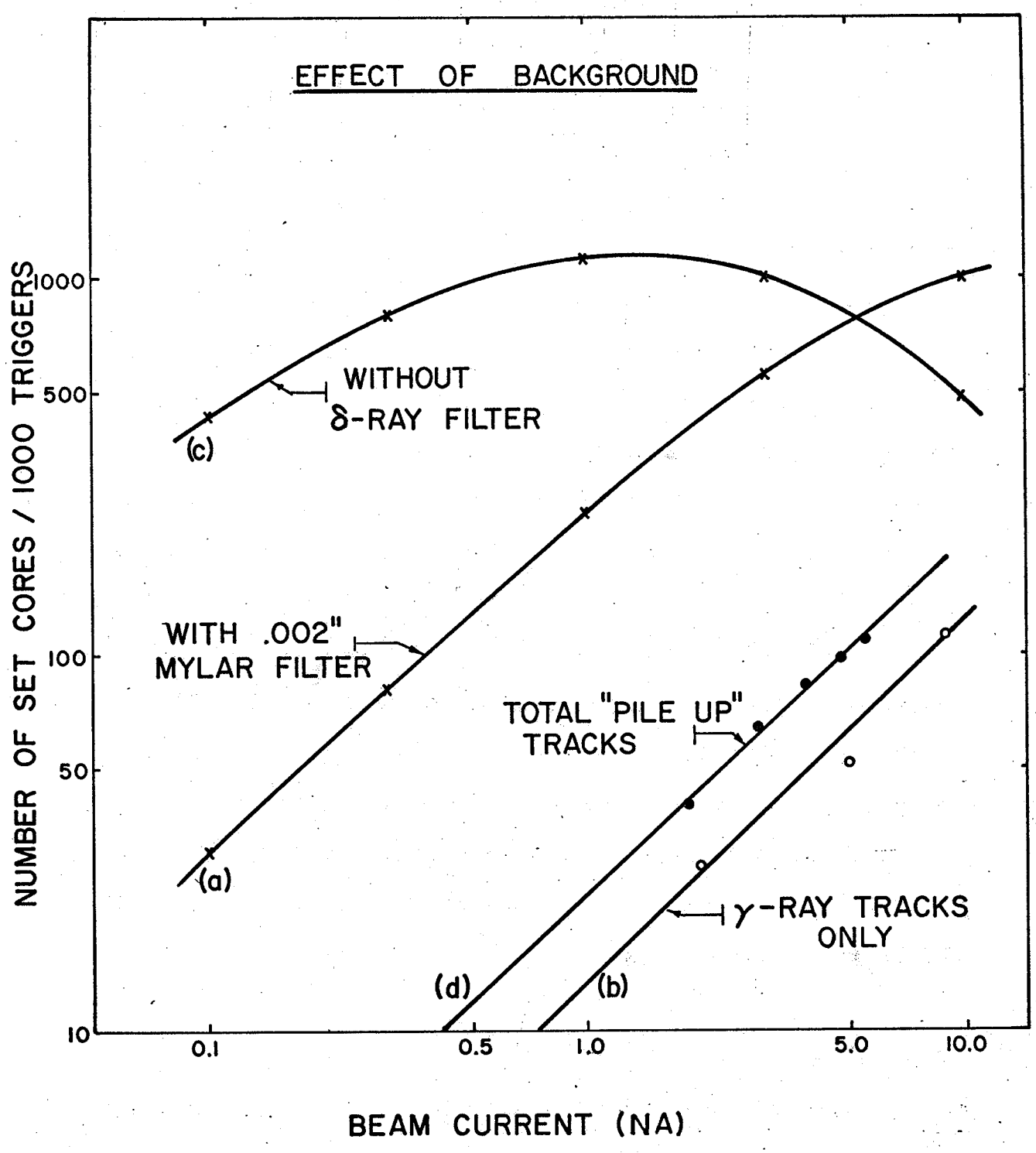
EFFECT OF BACKGROUND
NUMBER OF SET CORES / 1000 TRIGGERS
1000
500
100
50
10
0.1
0.5
1.0
5.0
10.0
BEAM CURRENT (NA)
WITHOUT
δ-RAY FILTER
(c)
WITH .002"
MYLAR FILTER
(a)
TOTAL "PILE UP"
TRACKS
γ-RAY TRACKS
ONLY
(d)
(b)

was measured with a gamma ray monitor and found to be 3 mR/hr/nA, when these data were taken.

Elastically scattered protons from the target gas are also a background problem in the PPB experiment. The target gas and beam profile were organised to simulate PPB data-taking conditions with a 0.002" mylar filter in position. The geometry and electronics were adjusted so that the chambers could be triggered by elastic proton coincidences under the control of the VERTEX program. The number of double tracks found in the front right chamber can be interpreted in terms of the number of set cores by referring to the multiplicities found for pulsed planes in Fig.IV.1. The curve with closed circles in Fig.IV.7 gives the variation of the 'pile-up' tracks with beam current. Protons, delta rays and gamma rays must all contribute. The decrease in the number of sparks from curve(a) to curve (b) can be attributed to the robbing of delta ray and gamma ray tracks by proton tracks. The number of greater-than-two-cluster events never exceeded 1% in these runs.

4.2 Geometry.

Optical alignment was used to position the primary geometric components in the transport system. The slits S_2, the final quadrupole doublet (Q_5 and Q_6) in Fig.II.1, the centre of the entrance and exit ports of the scattering chamber were adjusted to be colinear with the geometric

centre of the bending magnet. The scattering chamber was then firmly bolted to the 4 ft. square resting plate with lines drawn on the plate at 32.5° to the centre of the scattering chamber (the line normal to the wire chambers) and at 45° to a position 3" downstream from the centre of the chamber. In the latter position a CH_2 solid target was placed when it was desired to observed p-p elastic scattering.

The above procedure still allows 2 degrees of freedom in the precise determination of the geometry (in addition to the possible errors in optical alignment and the mechanical tolerance in the manufacture of the scattering chamber and wire chamber) namely the beam tuning conditions which determine the exact trajectory of the primary proton beam and the position of the rear chambers. The former was investigated by determining the beam position at the entrance and exit to the scattering chamber with the aid of the discoloration produced on perspex absorbers.

(a) Calibration from (p,p) scattering.

Facilities were provided for small controlled movements of the rear chamber along a line normal to the 32.5° line and the position of the rear wire chambers was determined to a first approximation with the aid of the 32.5° and 45° lines drawn on the plate. However, it was considerably more accurate to make use of the high

spatial resolution of the wire chambers. With a 39.5 MeV incident proton beam on the CH_2 target placed 3" downstream from the chamber centre, only those protons which were scattered through an 1/8" diameter collimating hole in a 1/2" aluminum plate, placed between the left rear wire chamber and the scintillation counter, were allowed to trigger the wire chambers. The beam was tuned so that a double focus resulted at the centre of the solid target and the protons detected in the right hodoscope necessarily followed a trajectory in the same plane as the collimating hole and the target centre.

Using the PLNHST program a run was taken in which histograms were formed of the raw sparks on each plane. The collimated arm showed well defined peaks covering 2 or 3 wires and although the peaks on the opposite arm were kinematically broadened it was possible to determine the centre of the peak to an accuracy of 1/2 a wire spacing without very much difficulty.

Fig.IV.8 shows the positions of the peaks in each of the four chambers for a typical run under these conditions. The beam and the left proton vector are in the horizontal plane but 0.7 ± 0.5 wire spacings higher than the mechanical centre. The vertical coordinate in the front right chamber is 0.3 ± 0.5 wire spacings low and this consistent with the fact that the geometric constants used in the VERTEX program required an asymmetry of 1/2 a wire spacing in order

to remove the asymmetry in the difference between the vertical intercepts with the Y-Z plane (vertical vertex error). Henceforth we shall refer to the Y-Z plane as the beam symmetry plane.

(b) Sensitivity of Geometric Constants by Calculation.

The outgoing protons from elastic p-p scattering must have vectors normal to each other and they must lie in the same plane as the vector of the incident particle. In this plane, however, the incident proton vector has a wide range of freedom and to remove this degeneracy it is necessary to investigate the intercept along the beam symmetry plane. There are 4 geometric constants required by the VERTEX program for calculation of the trajectory of the proton in each arm namely, for the right arm, P_1', P_2', $Q_3 - P_3$ and α (see Appendix B, Fig.B.1). It is necessary to determine the effect of these quantities independently and isolate those quantities which are important.

The effect of each constant for the elastic trajectories represented by Fig.IV.8 is shown in Table 2. The distance between the wire chambers, $Q_3 - P_3$ (called G in the Table), has an error of $\pm$ 0.005" and the angle which the normal to the wire chamber makes with the scattering chamber axis, α , has an error of $\pm$ 0.1°, hence the most critical parameter is the position of the rear chamber. This is controlled by the constants P_1' and P_2'. Investigation

Figure IV.8

Calibration of the geometry from (p,p) elastic scattering from a CH_2 target. The figure shows wire numbers for the centre of the peaks on each plane.

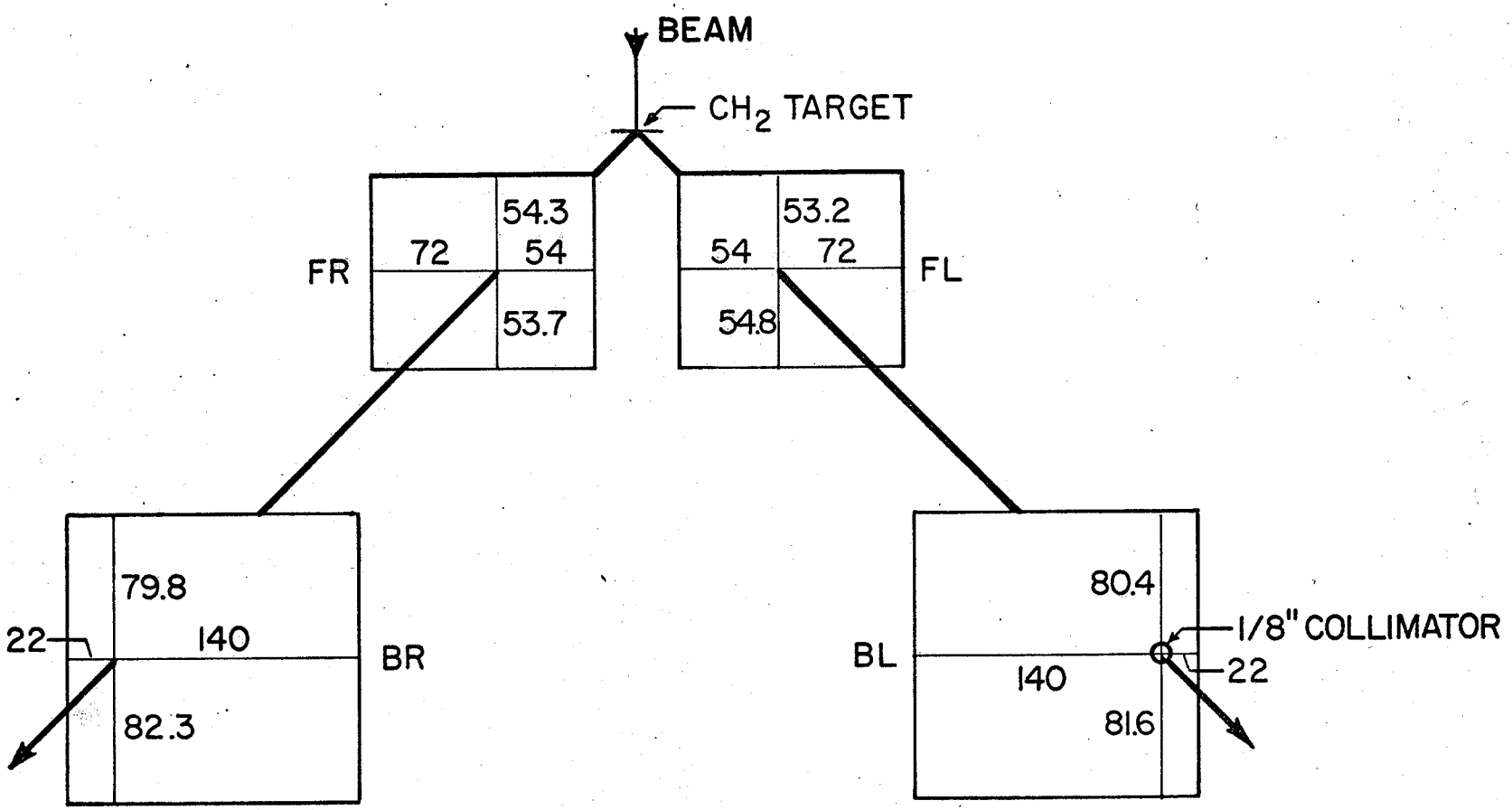
BEAM
CH_2 TARGET
54.3
72
54
FR
53.7
53.2
54
72
FL
54.8
79.8
22
140
BR
82.3
80.4
1/8" COLLIMATOR
BL
140
22
81.6

Table 2

The table shows the effect of variation in wire spacing,(P) (where P_1 is horizontal and P_2 is vertical), distance between the chambers,(G) and the angle, α , which the normal to the front chamber makes with the beam. All distances are in 1/2 wire spacings and angles are in degrees.

ELASTIC SCATTERING (COLLIMATED)

ANGLES ON WIRE SPACING		VERTEX INTERCEPT ON WIRE SPACING		EFFECT OF GAP (G)		EFFECT OF CHAMBER ANGLE	
$\frac{d\theta_1}{dP_1}$	$\frac{d\phi_1}{dP_2}$	$\frac{dY}{dP_2}$	$\frac{dZ}{dP_1}$	$\frac{d\theta_1}{dG}$	$\frac{dZ}{dG}$	$\frac{d\theta_1}{d\alpha}$	$\frac{dZ}{d\alpha}$
0.09	0.13	1.36	1.9	0.02	0.11	1.0	7.3

of the effect of these constants will show the dependence of angular and vertex resolution on the wire spacing in the front chamber.

The sensitivity of the polar scattering angle, Θ , the azimuthal angle, ϕ , the vertical coordinate, Y , and the beam coordinate, Z , to the spacing between the wires, is represented in Table 3. Proton trajectories were chosen from extreme parts of the reaction volume to extreme parts of the rear wire chamber so that Table 3 provides values for the limits of the variable dependence and the corresponding limits for θ and ϕ . The spatial resolution of the rear wire chamber will also contribute to the intercept uncertainty but, as will be shown in the next section the front chamber is more important. It is readily apparent from the value of 5.98 for dz/dP_1 at 15.7° that at small angles the intercept with the Z axis is very highly geared and any geometric error will be greatly accentuated in these cases.

(c) Tests using D(p,2p)N scattering.

The validity of this analysis and the values presented in the Tables 2 and 3 were tested by systematically varying the constants in the VERTEX program and processing a sample of 2,000 raw D(p,2p)N events obtained when the scattering chamber was filled with hydrogen enriched with deuterium gas. The variation in the inter-

cept with the beam symmetry plane and P_1' and P_2' are presented in Fig.IV.9(a) and (b). Events were accepted from all points in the reaction volume and in the polar angular range from 15^o to 37^o. The curves show that to first order the plane intercepts, called in the figure the average vertex error, in the horizontal and vertical directions are decoupled. The slopes of the curves give the horizontal and vertical intercept dependence and these are 2.55 and 1.40 respectively.

The smooth curves in Fig.IV.9 (c) and (d) show how this dependence on wire spacing varies along the reaction volume calculated for specimen trajectories which are incident normally on the wire chambers. As the solid angle increases with Z a weighted mean must be taken in placing the data point from Fig.IV.9 (a) on to (c). The agreement is satisfactory. The situation is more complicated for the horizontal intercept as in this case there is also a dependence on the polar scattering angle, θ , (see next section) and a weighted mean must be taken of both Z and θ . Here again the agreement is considered satisfactory.

4.3 Geometric Resolution.

Multiple scattering and the spatial resolution of the wire chambers are the causes of the uncertainty in the determination of the initial direction of the scattered proton. They contribute to the angular resolution and

Table 3

The sensitivity of the vertical and beam coordinates to the spacing between the wires in the front chamber for some extreme trajectories from the centre of the scattering chamber and 3" upstream from the centre. The limits of the polar scattering angle, θ , and the azimuthal angle, ϕ , are given for these trajectories. All distances are expressed in units of 1/2 wire spacings and angles in degrees.

TARGET POSITION	Z	EXTREME POSITION IN REAR CHAMBER	ANGLES ON WIRE SPACING				VERTEX INTERCEPT ON WIRE SPACING				LIMIT IN θ	LIMIT IN ϕ
			$\frac{d\theta_1}{dP_1}$	$\frac{d\theta_1}{dP_2}$	$\frac{d\phi_1}{dP_1}$	$\frac{d\phi_1}{dP_2}$	$\frac{dY}{dP_1}$	$\frac{dY}{dP_2}$	$\frac{dZ}{dP_1}$	$\frac{dZ}{dP_2}$		
CENTRE OF SCATTERING CHAMBER	137	MEDIAN PLANE NEAREST BEAM	0.088	0.001	0.0	0.31	0.0	1.53	4.99	0.0	17.3 MIN.	0.0
	137	TOP CORNER NEAREST BEAM	0.076	0.047	0.121	0.21	0.882	1.53	4.99	0.0	20.6 MIN.	34.12
	141	MEDIAN PLANE FURTHEST FROM BEAM	0.095	0.001	0.0	0.16	0.0	1.53	2.53	0.0	37.15 MAX.	0.0
	141	TOP CORNER FURTHEST FROM BEAM	0.089	0.024	0.041	0.14	0.446	1.53	2.53	0.0	38.7 MAX.	19.0
3 INCHES UPSTREAM FROM CENTRE	21	MEDIAN PLANE FURTHEST FROM BEAM	0.095	0.001	0.0	0.17	0.0	1.70	3.12	0.0	33.1 MAX.	0.0
	34	MEDIAN PLANE NEAREST BEAM	0.087	0.001	0.0	0.34	0.0	1.68	5.98	0.0	15.67 MIN.	0.0

Figure IV.9

The figure shows the results of systematically varying the geometric constants controlling the position of the spark coordinates in the front chamber. For the tests a small data sample of 2,000 (p,2p) events from a deuterium gas target was processed for different values of P_1' and P_2' (see Fig. B.1 for notation). The intercepts (or average vertex errors) of the proton trajectories with the beam symmetry plane are plotted as a function of P_1' and P_2' in (a) and (b). The slopes of these curves are compared with calculated variations of the intercepts along the reaction volume in (c) and (d).

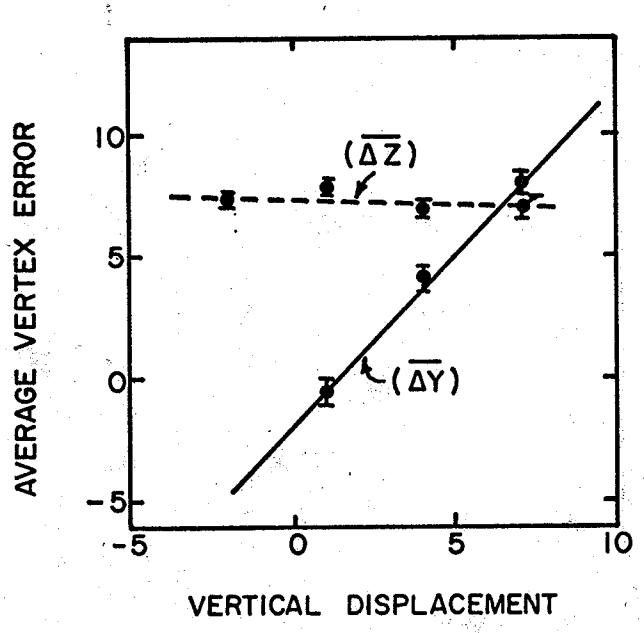
AVERAGE VERTEX ERROR
10
5
0
-5
(ΔZ)
(ΔY)
-5
0
5
10
VERTICAL DISPLACEMENT

(a)

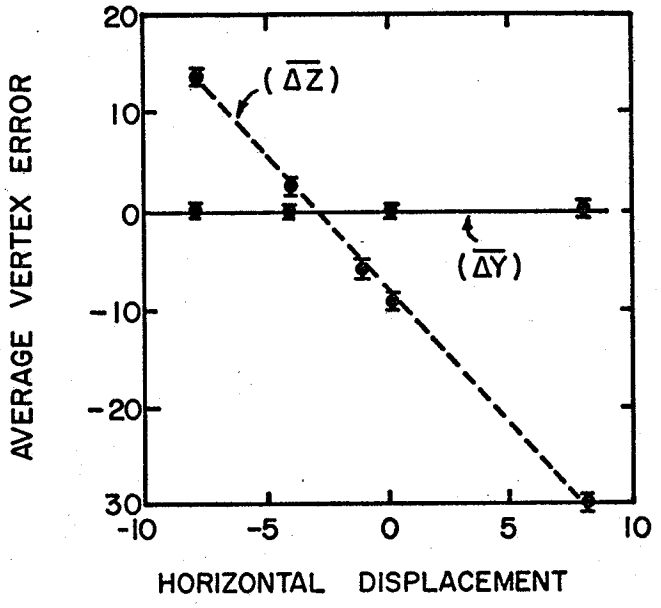
AVERAGE VERTEX ERROR
20
10
0
-10
-20
30
(ΔZ)
(ΔY)
-10
-5
0
5
10
HORIZONTAL DISPLACEMENT

(b)

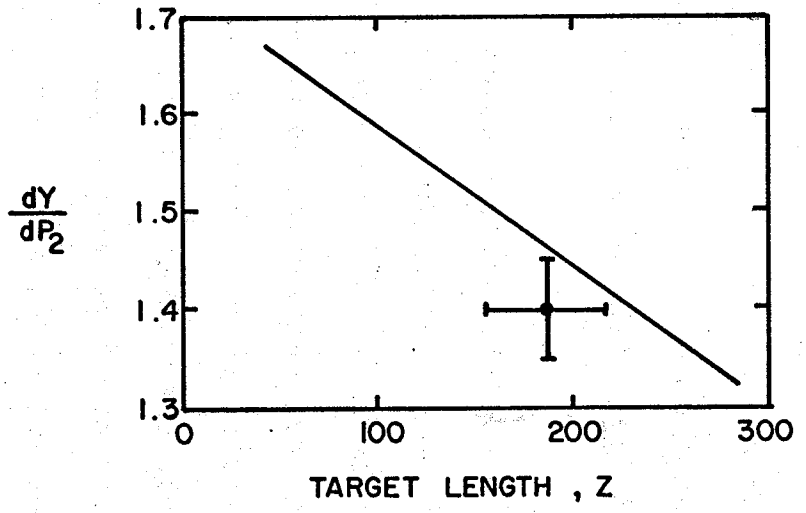
dY/dP2
1.7
1.6
1.5
1.4
1.3
0
100
200
300
TARGET LENGTH , Z

(c)

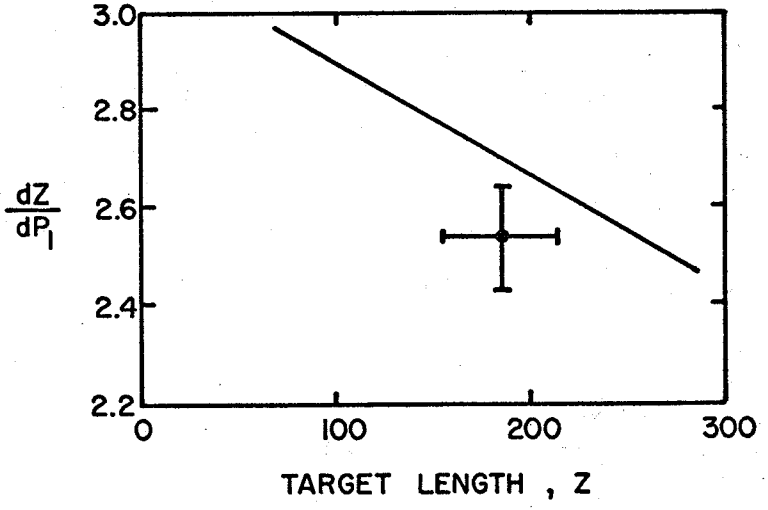
dZ/dP1
3.0
2.8
2.6
2.4
2.2
0
100
200
300
TARGET LENGTH , Z

(d)

vertex uncertainties in quite different ways. The calculations for the RMS of the projected angle of multiple scattering, $\langle\theta\rangle_M$, are based on the following formula first derived by Rossi and Griesen[25].

$$\langle\theta\rangle_M = \frac{E_s}{2\,E_{KE}}\sqrt{\frac{t}{X_o}}\,(1+\mu)$$

where

E_s = 15 MeV.

t = thickness in gm/cm^2.

X_o = radiation length in gm/cm^2 .

μ = is a small correction for thin foils[26].

E_{KE} = kinetic energy expressed in MeV.

The spatial resolution of the wire chambers which is a function of the width of the spark and the number of wires per unit length was discussed briefly in section 4.1.

(a) Angular Resolution.

Measurement of the angular resolution is complicated by the fact that there is horizontal divergence in the beam direction which is comparable to the uncertainty in the scattered proton track. However, observation of both elastically scattered proton tracks from a hydrogen gas target permits a measurement of the intrinsic angular resolution of the hodoscope arms combined. Fig.IV.10 shows a histogram of the sum of the two polar angles for an incident energy of 42 MeV. A ribbon beam profile was used

with hydrogen gas as the target. The delta ray filter was not in position. A coarse vertex error accepted tracks which had a vertex error of $\pm$ 1" in both the vertical and beam directions. The histogram is distributed about the mean value of 89.4° and as it may be assumed that the uncertainties from each arm add in quadrature the intrinsic angular resolution is 0.32° HWHM. The tails in the distribution are thought to be due to either multiple scattering in the chamber wires or the acceptance of sparks caused by delta rays.

From Table 2 the contribution to $\Delta\theta$ from the wire spacing in the front chamber is 0.09°, hence the standard deviation for the uncertainty due to both front and rear chambers is $\sqrt{2}$ x 0.09° = 0.13°. From Fig.II.6 the RMS projected angle of multiple scattering at 21 MeV is 0.26° and summing the expected errors from multiple scattering and spatial resolution gives an expected value for the angular resolution of

$$\langle\theta\rangle = \left[\langle\theta\rangle_M^2 + \langle\theta\rangle_w^2 \right]^{\frac{1}{2}} = 0.29^\circ$$

This is in reasonable agreement with the measured value of 0.32° at this energy.

The effect of the wire spacing of the chambers on the angular resolution can be observed in Fig.IV.11. Here the proton beam was incident on a CH_2 target and only protons elastically scattered from hydrogen and passing

Figure IV.10

The figure shows the distribution of the measured sum of the scattering angles of two protons from (p-p) elastic scattering for an incident proton energy of 42.0 MeV and H_2 gas as the target. From this curve it follows that the angular resolution of each arm of the spectrometer for 21.0 MeV protons is $\pm$ 0.45°/$\sqrt{2}$ = $\pm$ 0.32°. For this measurement the delta ray filter was not in position and a 'coarse' vertex limit of $\pm$ 1" in the vertical and beam directions was used. The tails are due to pile-up tracks and scattering from the wires in the front chamber.

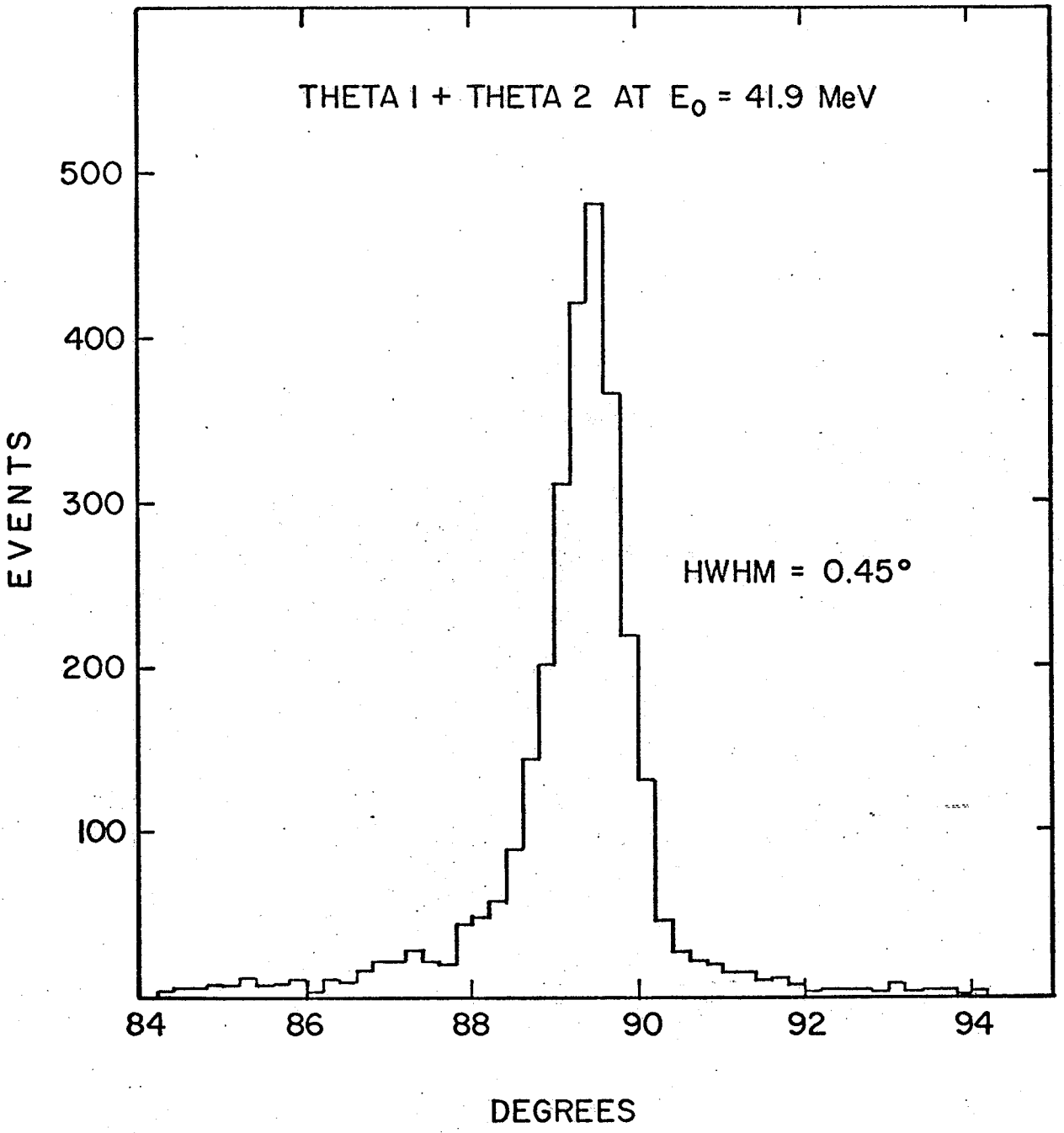
THETA 1 + THETA 2 AT E_0 = 41.9 MeV
HWHM = 0.45°
EVENTS
500
400
300
200
100
84
86
88
90
92
94
DEGREES

Figure IV.11

The effect of wire spacing and geometric broadening on ϕ_1, and ϕ_2, from elastic scattering tightly collimated on one side only. The histogram has a bin size of 0.1° on top of which the chamber resolution is superimposed.

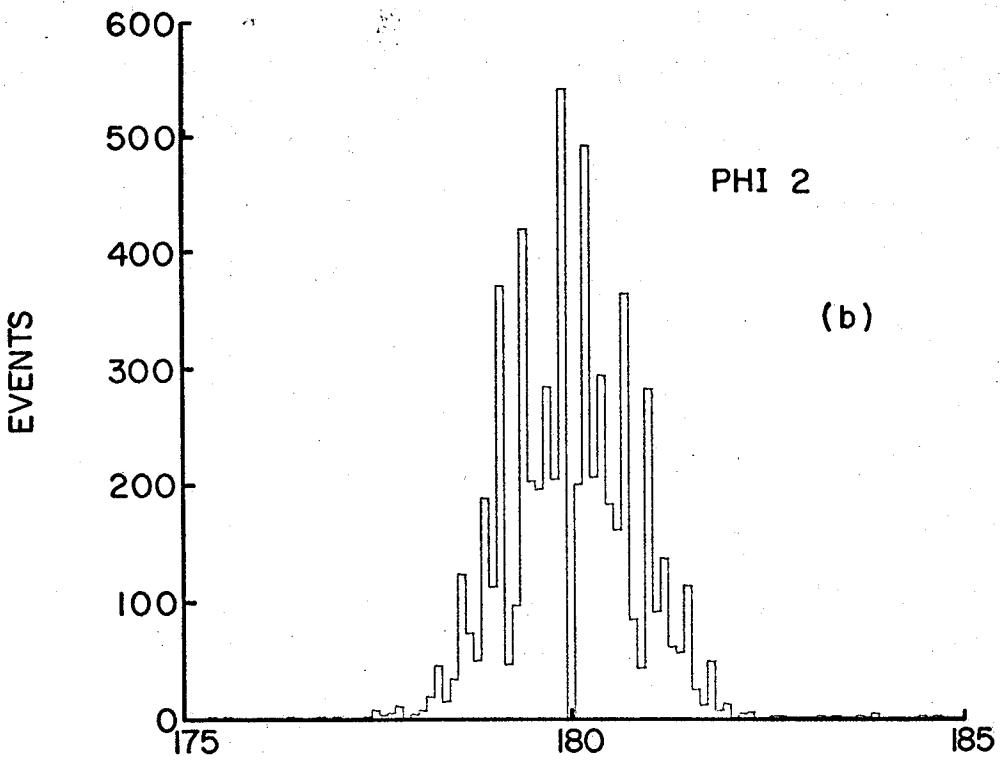
600
500
400
300
200
100
0
EVENTS
PHI 2
(b)
175
180
185
AZIMUTHAL ANGLE (DEGREES)

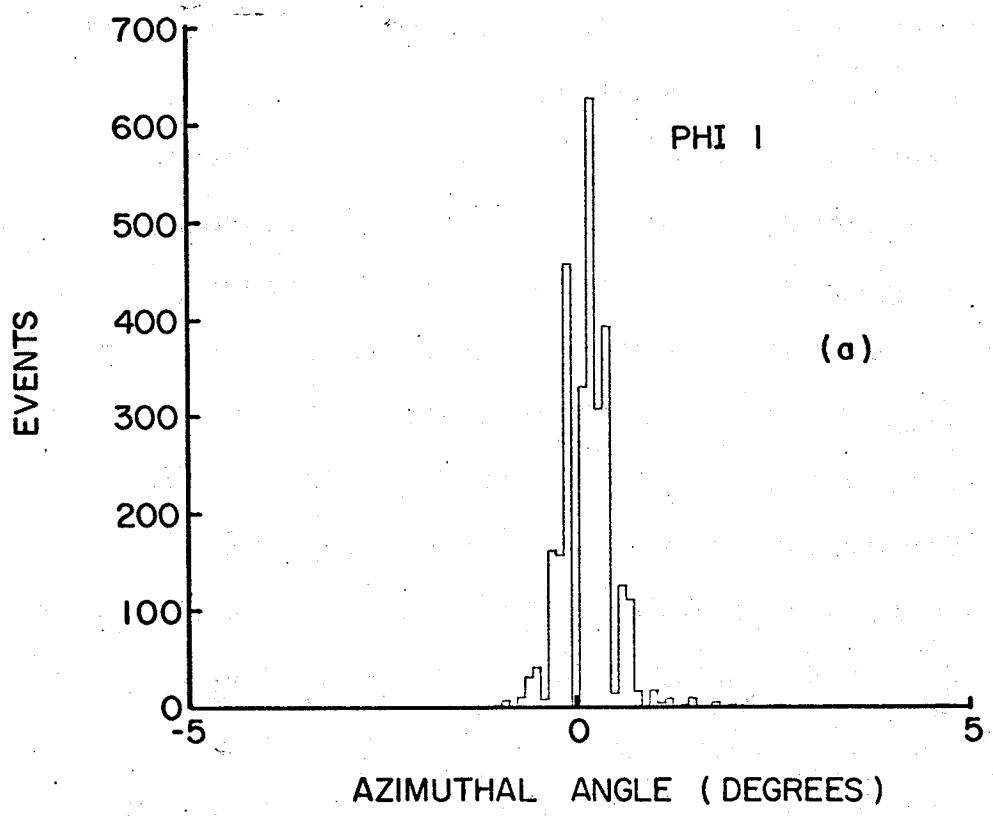
700
600
500
400
300
200
100
0
EVENTS
PHI 1
(a)
-5
0
5
AZIMUTHAL ANGLE (DEGREES)

through a 1/8" collimating hole on the left side of the beam in the median plane were allowed to trigger the chambers. Fig.IV.11(a) shows the distribution in , ϕ_1 , where the discrete nature of the distribution is superimposed on the histogram bin size of 0.1°. Fig.IV.11(b) shows the histogram of, ϕ_2 . This side of the spectrometer was uncollimated and the histogram is centred at 180° as required by elastic scattering. The discrete nature may again be observed in the distribution broadened by the finite beam width and the geometric resolution.

(b) Vertex Uncertainty.

The spectrometer was designed with good geometric definition mainly to minimise the vertex uncertainty so that good rejection of background could be achieved in the PPB experiment. Fig.IV.12(a) gives the difference in the vertical intercepts of the left and right track with the beam symmetry plane for the outgoing protons from p-p elastic scattering created 2"-3" downstream from the chamber centre. The vertical vertex error is independent of beam width, target thickness and possible beam misalignment for events in the median plane, therefore it represents a figure of merit of the spectrometer. Fig.IV.12 (b) gives the distribution in the horizontal vertex error i.e. the difference in the horizontal intercepts of the left and right tracks with the beam symmetry plane in

the chamber. This error is dependent on the beam width and the precise centering of the beam. The equations used in the calculation of these errors as intercepts with the symmetry plane of the chamber are given in Appendix B.

If a line drawn normally to the wire chamber from an origin in the reaction volume, intersects the delta ray filter at X_1 the diagonal plane of the front chamber at X_2 and the diagonal plane of the rear chamber at X_3, then the uncertainty $(\Delta y)_M$ in the intercept with the beam symmetry plane due to multiple scattering is given by

$$(\Delta y)_M = \left[\left(\langle\theta\rangle_\delta \times X_1 \right)^2 + \left(\langle\theta\rangle_{H_2} \times \frac{X_2}{2} \right)^2 + \left(\langle\theta\rangle_{FC} \times X_2 \right)^2 + \left(\langle\theta\rangle_{He} \frac{X_3}{2} \right)^2 \right]^{\frac{1}{2}} \quad (1)$$

where $(\Delta y)_M$ is an uncertainty of one standard deviation assuming a Gaussian distribution and $\langle\theta\rangle_\delta$, $\langle\theta\rangle_{H_2}$, $\langle\theta\rangle_{FC}$, $\langle\theta\rangle_{He}$ are the RMS projected angles for the delta ray filter, hydrogen gas, front wire chamber and helium bag respectively. The equation shows that mass, which is important when angular resolution is considered, becomes relatively unimportant when the vertex errors are considered. This is especially the case with the delta ray filter as X_1 is only 1.0" and $\langle\theta\rangle_\delta$ is independent of distance for a given angle. It therefore contributes little to the vertex uncertainty.

There is a random source of error due to the spatial resolution of the chambers. In addition, as the program refers the coordinates to a plane and ignores the spacing

Figure IV.12

The distribution in the vertex error i.e. the difference in the intercepts of the left and right track with the vertical symmetry plane in the chamber. The vertical vertex error is independent of the beam width, target thickness and possible beam misalignment. The horizontal vertex error is dependent upon the above factors and the data presented from curves are for elastic scattering at 42 MeV.

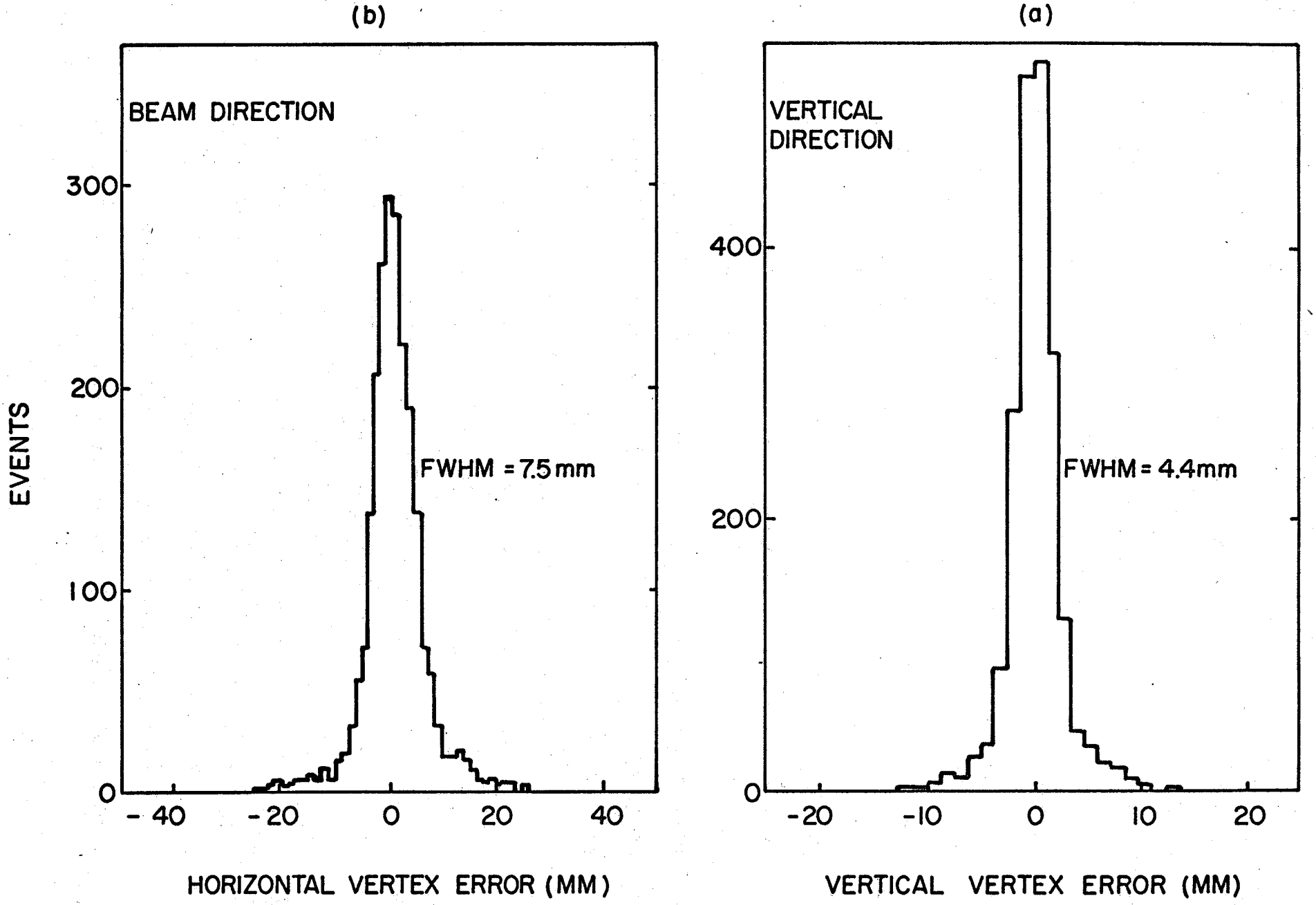
(b)
BEAM DIRECTION
300
200
100
0
EVENTS
FWHM = 7.5 mm
-40
-20
0
20
40
HORIZONTAL VERTEX ERROR (MM)
(a)
VERTICAL
DIRECTION
400
200
0
FWHM = 4.4mm
-20
-10
0
10
20
VERTICAL VERTEX ERROR (MM)

between the chamber planes there is a systematic source of error which has a value of approximately 1/2 wire spacing in the extreme case when the particle is incident at 12^{o} to the normal of the wire chamber. The contribution to the vertical vertex error from spatial resolution is

$$(\Delta y)_w^2 = \frac{\Delta s^2}{(X_3 - X_2)^2} \left(X_2^2 + X_3^2\right) \qquad \ldots\ldots\ldots\ldots(2)$$

where ΔS = is the error in coordinate determination in each chamber. As X_1, X_2 and X_3 are functions of the position along the reaction volume the vertex error will be a function of Z. Fig.IV.13(a) shows how each term in equation (1) and how equation (2) depends on Z. The term containing $\langle\theta\rangle_s$ is neglected. The significant point to note is that the effect of wire spacing in the chamber is now the dominant factor for this geometry, whereas with angular resolution, multiple scattering was dominant.

A test of the above calculations was performed by investigation of (p,2p) events from deuterium break-up. The amount of D_2 gas in the scattering chamber was increased and the events were fully processed through the VERTEX and KINEMATICS programs. Using the CORRELATE program events were selected on vertex position within the reaction volume and the FWHM of the vertical vertex error curve obtained. After division by $\sqrt{2}$ the uncertainty in intercept is plotted as a function of Z. Although most of the experimental points lie above the expected curve the agree-

ment should be considered as good in view of the approximations used.

The horizontal vertex error, ΔZ , is related to the vertical vertex error Δy by

$$\Delta Z = \frac{\Delta y}{\sin \theta}$$

The two curves plotted in Fig.IV.13(b) are plotted for two positions along the reaction volume. The above data was selected on both Z and θ and the widths of the horizontal vertex errors investigated. These vertex errors are dependent on the width of the beam and the precise centering of the beam along the beam symmetry plane. The analysed data had a bias from the zero position of 0.125" and the widths are therefore correspondingly larger than their optimum values. Nevertheless, the dependence of ΔZ on θ follows the general shape of the curves.

4.4 Energy and Momentum Resolution.

The energy resolution of the spectrometer is of special interest particularly as the third particle in the final state is not detected. In (p,2p) reactions the binding energy can be measured by calculating the total change in kinetic energy caused by the reaction. Likewise in PPB the energy of the photon may be obtained from momentum conservation where the angular resolution is also folded in, or directly from energy conservation. In this section we consider the experimental properties of both methods.

Figure IV.13

Dependence of vertex uncertainty on vertex position and angle.

(a) The individual contributions from multiple scattering in the target gas, front wire chamber and helium bag, to the FWHM vertical vertex error, Δy, is plotted as a function of the distance, Z, from the origin in the beam direction. The independent contribution from the spatial resolution in both the front and rear chambers is also plotted as a function of Z. Their quadrature sum is compared with experimental points obtained from deuteron break-up in deuterium enriched hydrogen gas. Each point represents the $\sqrt{2}$ x FWHM of the vertical vertex error of events selected from 3.18 cm long sections in the reaction volume.

(b) The horizontal vertex error is also a function of θ and is related to ΔY by $\Delta Z = \Delta Y / \sin\theta$. The two smooth curves are the expected variation of ΔZ with θ for Z = 6.25 cm and Z = 13.0 cm. The data points show the observed variation with θ. The systematic displacement is due to an asymmetry in ΔZ caused by a displacement of the beam during this run from the beam symmetry plane.

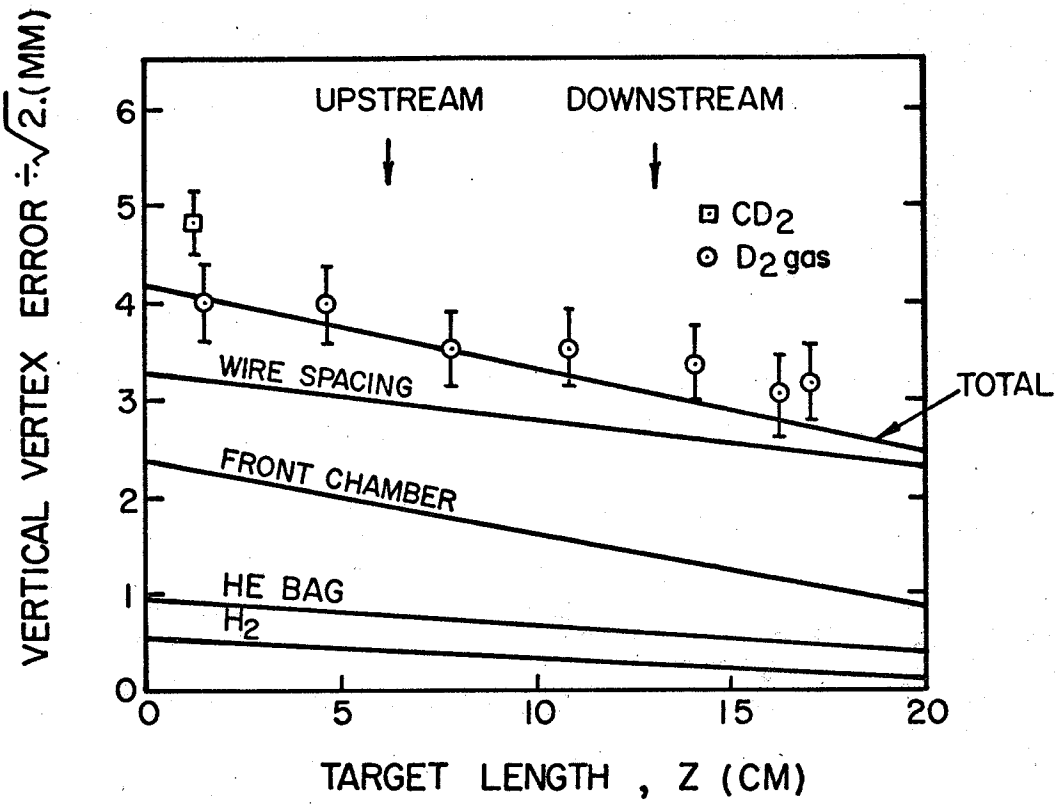
VERTICAL VERTEX ERROR ÷√2.(MM)
UPSTREAM
DOWNSTREAM
CD2
D2 gas
WIRE SPACING
TOTAL
FRONT CHAMBER
HE BAG
H2
0
1
2
3
4
5
6
0
5
10
15
20
TARGET LENGTH , Z (CM)

(a)

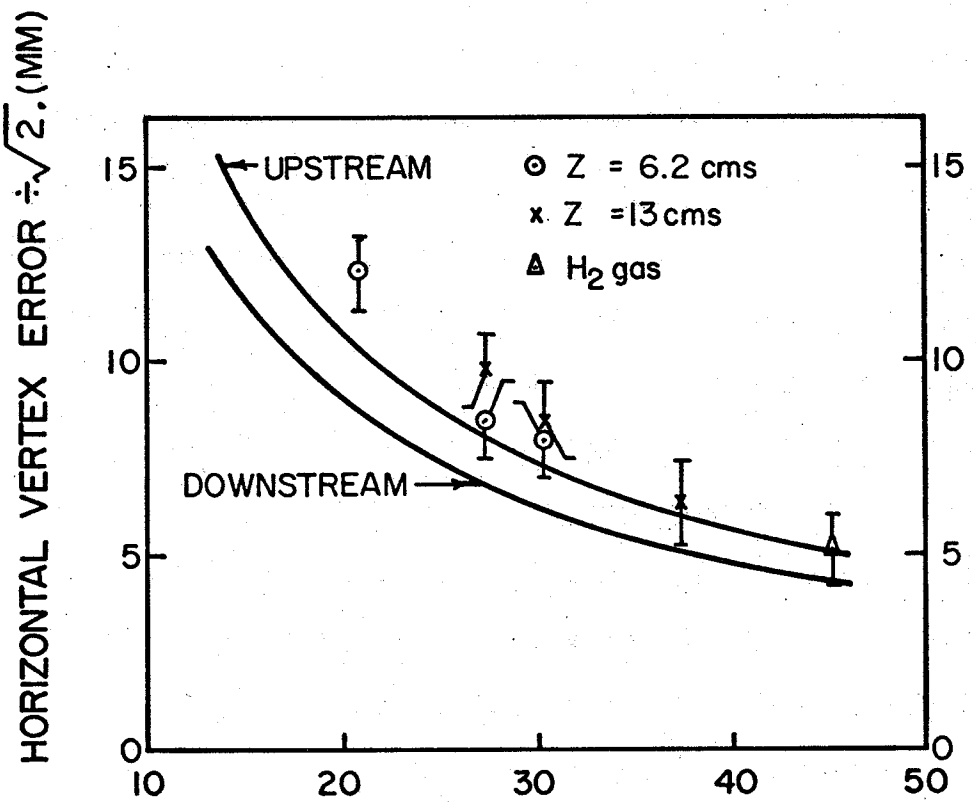
HORIZONTAL VERTEX ERROR ÷√2.(MM)
UPSTREAM
Z = 6.2 cms
Z =13 cms
H2 gas
DOWNSTREAM
0
5
10
15
10
20
30
40
50
THETA (DEGREES)

(b)

(a) Energy Conservation.

The pulse height calibration of the scintillation counters was performed by three independent methods. Calibration points were provided by :-

(i) elastic scattering from hydrogen and carbon in a CH_2 target. The incident beam energy was varied but the scattering angle remained constant.

(ii) allowing scattered protons to pass through various thicknesses of aluminum absorbers.

(iii) inelastic scattering from ^{12}C.

The pulse height is a function of the position where the proton strikes the scintillator due mainly to light absorption in the scintillator. The spread of 15% is reduced by storing a two dimensional correction matrix in the 360/65 computer and the computer uses this array with the coordinate information from the rear wire chambers during event analysis. The correction matrix is obtained from the off-line analysis of data taken when the chambers were sparked on random coincidences from protons elastically scattered from a tantalum target. The pulse height resolution for 22.2 MeV protons collimated at the centre of the counter was measured to be 2.2% HWHM and the uncollimated corrected resolution for 42 MeV protons scattered from a 0.001" thick Ta target was 3.1% HWHM. Full details of these results and procedures used in calibration are discussed in reference [18].

In order to measure the spectrometer resolution in the computed photon energy, E_γ, we analysed p-p scattering data as if they were due to a 3 body final state process. The histogram in Fig.IV.14 shows the distribution obtained. From these results it follows that the energy of the third particle can be obtained with an accuracy of $\pm$ 1.5 MeV at zero energy.

Let the energy of the third particle, E_γ, be given by

$$E_\gamma = E_o - (E_1 + E_2)$$

If the uncertainty in the energy determination of each outgoing proton ΔE obeys the relationship

$$\Delta E = a\, E^{\frac{1}{2}}$$

where 'a' is the resolution coefficient of the counter. Then for identical counters

$$\Delta E_\gamma = \left[(\Delta E_o)^2 + a^2\,(E_1 + E_2)\right]^{\frac{1}{2}}$$
$$= \left[(\Delta E_o)^2 + a^2\,(E_o - E_\gamma)\right]^{\frac{1}{2}}$$

Fig.IV.15 shows the expected dependence of the resolution ΔE_γ on the energy of the third particle using energy conservation.

(b) Momentum Conservation.

By measurement of the vector momentum of both protons, the recoil nucleus or gamma ray momentum is then found by conservation of momentum. Besides allowing the

Figure IV.14

In order to measure spectrometer resolution in the computed photon energy, p-p elastic scattering data are analysed as if they are due to the PPB process. The histogram shows the distribution obtained.

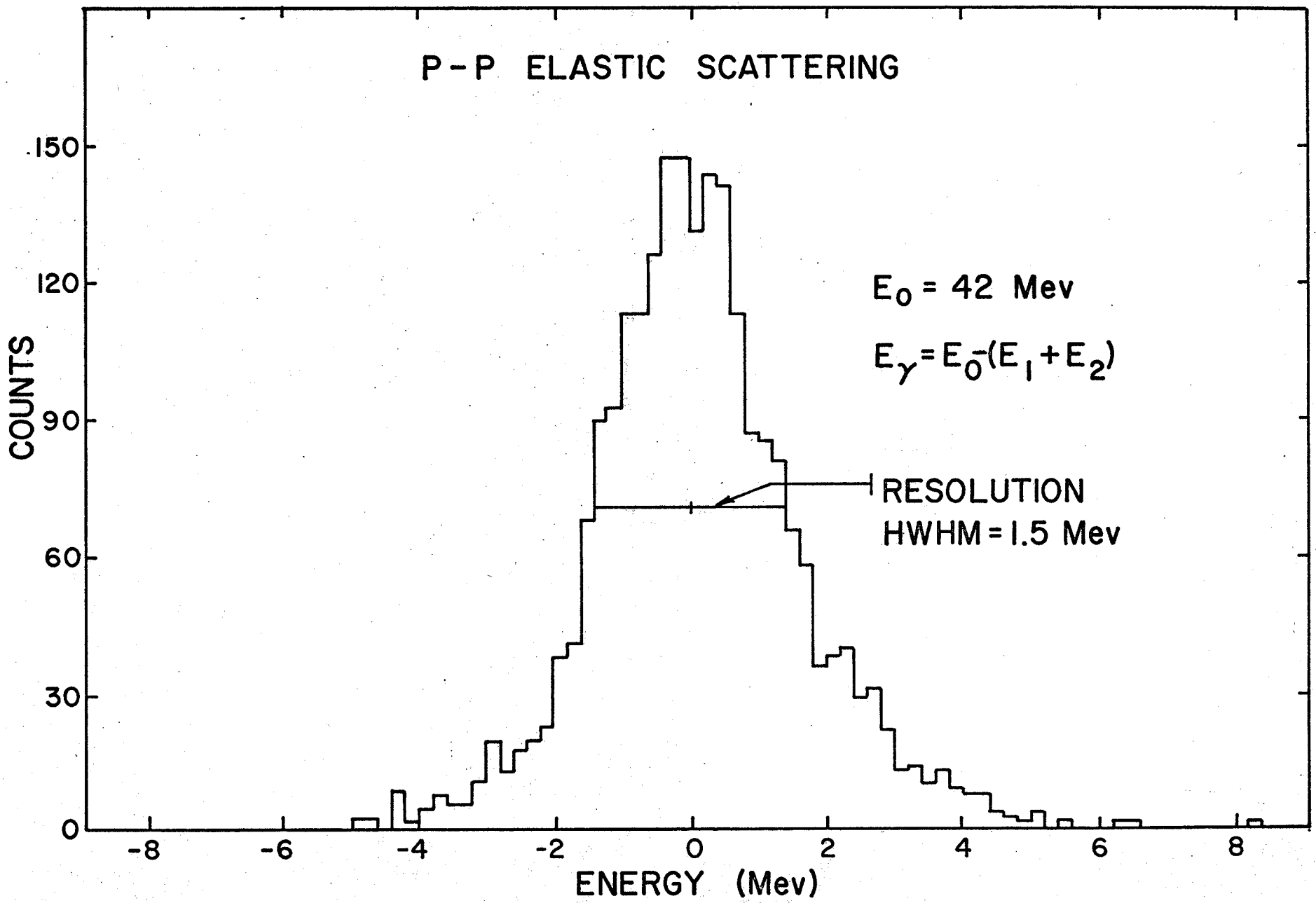
P-P ELASTIC SCATTERING
COUNTS
150
120
90
60
30
0
-8
-6
-4
-2
0
2
4
6
8
ENERGY (Mev)
E_0 = 42 Mev
$E_\gamma = E_0 - (E_1 + E_2)$
RESOLUTION
HWHM = 1.5 Mev

Figure IV.15

Expected and measured variation of the uncertainty in the photon energy with the incident energy from energy conservation. The curve represents the expected variation normalised to the measured value of the uncollimated scintillation counter resolution. The data points were obtained by analysing p-p scattering as PPB. The 3.8 MeV point was obtained when the beam had a ribbon profile and one counter was collimated but the other counter was open. The point at 8.0 MeV was taken with the counters completely exposed.

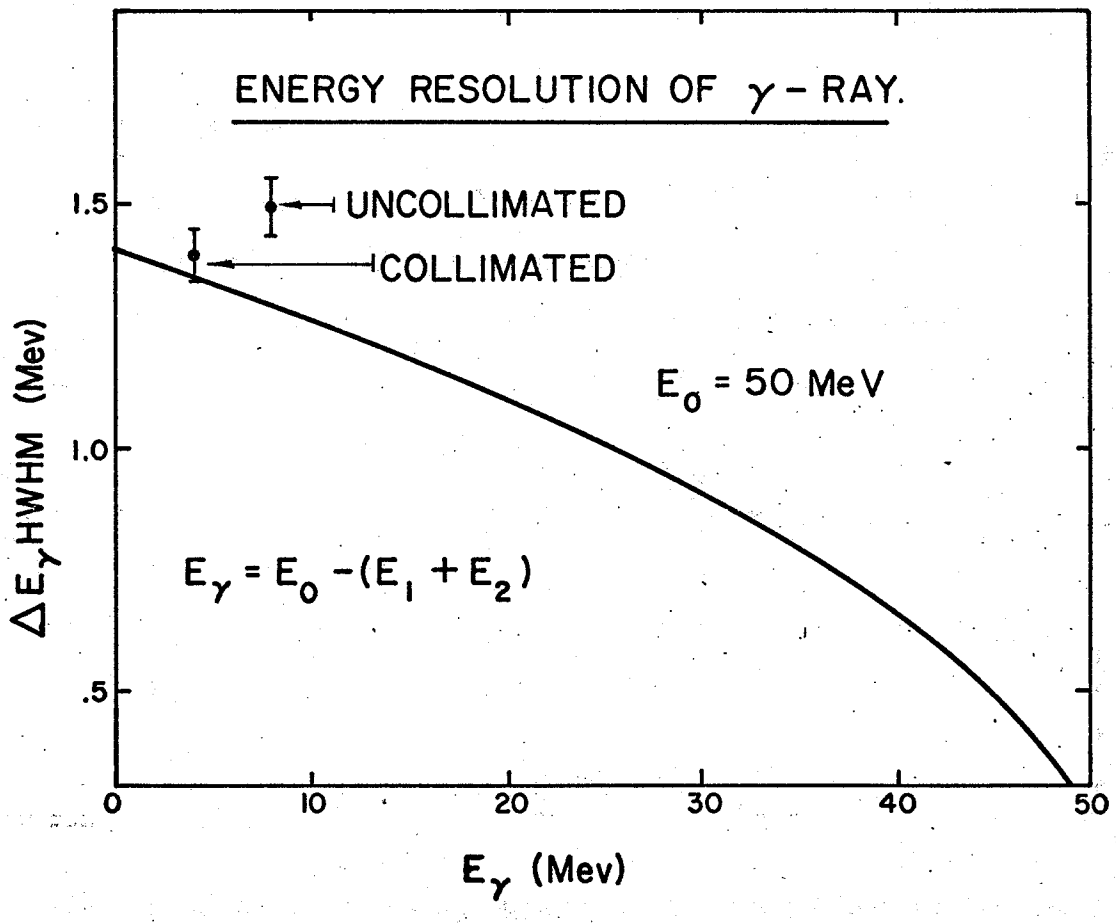
ENERGY RESOLUTION OF γ - RAY.
UNCOLLIMATED
COLLIMATED
E_0 = 50 MeV
$E_\gamma = E_0 - (E_1 + E_2)$
ΔE_γ HWHM (Mev)
1.5
1.0
.5
0
10
20
30
40
50
E_γ (Mev)

angular distributions of the third particle to be determined, the final state energy obtained by this process can be compared with the incident total energy. This procedure allows a "goodness of fit" parameter to be defined. (See section 3.3(b))

P-p elastic scattering data was again processed as a three body final state process and the vector components of the unmatched momenta shown in Fig.IV.16 demonstrate the resolution of the system in recoil momentum space. The resolution of E_γ by momentum conservation compounds to be 3.5 MeV/c at HWHM when E_o = 46.2 MeV.

Figure IV.16

The spectrometer momentum resolution has been measured by analysing p-p scattering at 46.2 MeV as if it was due to the PPB process. Figs. (a), (b) and (c) give the distribution of the momentum components of the "third" particle after analysis as a PPB process.

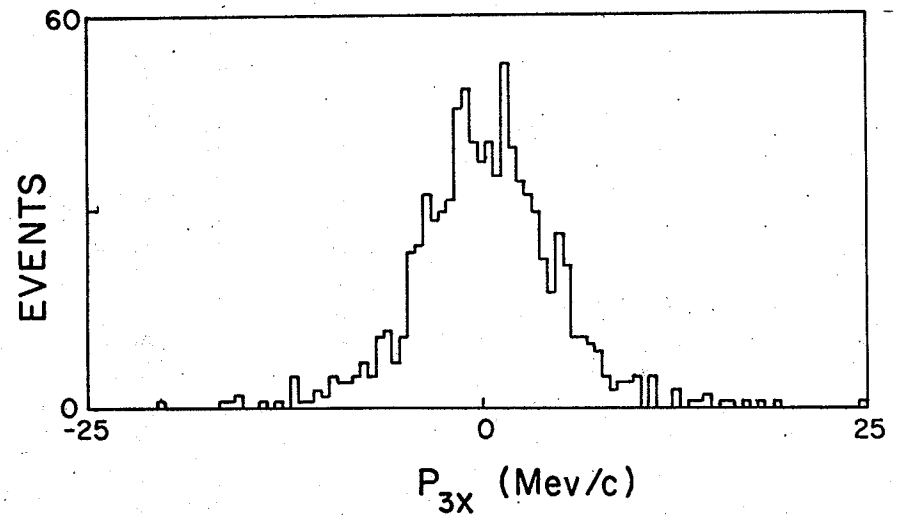

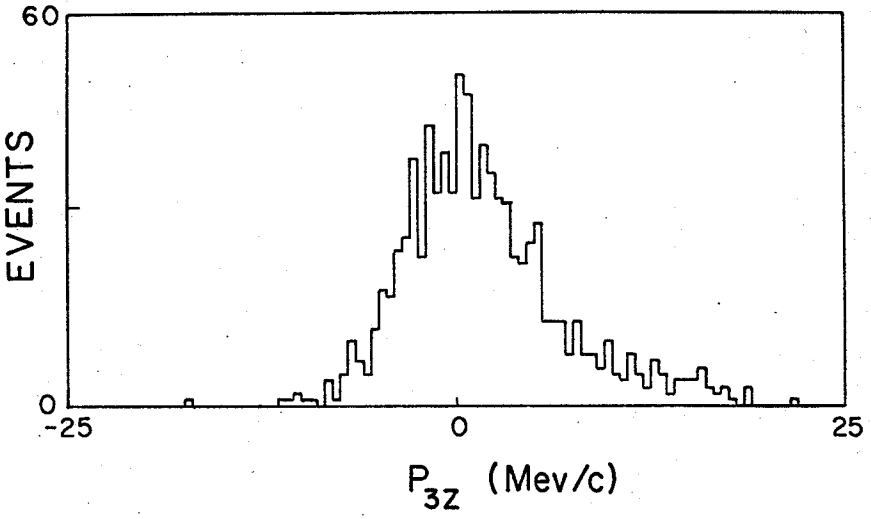

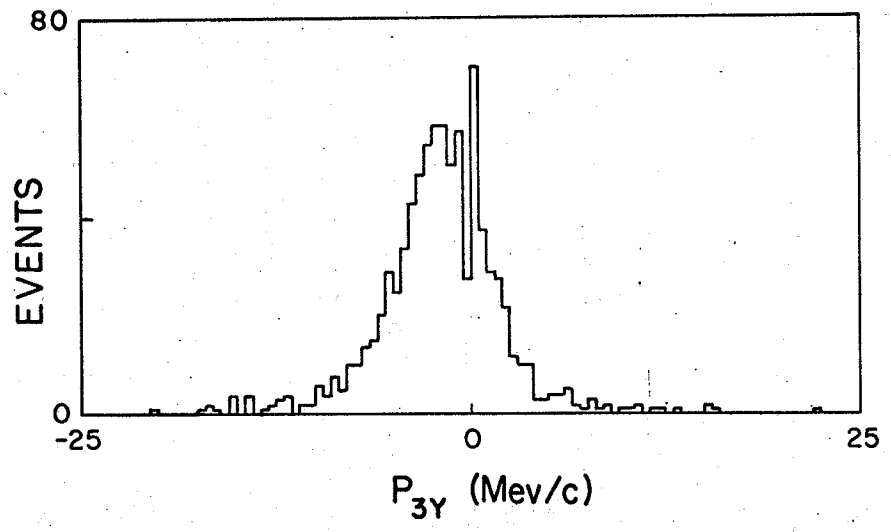

P - P ELASTIC SCATTERING

MOMENTUM RESOLUTION OF "THIRD"

FINAL STATE PARTICLE AT

E_0 = 46 Mev.

CHAPTER V

RESULTS OF A TEST RUN.

In July 1969, during a cyclotron run lasting nine days, some preliminary results were taken on the D(p,2p)N reaction and the PPB process. The main objective was to calibrate the spectrometer, to test data-taking procedures and to collect a statistically meaningful sample of events. These events were needed for testing hardware performance and the procedures for data analysis, leading to further improvements in computer programs. No attempt was made to optimise all parameters as would be necessary before starting long data-taking runs.

5.1 Data from the D(p,2p)N reaction.

The probability of (p,2p) events occurring is usually small and the expression of the cross section as a four or five times differential is often severely limited by statistical considerations. As integration over some kinematic variables is usually necessary, it is desirable that the distribution of events should be expressed as a function of those variables where the scattering matrix shows a strong dependence.

As each event is characterised by 60 variables written on magnetic tape, including all the laboratory and centre

of mass kinematic variables, correlations and selections can be made in a way which is uncommon in nuclear physics experiments. The flexibility that this allows is illustrated by observation of the break-up of the deuteron into the available phase space. The deuteron is so loosely bound that this reaction provides a ready source of (p,2p) events.

The yield of events, Y_T , can be expressed in the form

$$Y_T = n\,t\,p\,\varepsilon_v \iiint \varepsilon_g(\theta_1, \theta_2, E_1, \phi_1, \phi_2) \frac{d^3\sigma}{d\Omega_1 d\Omega_2 dE_1} d\Omega_1 d\Omega_2 dE_1 \quad \ldots\ldots(1)$$

where

n = number of target atoms/cc.

t = length of the target.

p = number of incident protons which have traversed the target.

ε_v = spectrometer detection efficiency as defined in subsection 4.1(c).

ε_g = geometric efficiency.

Expanding,

$$Y_T = n\,t\,p\,\varepsilon_v \iiiint \varepsilon_g(\theta_1, \theta_2, E_1, \phi_1, \phi_2) \frac{d^5\sigma}{d(\cos\theta_1)\, d(\cos\theta_2)\, d\phi_1\, d\phi_2\, dE_1} d(\cos\theta_1)\, d(\cos\theta_2) \times d\phi_1\, d\phi_2\, dE_1 \quad \ldots\ldots(2)$$

ε_g is a complicated function which would be almost impossible to derive analytically for our geometry. In Fig.II.5, for example, the geometric efficiency for a gas

target, determined by graphical methods, was presented as a function of θ and ϕ . The geometric variables are interdependent giving rise to curves of similar functional complexity. This problem can be approached using the Monte Carlo method to generate events within the available phase space. Alternatively, (and the method we shall use later) the space can be carved up into bins where all variables are independent and the efficiency is constant. For these special cases we shall assume (and continue to do so unless stated otherwise) that $\varepsilon_g = 1$. Then for a certain small range in θ , ϕ and E_1 we have a yield, Y , and the cross section is given by

$$\frac{d^3\sigma}{d\Omega_1\, d\Omega_2\, dE_1} = \frac{Y}{n\,t\,p\;\varepsilon_v\;\Delta\phi_1\;\Delta\phi_2\;\Delta\theta_1\;\Delta\theta_2\;\sin\theta_1\;\sin\theta_2\;\Delta E_1} \qquad \ldots\ldots\ldots(3)$$

A 0.007" thick CD_2 target was placed in the centre of the scattering chamber filled with H_2 gas and an incident proton beam of 10^{-11} amps produced a trigger rate of 20-25/sec. A total charge of 8.0 nC produced 39,677 raw events of which 464 were initiated by triggers from the random electronics. From this total 23,994 fell within the allowed range for the vertex errors of $\pm$ 1" in both beam and vertical directions.

Fig.V.1 shows the variation of $\frac{d^3\sigma}{d\Omega_1\, d\Omega_2\, dE_1}$ with E_1 at symmetric angles of 30° and 34°. As expected, kinematically the energy of the corresponding neutron decreases with increasing opening angle, $(\theta_1 + \theta_2)$, hence

the neutron is becoming more of a spectator in the reaction. The cross section is higher at the larger opening angle. To investigate the spectator property further, suppose we take all of the events and integrate over the energies constraining so that only events are accepted within the narrow range $\Delta\phi_1$ and $\Delta\phi_2$. Then

$$Y = n\,t\,\rho\,\varepsilon_v\,\Delta\phi_1\,\Delta\phi_2 \iint \frac{d^2\sigma}{d(\cos\theta_1)\,d(\cos\theta_2)}\, d(\cos\theta_1)\,d(\cos\theta_2) \quad \ldots\ldots (4)$$

It is usually desirable to present experimental results as the distribution of events and with conventional counter telescopes cross sections are usually expressed in the above form with the solid angles already folded in. However, here the cross section can be expressed in terms of the opening angle, θ_s, and the asymmetric angle, $\theta_D\,(=(\theta_1-\theta_2))$. Equation (4) then must be transformed in order to express the cross section and the volume element in terms of the new coordinate system. The yield of events is now given by

$$Y = n\,t\,\rho\,\varepsilon_v\,\Delta\phi_1\,\Delta\phi_2 \iint \frac{d^2\sigma}{d\theta_s\,d\theta_D} \times \frac{\partial(\theta_s,\theta_D)}{\partial(\cos\theta_1,\cos\theta_2)} \times \frac{\partial(\theta_1,\theta_2)}{\partial(\theta_s\,\theta_D)} \times \sin\theta_1 \sin\theta_2\, d\theta_s\, d\theta_D$$

where the Jacobians are

$$\frac{\partial(\theta_s,\theta_D)}{\partial(\cos\theta_1,\cos\theta_2)} = \begin{vmatrix} \frac{\partial\theta_s}{\partial(\cos\theta_1)} & \frac{\partial\theta_D}{\partial(\cos\theta_1)} \\ \frac{\partial\theta_s}{\partial(\cos\theta_2)} & \frac{\partial\theta_D}{\partial(\cos\theta_2)} \end{vmatrix} = \begin{vmatrix} -\frac{1}{\sin\theta_1} & -\frac{1}{\sin\theta_1} \\ -\frac{1}{\sin\theta_2} & \frac{1}{\sin\theta_2} \end{vmatrix} = -\frac{2}{\sin\theta_1 \sin\theta_2}$$

and

$$\frac{\partial(\theta_1,\theta_2)}{\partial(\theta_s,\theta_D)} = \begin{vmatrix} \frac{\partial\theta_1}{\partial\theta_s} & \frac{\partial\theta_2}{\partial\theta_s} \\ \frac{\partial\theta_1}{\partial\theta_D} & \frac{\partial\theta_2}{\partial\theta_D} \end{vmatrix} = \begin{vmatrix} \frac{1}{2} & \frac{1}{2} \\ \frac{1}{2} & -\frac{1}{2} \end{vmatrix} = -\frac{1}{2}$$

Figure V.1

Relative differential cross sections for the D(p,2p)N reaction as a function of the proton and neutron energies. The cross section increases with opening angle while at the same time the peaks in the neutron cross sections shift to lower energies.

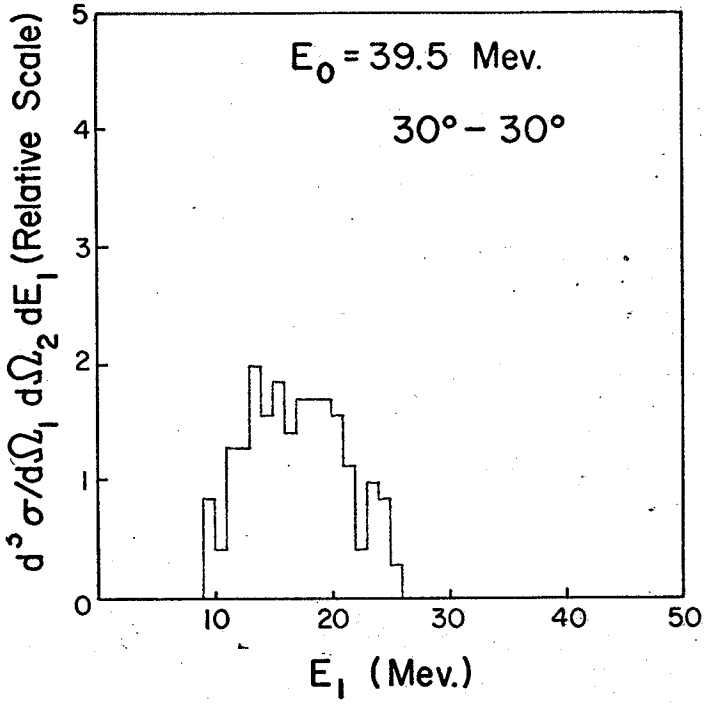
$E_0 = 39.5$ Mev.
30° – 30°
$d^3\sigma/d\Omega_1\, d\Omega_2\, dE_1$ (Relative Scale)
E_1 (Mev.)

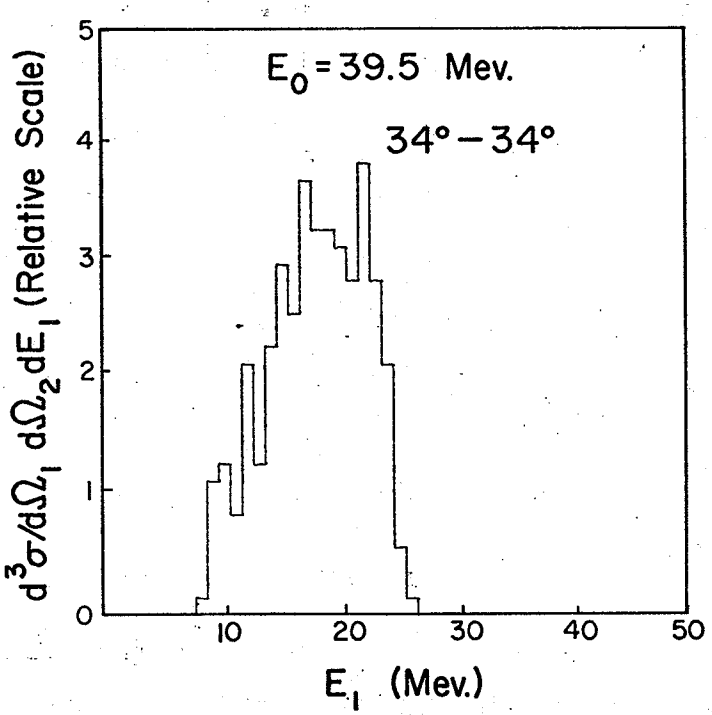
$E_0 = 39.5$ Mev.
34° – 34°
$d^3\sigma/d\Omega_1\, d\Omega_2\, dE_1$ (Relative Scale)
E_1 (Mev.)

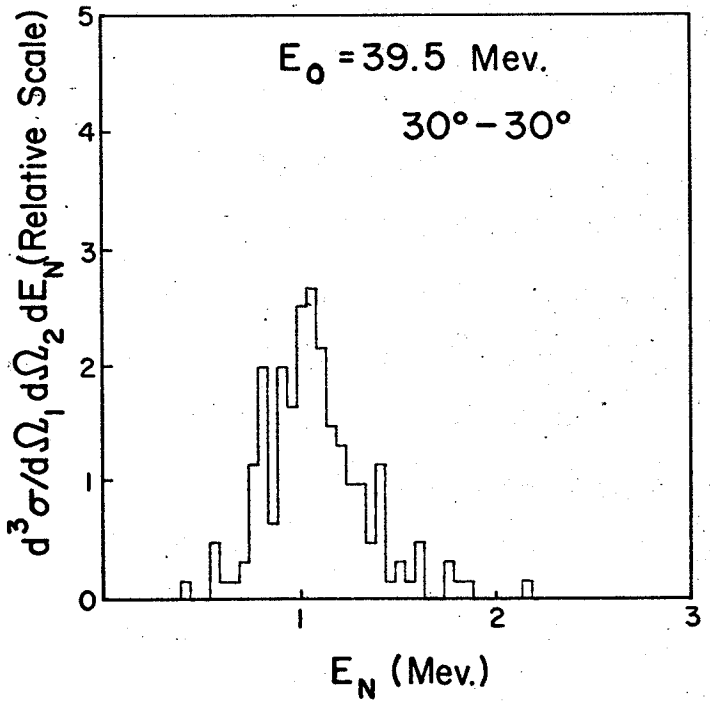
$E_0 = 39.5$ Mev.
30° – 30°
$d^3\sigma/d\Omega_1\, d\Omega_2\, dE_N$ (Relative Scale)
E_N (Mev.)

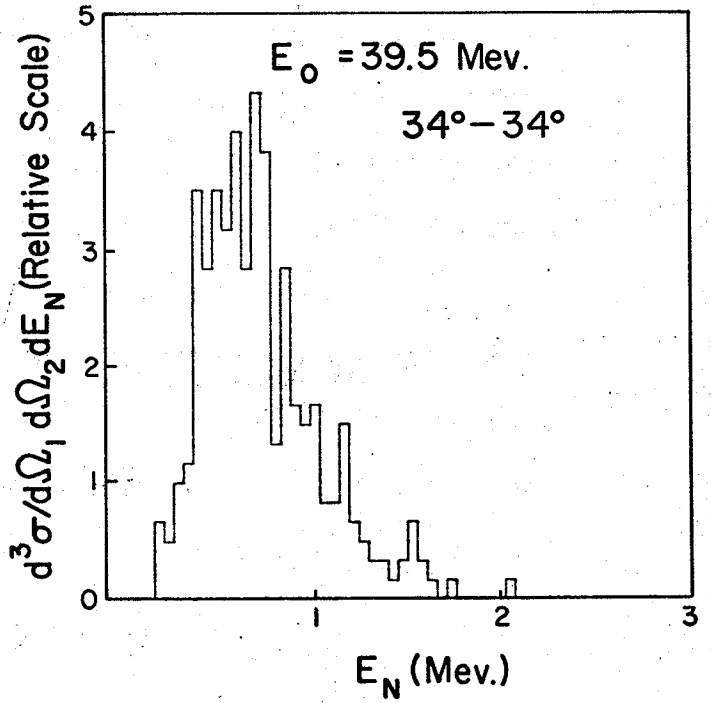
$E_0 = 39.5$ Mev.
34° – 34°
$d^3\sigma/d\Omega_1\, d\Omega_2\, dE_N$ (Relative Scale)
E_N (Mev.)

substitution gives

$$Y = n\,t\,\rho\,\varepsilon_v\,\Delta\phi_1\,\Delta\phi_2 \iint \frac{d^2\sigma}{d\theta_s\,d\theta_D}\,d\theta_s\,d\theta_D$$

Fig.V.2 shows a scatter plot of events in the $\theta_s - \theta_D$ plane. There is obviously a strong dependence of opening angle on asymmetric angle and in order to make $\varepsilon_g(\theta_s, \theta_D)$ (see page 147-148)equal unity we take a horizontal cut in the range $\Delta\theta_D$ and project onto the θ_s axis. The cross section obtained can then be expressed by

$$\frac{d^2\sigma}{d\theta_s\,d\theta_D} = \frac{Y}{n\,t\,\rho\,\varepsilon_v\,\Delta\phi_1\,\Delta\phi_2\,\Delta\theta_D\,\Delta\theta_s}$$

The dependence of the cross section on opening angle given in Fig.V.2 shows an increase in the kinematic region corresponding to the emission of two protons with high relative energy and a low energy neutron in the laboratory, implying a quasi-free scattering process. Similarly, the constraint in, θ_D, can be removed and imposed on θ_s. Fig.V.2(c) shows the distribution of events when the opening angle is kept constant and only asymmetric events are accepted. The distribution must be symmetrical about zero. It does not have any characteristic features.

The (p,2p) events collected can also be expressed in a form which leads to the dependence of the cross sections on the angle of non-coplanarity $\bar{\phi}$. Changing the coordinate system from variables $(\cos\theta_1, \cos\theta_2, \phi_1, \phi_2)$ to $(\theta_1, \theta_2, \phi_1, \bar{\phi})$ gives

$$Y_T = n\,t\,\rho\,\varepsilon_v \iiiint \varepsilon_g(\theta_1,\theta_2,\phi_1,\bar{\phi}) \frac{d^4\sigma}{d\theta_1\,d\theta_2\,d\phi_1\,d\bar{\phi}} \left(\frac{\partial(\theta_1,\theta_2,\phi_1,\bar{\phi})}{\partial(\cos\theta_1,\cos\theta_2,\phi_1,\phi_2)}\right) \sin\theta_1 \sin\theta_2 \times d\theta_1\,d\theta_2\,d\phi_1\,d\bar{\phi}$$

Solving the 4 x 4 determinant for the Jacobian leads to

$$Y_T = n\,t\,\rho\,\varepsilon_v \iiiint \frac{\varepsilon_g(\theta_1,\theta_2,\phi_1,\bar{\phi})\; d^4\sigma}{d\theta_1\,d\theta_2\,d\phi_1\,d\bar{\phi}} \; d\theta_1\,d\theta_2\,d\phi_1\,d\bar{\phi}$$

If events are selected within a small range $\Delta\theta_1$ and $\Delta\theta_2$ then

$$Y = n\,t\,\rho\,\varepsilon_v\,\Delta\theta_1\,\Delta\theta_2 \iint \frac{\varepsilon_g(\phi_1,\bar{\phi})\; d^4\sigma}{d\theta_1\,d\theta_2\,d\phi_1\,d\bar{\phi}} \; d\phi_1\,d\bar{\phi}$$

Fig.V.3(a) gives a scatter plot of a sample of events in the ϕ_1-$\bar{\phi}$ plane. To express the cross section as a four times differential one could use the same method as that employed with the variation of cross sections with opening angle in Fig.V.2. However, as the beam is unpolarised the distribution in ϕ_1 is uniform and such a procedure is wasteful. The two variables ϕ_1 and $\bar{\phi}$ are strongly inter-dependent but if the space is carved up into sections where the independence of ϕ_1 and $\bar{\phi}$ is approximated the integration over ϕ_1 can be performed by counting the number of events in each bin.

The integrated cross section evaluated at an angle $\bar{\phi}$ is then given by

$$\frac{d^3\sigma}{d\theta_1\,d\theta_2\,d\bar{\phi}} = \frac{Y}{n\,t\,\rho\,\varepsilon_v\,\Delta\theta_1\,\Delta\theta_2\,\Delta\phi\;\;\varepsilon_g(\bar{\phi})}$$

where $\varepsilon_g(\bar{\phi})$ is the geometric efficiency for each bin. In the simple case where constraints of $\pm\,\phi_L$ are imposed on ϕ_1

Figure V.2

The distribution of events from D(p,2p)N reaction with opening angle and asymmetric angle. The scatter plot in the top right shows a higher concentration of events at larger opening angle. Vertical and horizontal cuts are made to provide the projections giving the variation of the cross section with opening angle at the bottom right and the variation with asymmetric angle at the top left.

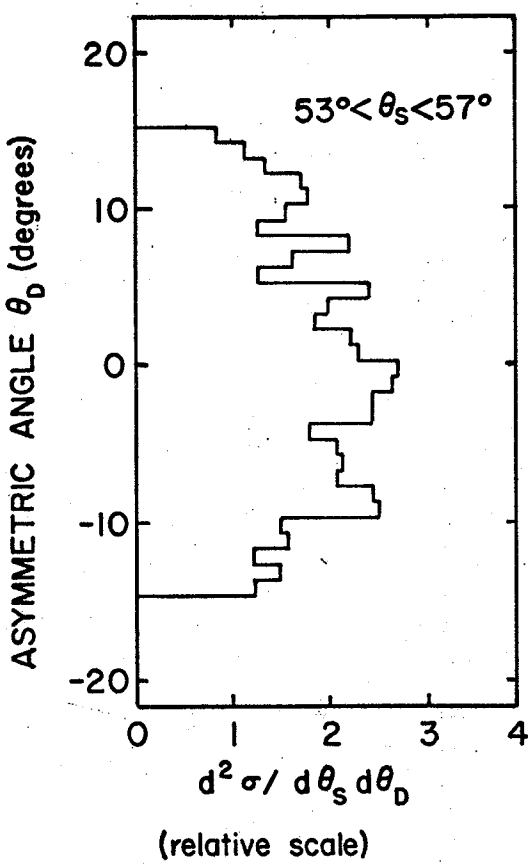

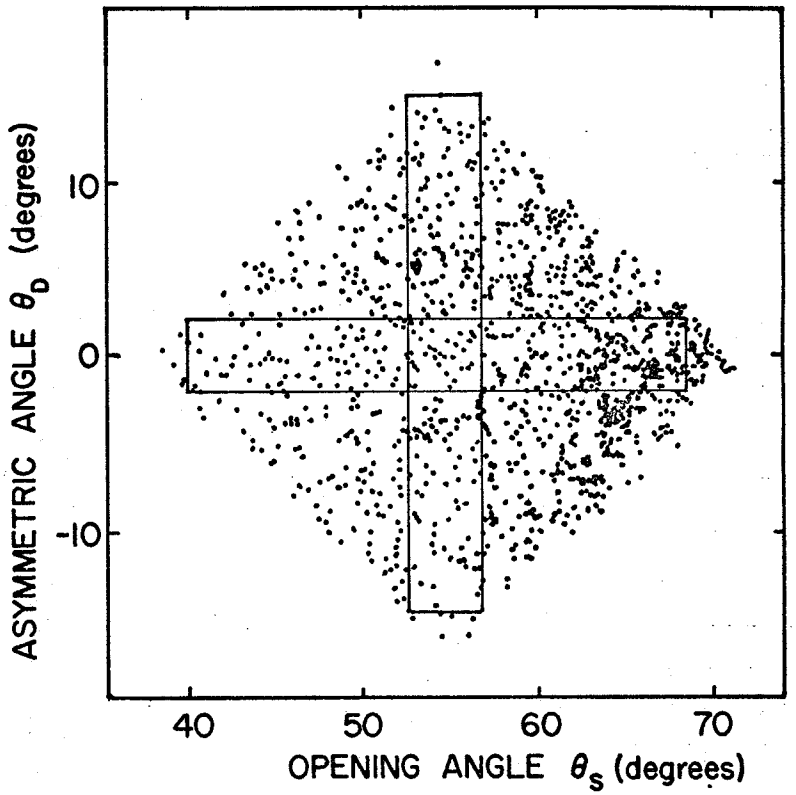

D(p,2p)N

$E_0 = 39.5$ MeV

$0 < |\bar{\Phi}| < 5°$

$19° < \theta < 36°$

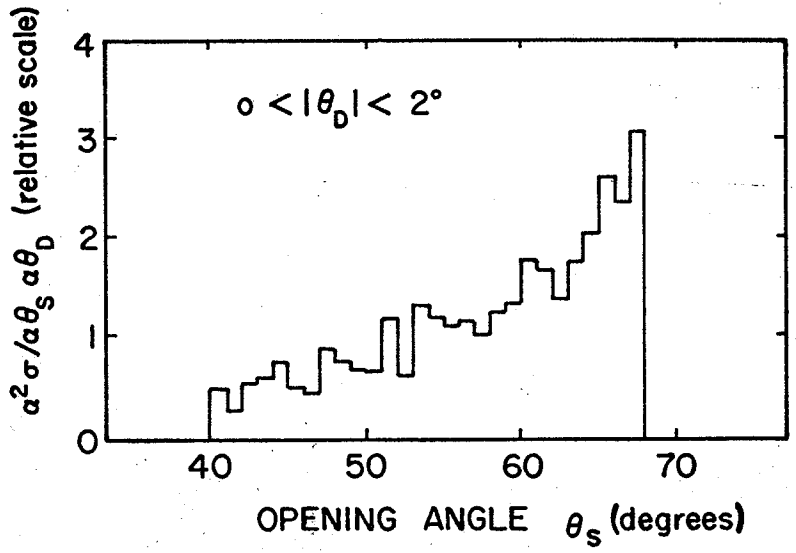

Figure V.3

The non-coplanar cross section for the D(p,2p)N reaction.

(a) shows a scatter plot of ϕ v $\bar{\phi}$ for events in the range $\theta_1 = \theta_2 = 34^\circ \pm 2^\circ$, $-16^\circ < \phi_1 < 16^\circ$ and $164^\circ < \phi_2 < 196^\circ$

(b) the space is divided into 5° bins in the absolute value of the non-coplanar angle $\bar{\phi}$ and integral number of events in each bin is normalised to give the dependence of the cross section on $\bar{\phi}$

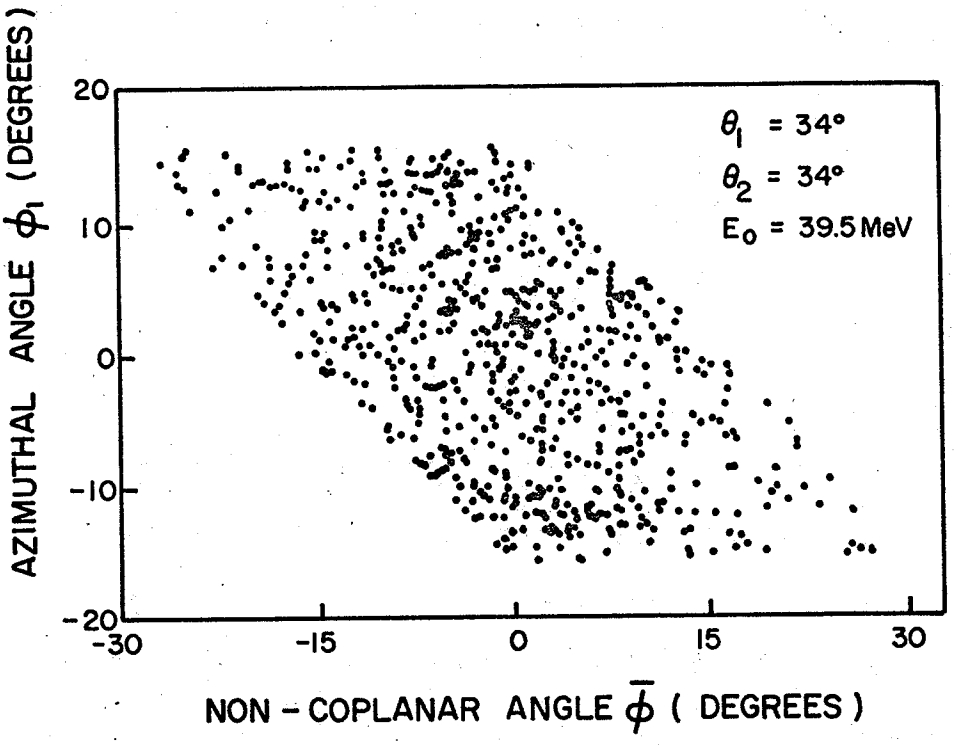
AZIMUTHAL ANGLE ϕ_1 (DEGREES)
20
10
0
-10
-20
-30
-15
0
15
30
θ_1 = 34°
θ_2 = 34°
E_0 = 39.5 MeV
NON - COPLANAR ANGLE $\bar{\phi}$ (DEGREES)

(a)

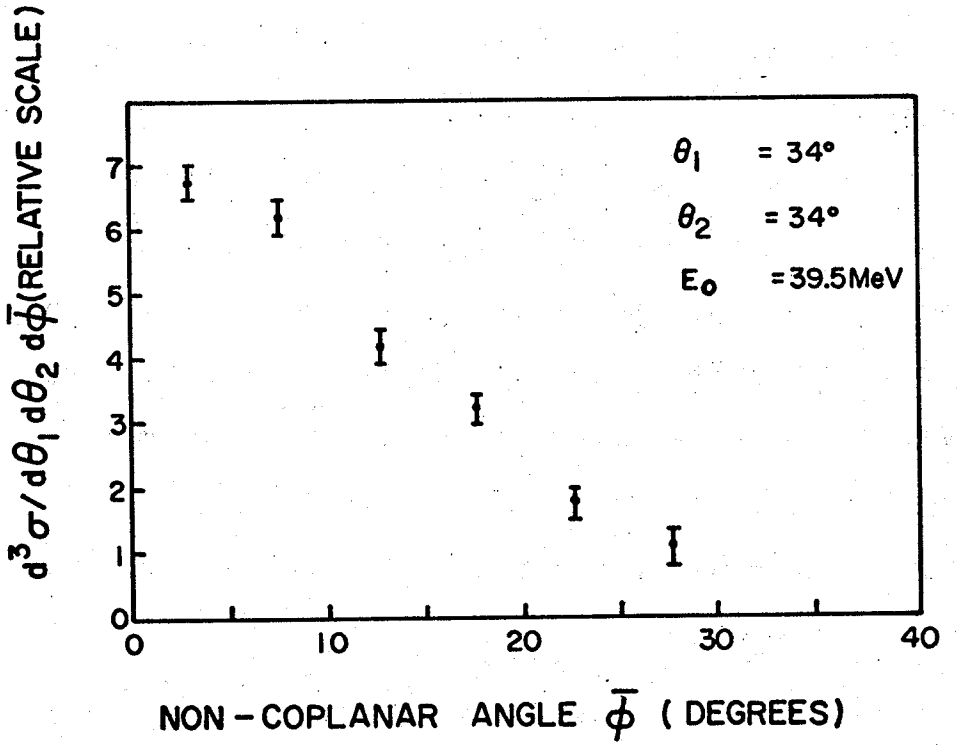
$d^3\sigma/d\theta_1 d\theta_2 d\bar{\phi}$(RELATIVE SCALE)
7
6
5
4
3
2
1
0
0
10
20
30
40
θ_1 = 34°
θ_2 = 34°
E_0 = 39.5MeV
NON - COPLANAR ANGLE $\bar{\phi}$ (DEGREES)

(b)

and ϕ_2 then $\quad \epsilon_g(\bar{\phi}) = 1 - \bar{\phi}/\phi_L$

Fig.V.3(a) shows that the density of events decreases strongly as the angle of non-coplanarity increases and Fig.V.3(b) shows the variation of the integrated cross section with $\bar{\phi}$. This strong dependence is consistent with the predictions of the spectator model[27] and the experimental results of Slaus et al. at 46 MeV[28].

5.2 Data from the PPB process.

Data was taken at an incident proton energy of 39.5 MeV with the wire chambers in the PPB position, hydrogen gas as a target and without the delta ray filter in position. Using STAR, i.e. recording all raw data on tape, four files were written, two of which had a total of 38,413 triggers taken at 1.0 nA, one with 29,007 triggers taken at 1.5 nA and one with 40,040 triggers taken at 2.0 nA, giving a total of 107,460 raw events. The total charge was about 8.6 nA-hrs reducing to a net charge of 7.7 nA-hrs after correction for dead time. The PDP-9, with a "coarse" vertex of $\pm$ 2" in the beam direction and $\pm$ 1" in the vertical direction, accepted 11,199 of these events which were subsequently processed in the kinematics program.

Fig.V.4 shows an E_1-E_2 scatter plot of a sample of the events when a tight vertex of $\pm$ 0.3" and $\pm$ 0.8" is respectively imposed in the vertical and beam directions. The density of points along the diagonal comes from D(p,2p)N

events (as deuterium is present as an impurity of 0.015% in H_2 gas) and the lower left corner contains PPB events with background. Events in the top right corner come from random elastic coincidences.

The energy surface can be divided into regions using the constraining variable E_1+E_2, hence the PPB region can be investigated quite independently. Figs.V.5(a) and (b) show the distribution in chi square for the PPB region for events which lie within the tight vertex limit and for events which lie outside the tight vertex limit respectively. If only events having chi square less than 5 are accepted inside the PPB energy boundary, then good PPB events must have small vertex errors in the beam symmetry plane. Fig.V.6 shows a scatter plot of events satisfying these criteria and the density of points around the centre indicate that PPB events are present. Out of a total of 335 events satisfying the coarse vertex presented in Fig.V.6, 297 of these events are concentrated within the tight vertex region. When the constraint defining the energy region is removed an additional 8 events are added and these lie close to the E_1+E_2 boundary.

The chi square distribution for events within the D(p,2p)N region are shown in Figs.V.5(c) and(d). In Fig.V.5 (c) all (p,2p) events have been analysed statistically as coming from deuterium break-up and out of 361 events in the diagonal space defined by $-3 < [E_0 - (E_1+E_2)] < 7$ only 8

Figure V.4

E_1-E_2 scatter plot, taken at 39.5 MeV, of a sample of the events which lie inside the tight vertex limits, when hydrogen gas is the target. The density of points along the diagonal comes from D(p,2p)N events (as deuterium is present as an impurity of 0.015% in H_2 gas) and the lower left corner contains p-p bremsstrahlung events with background.

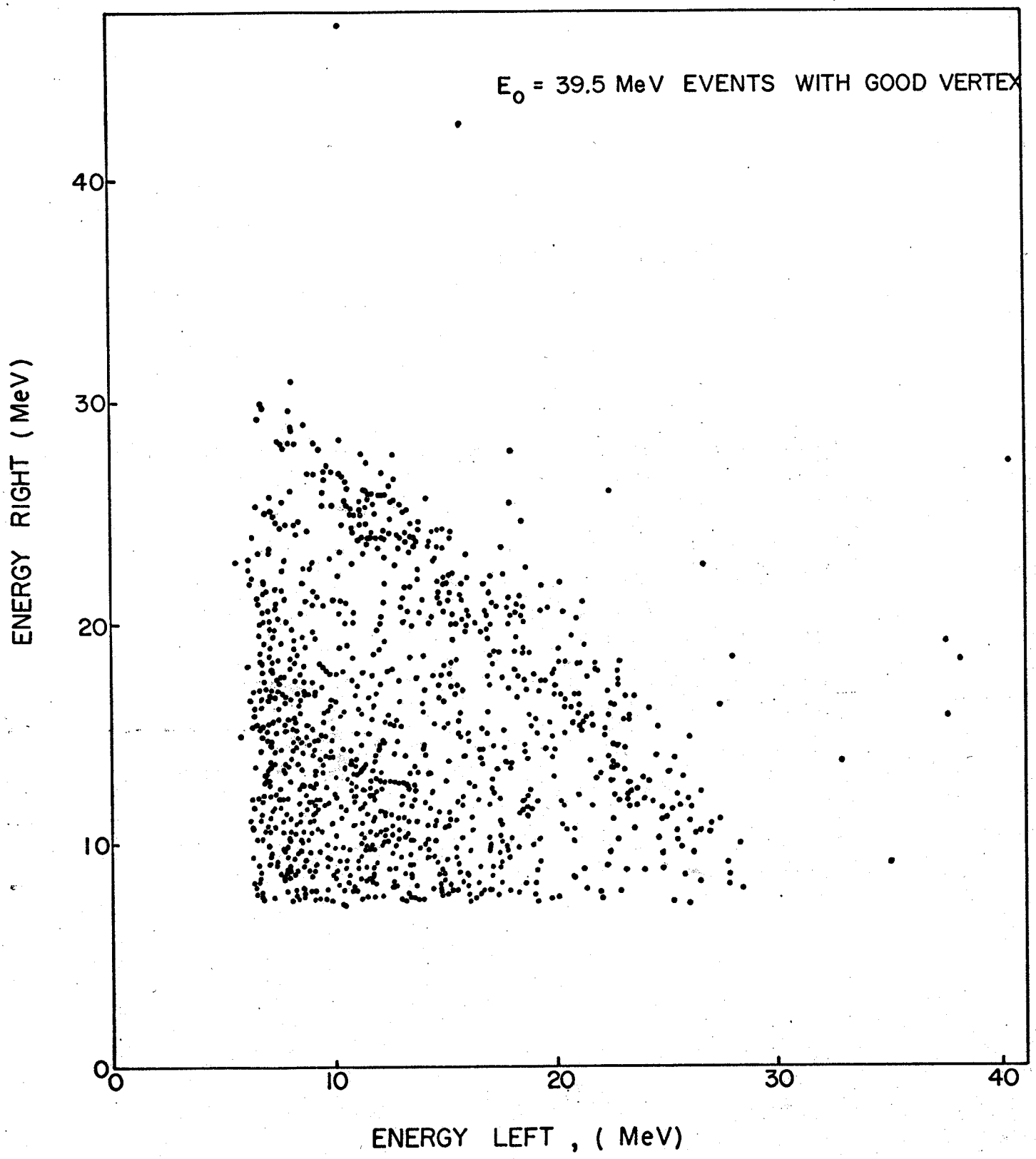
E_0 = 39.5 MeV EVENTS WITH GOOD VERTEX
ENERGY RIGHT (MeV)
ENERGY LEFT , (MeV)
0
10
20
30
40

Figure V.5

Chi square distributions for events selected on the difference in the incident beam energy and the sum of the energies of the outgoing protons.

(a) Chi square distributions for tight vertex events in the range $[E_0 - (E_1 + E_2)] > 7$ MeV.

(b) Chi square distributions for events in the range $[E_0 - (E_1 + E_2)] > 7$MeV but which lie in between tight and coarse vertex limits. They must be multiplied by 0.6 to obtain the equivalent number of background events within the tight vertex limits.

(c) Chi square distribution for events which lie in the energy range $-3 < [E_0 - (E_1 + E_2)] < 7$ MeV processed as deuteron break-up.

(d) Chi square distribution for the same events as (c) but processed as PPB events.

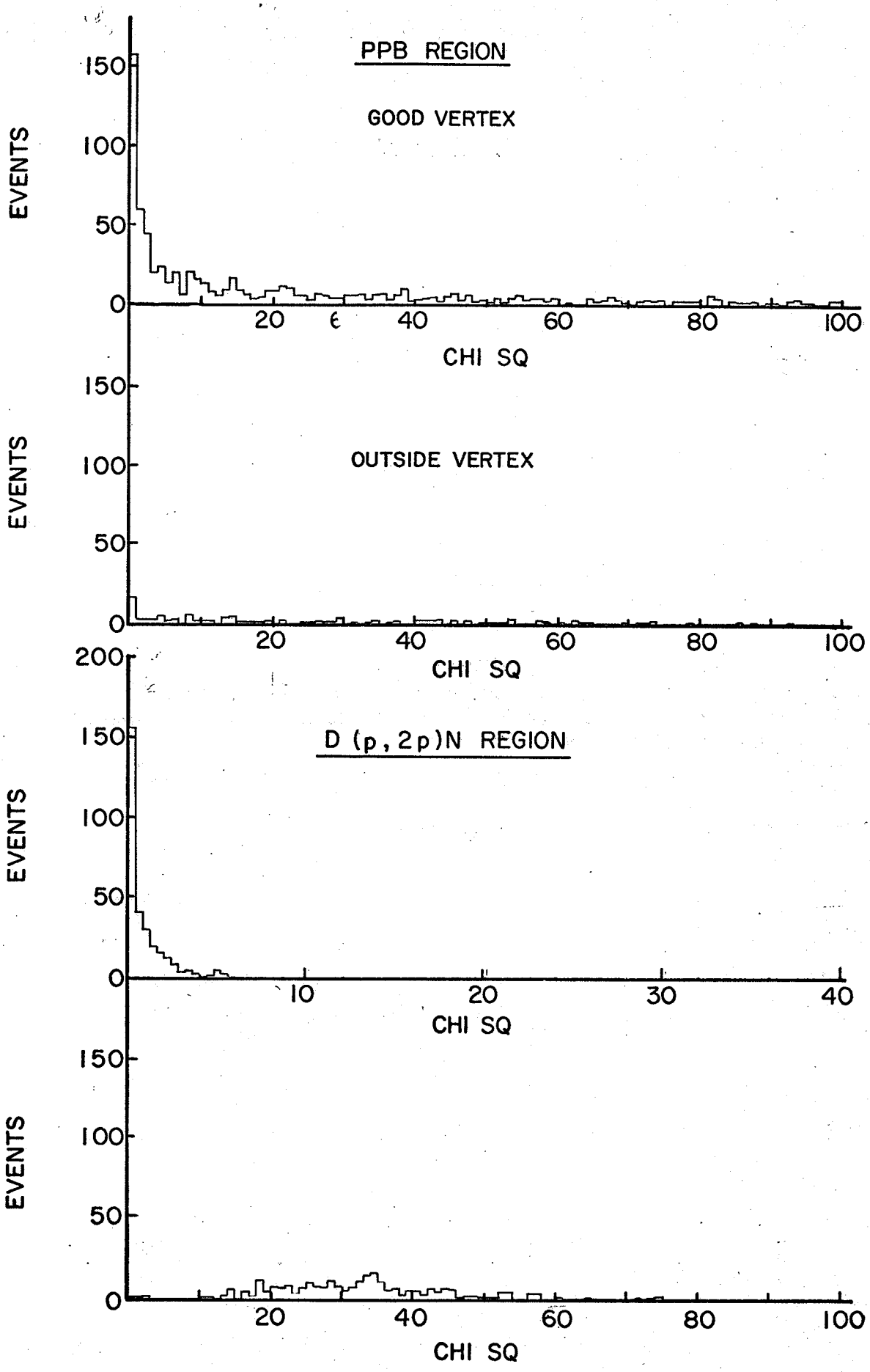
PPB REGION
GOOD VERTEX
EVENTS
150
100
50
0
20
40
60
80
100
CHI SQ
OUTSIDE VERTEX
EVENTS
150
100
50
0
20
40
60
80
100
CHI SQ
D (p, 2p)N REGION
EVENTS
200
150
100
50
0
10
20
30
40
CHI SQ
EVENTS
150
100
50
0
20
40
60
80
100
CHI SQ

Figure V.6

Two dimensional scatter plot of horizontal and vertical vertex errors for the data taken with H_2 gas as the target. The events are selected to have a chi square value less than 5. The concentration of points in the centre is due to PPB events.

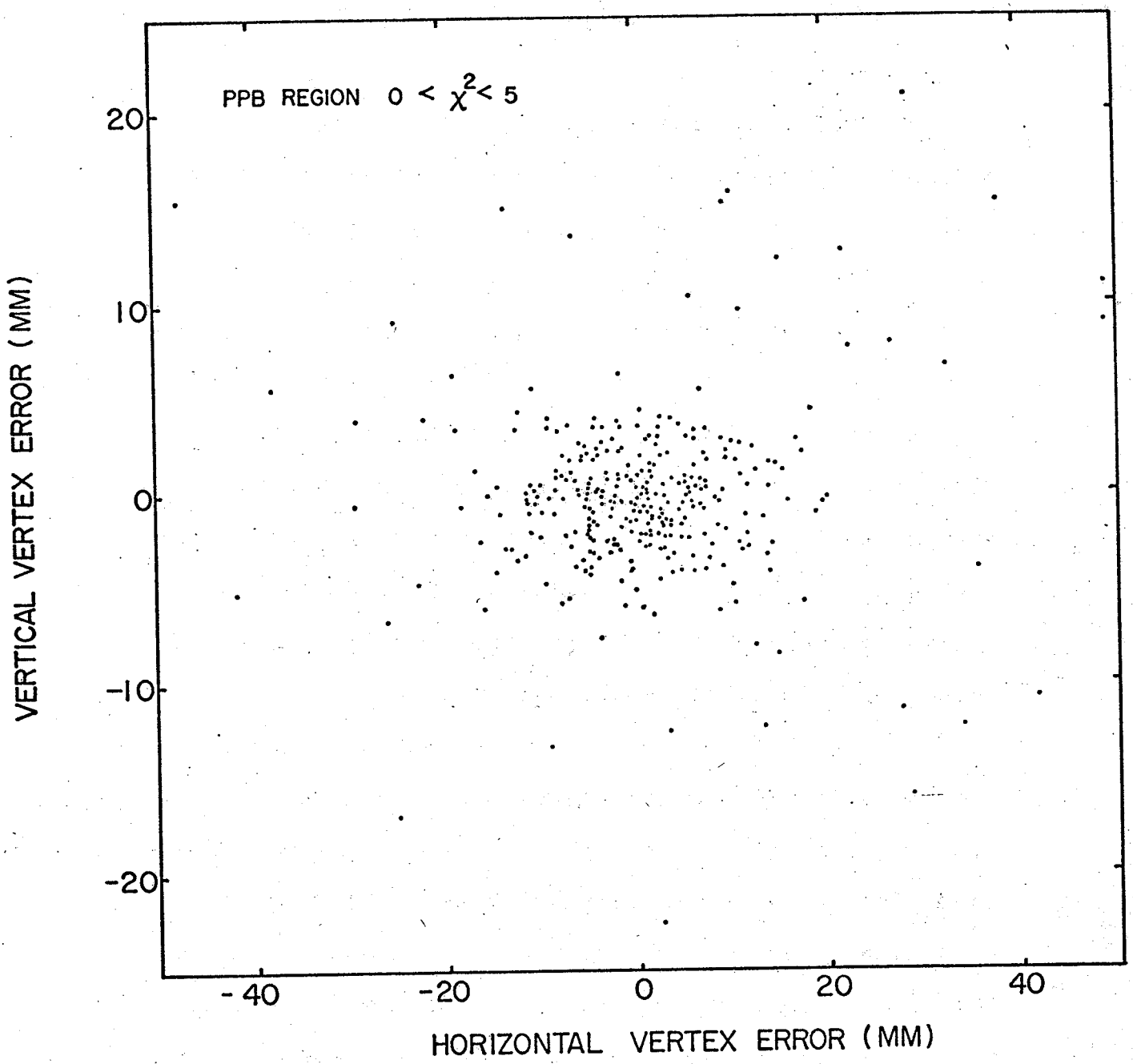
PPB REGION 0 < χ² < 5
20
10
0
-10
-20
-40
-20
0
20
40
VERTICAL VERTEX ERROR (MM)
HORIZONTAL VERTEX ERROR (MM)

events have values of chi square less than 5.

The source of events with chi square in the range 5 to 100 lying within the PPB energy boundary demands further investigation. There can be no doubt that they make a vertex as shown in Fig.V.7. The procedure to establish real events by vertex demand can be tested by investigating the 50 events in the energy range where

$$[E_0 - (E_1 + E_2)] < -3.5 \text{ MeV}$$

These events must originate from accidental coincidences. Fig.V.8 gives the distribution for these random events and it does not show any concentration at the centre. Also an investigation of these bad chi square events within the PPB energy region showed that the tracks originated along the reaction volume, well removed from the collimating slits. It must be concluded therefore, that these are indeed true (p,2p) events.

The E_1-E_2 scatter plot of the contaminants of Fig.V.9 show clearly the D(p,2p)N line. There seems to be another diagonal line nearby but they do not lie on the kinematic loci for air contamination which would be a suspected contaminant. Excited states may be populated which would lead to a higher density at lower energies. The high density of points near the low energy cut-off but not traversing the E_1-E_2 plane along a diagonal are of unknown origin. They are also present in the data presented in reference [29] where their identity was not established either [30].

The E_1-E_2 scatter plot of events with polar angles less than 37°, which lie within the tight vertex error limits and have values of chi square less than 5, is presented in Fig.V.10. The solid line is the boundary imposed by the geometric and energy cut-offs. This defines the energy region where PPB events should populate. The faint curves show a few typical kinematic loci at angles which define the geometric boundary. It is expected that the region will not have uniform density not only because of the variation in cross section but, more particularly, because the geometric efficiency is 100% only near the centre of the region and falls off to zero at the boundary. The boundary is clearly reproduced lending credibility to our conclusion that the events satisfying the vertex and chi square criteria are genuine PPB events.

Figure V.7

Scatter plot of vertex errors for events with energies $E_o - (E_1 + E_2) > 7$MeV and with a value of chi square between 5 and 100. The concentration at the centre is due to genuine (p,2p) events from a contaminant.

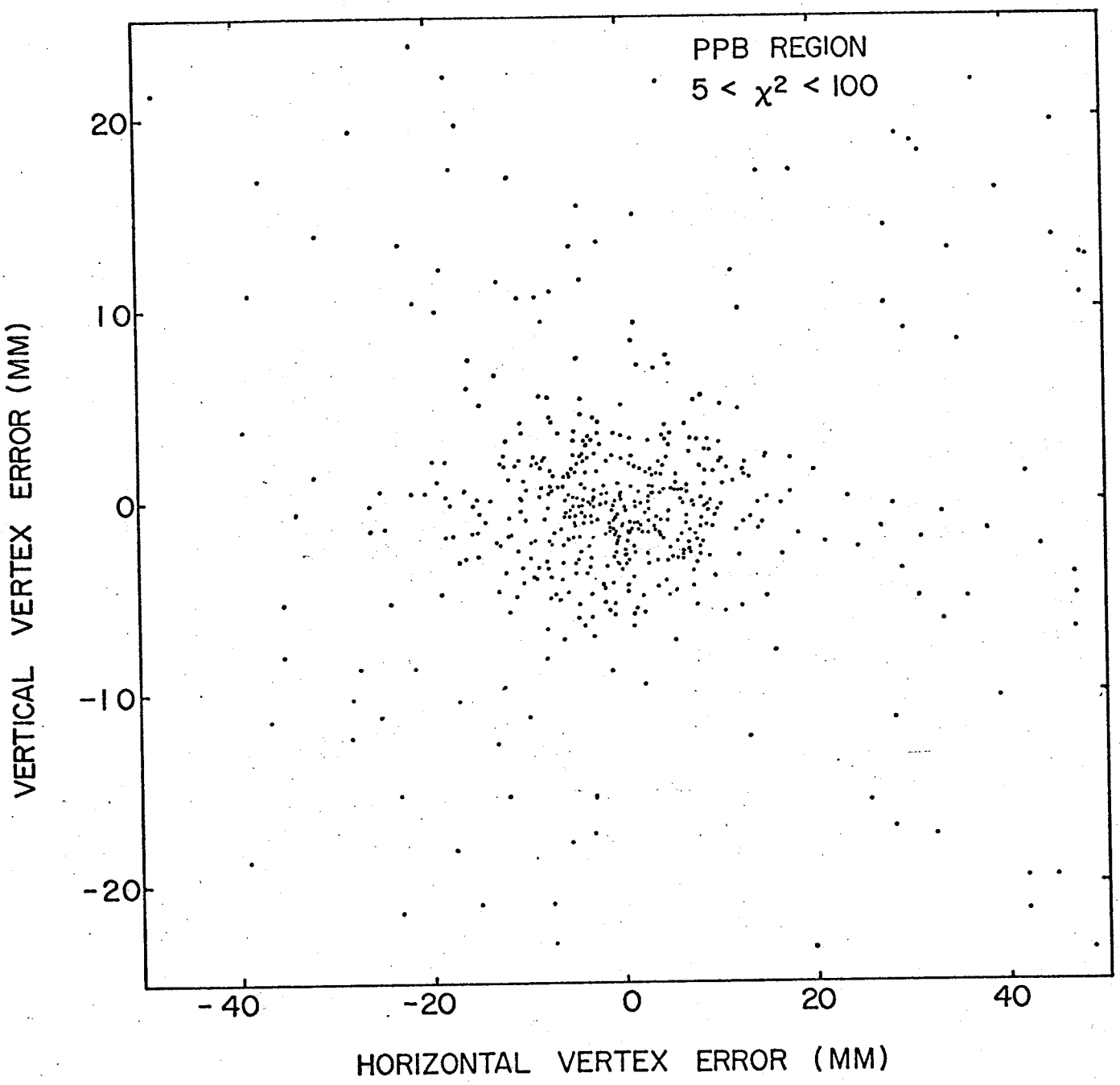
PPB REGION
5 < χ² < 100
20
10
0
-10
-20
-40
-20
0
20
40
VERTICAL VERTEX ERROR (MM)
HORIZONTAL VERTEX ERROR (MM)

Figure V.8

Scatter plot of vertex errors for events with energies $E_1 + E_2 > E_0 + 3.5$ MeV. These events must be due to random coincidences. The space lacks any concentration of points at the centre.

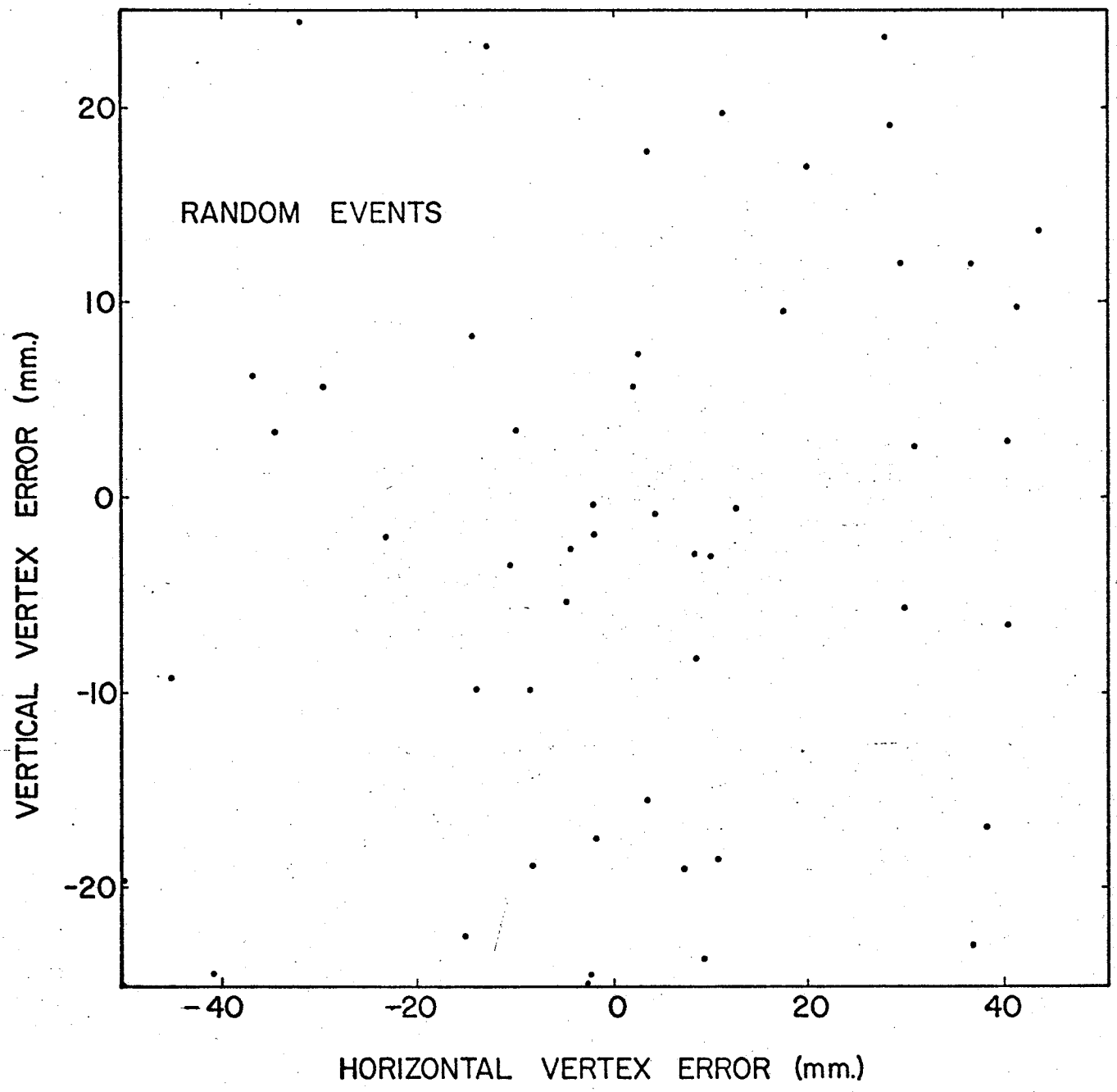
RANDOM EVENTS
VERTICAL VERTEX ERROR (mm.)
HORIZONTAL VERTEX ERROR (mm.)
20
10
0
-10
-20
-40
-20
0
20
40

Figure V.9

E_1-E_2 scatter plot of good vertex events with values of chi square between 5 and 100. The D(p,2p)N events can be easily identified. The identity of the concentration of events along a diagonal line close to the deuterium locus and near the energy cut-off boundaries has not been established.

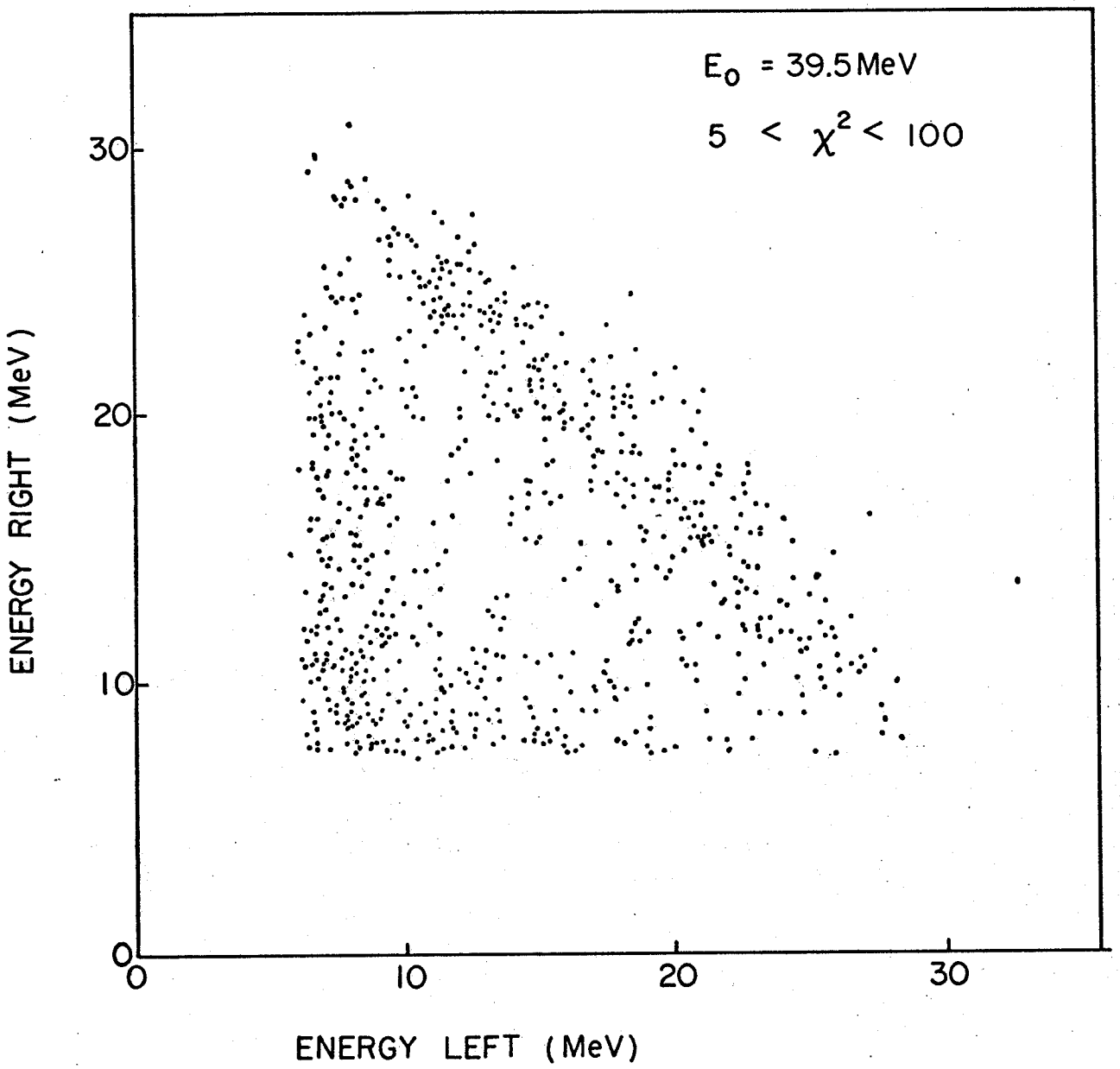
E_0 = 39.5 MeV
5 < χ^2 < 100
ENERGY RIGHT (MeV)
ENERGY LEFT (MeV)
0
10
20
30

Figure V.10

Effect of geometric efficiency and energy cut-off on the distribution of PPB events.
The heavy line gives the boundary imposed by :-

(a) the acceptance of events with polar scattering angles θ less than 37° and greater than 16°.

(b) the minimum scattered energy detectable by the scintillation counters.

The faint lines show some typical kinematic loci which define the geometric boundary.

The full dots are events which satisfy the vertex and chi square requirements necessary to qualify as PPB events.

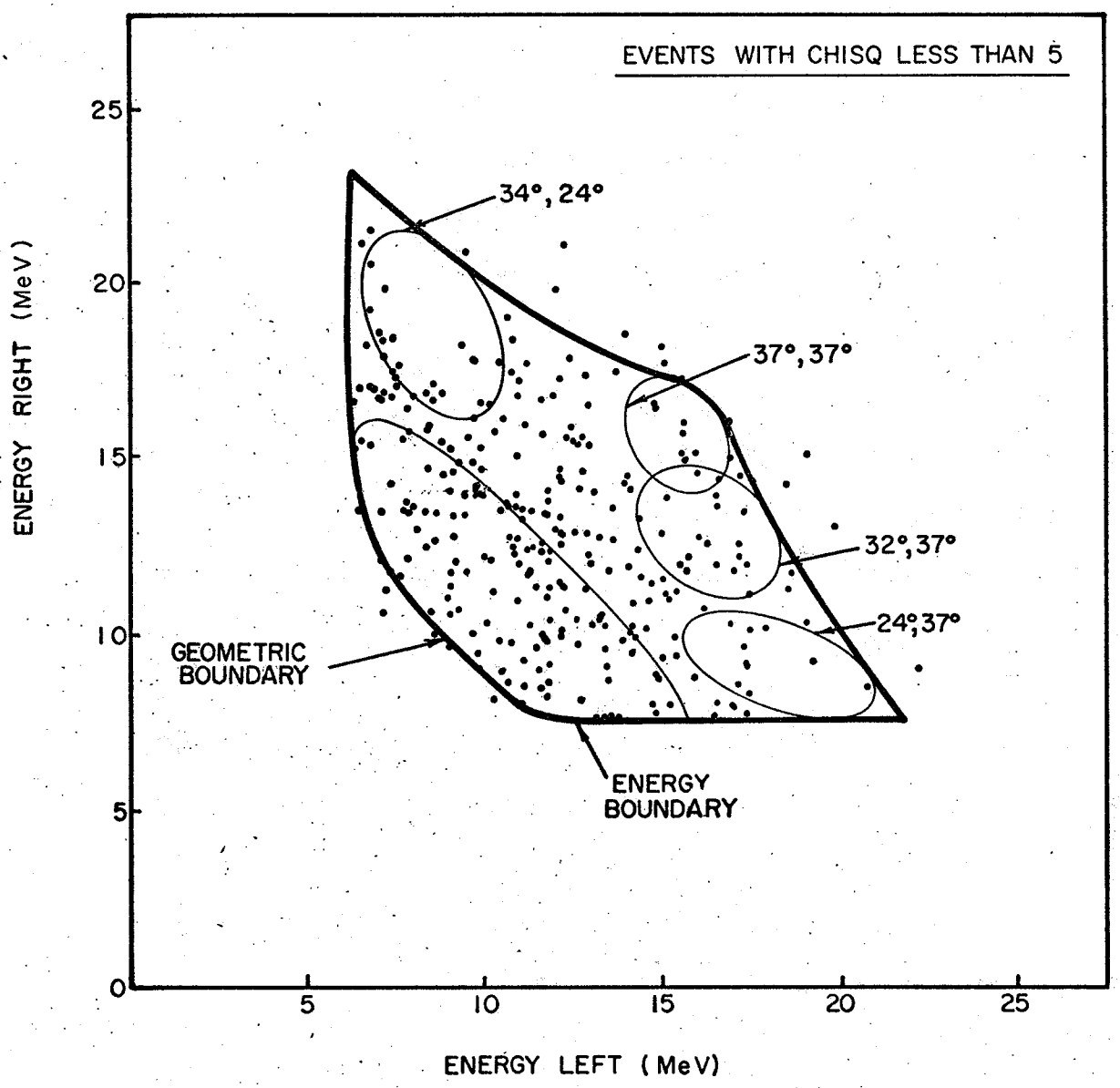
EVENTS WITH CHISQ LESS THAN 5
34°, 24°
37°, 37°
32°, 37°
24°, 37°
GEOMETRIC BOUNDARY
ENERGY BOUNDARY
ENERGY RIGHT (MeV)
ENERGY LEFT (MeV)
0
5
10
15
20
25

CONCLUSIONS.

We have constructed a spectrometer designed to study (p,2p) reactions in general and the PPB process in particular. The motivation for use of wire chambers was to provide large solid angles and at the same time to maintain good angular resolution. This eliminates the necessity for compromise between angular resolution and event rates.

The geometry chosen for the results presented in Chapters IV and V gives a solid angle of 0.16 sterad. to the centre of the reaction volume. The angular range of events extends from 16° to 42° in the polar scattering angle, θ , and from -28° to 28° in azimuthal scattering angle, ϕ . The angular resolution was limited by multiple scattering and was measured to be 0.32° HWHM at 21 MeV with the delta ray filter removed. The energy resolution of the large scintillation counters is 3.1% HWHM at 42 MeV. For a pair of 21.0 MeV outgoing protons the energy resolution of the undetected third particle is 1.5 MeV HWHM. For a pair of 23 MeV outgoing protons the momentum resolution of the third particle is 3.5 MeV/c.

Background rejection is accomplished by two methods not previously used in (p,2p) experiments :-

(a) Vertex Demand.

The effectiveness of this requirement is dependent on the reaction undergoing investigation and the

particular geometry in use. The spacing between the wires makes a greater contribution than multiple scattering with the given geometry. The area of vertex uncertainty at two standard deviations is 0.35 cm^2 in the downstream position for polar scattering angles of 42^o. Upstream and at polar angles of 21^o the area of uncertainty was measured to be 1.16 cm^2. It is expected that more than 95% of the random background can be rejected for the PPB reaction using this criterion.

(b) Goodness of Fit.

The energy resolution tends to dominate the precision with which an event can be specified kinematically. Nevertheless, chi square can be defined so that almost complete segregation between events from deuterium break-up and PPB is possible. Lying within the kinematic limits where PPB events are expected to populate, the use of chi square made possible the separation of events, all of which made a good vertex. Events with chi square less than 5 were accepted as PPB events and these formed a pattern on an E_1-E_2 plot consistent with the boundaries imposed by the geometric and energy cut-offs.

The spectrometer can also be used with a solid target and some relative cross sections are presented for the D(p,2p)N reaction. The purpose here was mainly to apply the spectrometer to a three body final state re-

action which has been previously investigated. The enhancement of the cross section at large opening angle corresponding to quasi-free scattering was observed. So also was the rapid decrease in cross section with the angle of non-coplanarity, $\bar{\phi}$.

A test run revealed the desirability of having continuous control of some important drifts that can occur over extended data-taking periods. It was found that the overhead required to check energy calibrations, wire chamber efficiencies and beam tuning conditions was severe. As a consequence the rear wire chambers have now been repositioned so that a small sample of protons scattered elastically from part of the reaction volume trigger the chambers. Besides monitoring drifts, cross sections can be normalised to the accurately known elastic cross sections.

Unfiltered delta rays, produced in hydrogen gas by the primary beam, caused a severe deterioration in wire-chamber efficiency. When the event rate is high at low beam currents, the delta ray filter can be removed and advantage taken of the good hodoscope angular resolution. When it is necessary to use a current in excess of 0.5 nA these rays must be filtered if the chamber efficiency is to be preserved.

The fundamental nature of the PPB process demands a larger sample of events than that collected in previous experiments. Therefore, event rate is a primary consideration

in any new experimental approach designed to study this process in detail. In the most recent publication near this energy [29] the event rate was approximately 2 per hour. In our preliminary calibration run we identified 274 ± 17 PPB events in 6.8 hours. When the changes discussed above are fully realised an increase in this data-taking rate can be expected.

REFERENCES.

1. R.A. Arndt and M.H. McGregor, Phys.Rev. 141,875 (1966)
2. R.E.Warner, Can.J. Phys. 44,1225 (1966)
3. I. Slaus, J.W. Verba, J.R. Richardson, R.F. Carlson, W.T.H. van Oers, and L.S.August, Phys. Rev. Letters 17, 536 (1966)
4. D.L. Mason and M.L. Halbert, Phys. Rev., Vol. 176, No.4, 1159 (1968)
5. M.I.Sobel and A.H.Cromer 1963 Phys. Rev. 132, 2698
6. B. Gottschalk, W.J. Shlaer and K.H. Wang 1965 Phys. Letters, 16, 294; Nucl. Phys. 75, 549
7. K.W. Rothe, P.F.M. Koehler and E.H. Thorndike Phys.Rev. Letters 16, 1118 (1966)
8. E. Belser, G.B. Collins, J. Fischer, T. Fujii, S. Heller, W. Higinbotham, J. Menes, H. Pate, F. Turkot, N.C. Hien, IEEE Trans. Nucl.Sci. NS-12, No.4, 227 (1965)
9. J. Fischer, IEEE Trans. Nucl. Sci. NS-12 No.4, 37 (1965)
10. W.A. Higinbotham, J.F. Jacobs, H.R. Pate, IEEE Trans. Nucl. Sci. 12, No.1, 386 (1965)
11. P.T. Andrews, P. Butler, N. Cohen, A.N. James and B.G. Lowe, Nucl. Instr. and Meth. 74, 300 (1969)
12. K.G. Standing, J.J. Burgerjon and F. Konopasek, 1962 Nucl. Instr. and Meth. 18-19, 111 --------1965, IEEE Trans. Nucl. Sci. NS-12, 334
13. D.G. Peterson, Master's Thesis, Univ. of Manitoba, 1970.

14. J.C. Thompson, Technical Notes, Univ. of Manitoba Cyclotron (1968)

15. L.W. Funk, J.V. Jovanovich, R. Kawchuk, R. King, J. McKeown, C.A. Miller, D.G. Peterson, D. Reimer, K.G. Standing and J.C. Thompson, Proc. DECUS 1967 Fall Symposium, P. 187.

16. D. Reimer, J.V. Jovanovich, J. McKeown, and J.C. Thompson Proc. DECUS 1968 Spring Symposium, P. 17

17. J. McKeown, Univ. of Manitoba Cyclotron Report, 1970

18. T.W. Millar, Master's Thesis, Univ. of Manitoba 1970

19. B. Rossi, "High Energy Particles", Prentice Hall, P. 47

20. E. Fett "Methods in Subnuclear Physics", Int. Sch. of El. Part. Phys. Herceg-Novi, 1967 V.1, P. 33

21. R. Blieden, J. Menes, F. Turkot, E.W. Anderson, E. Bleser, G. Collins, R. Edelstein, N. Hieu and T. McMahon. Nucl. Instr. and Meth. 48, 177 1967.

22. W.A. Wenzel, Annual Review of Nuclear Sci. 14, 205 1964.

23. G. Charpak, L. Massonnet, Progress in Nuclear Techniques 1, 323 (1965) (North Holland Publishing Co.).

24. S. Miyamoto, Nucl. Instr, and Meth. 30, 361 (1964).

25. B.B. Rossi and K.I. Griesen, Rev. Mod. Phys. 13 (1941) 240.

26. W.H. Barkas and A.H. Rosenfeld, UCRL - 8030 Rev. (1961) 11.

27. A.F. Kuckes, R. Wilson and P.F. Cooper, Jr., Ann. Phys (N.Y.) 15, 193 (1961).

28. I. Slaus, J.W. Verba, J.R. Richardson, R.F. Carlson,

L.S. August and E.L. Peterson, Phys. Letters 23, 358 (1966)

29. M.L. Halbert and D.L. Mason, Phys. Rev. V 168, No.4, 1130-1138 (1968).

30. M.L. Halbert, private communication.

APPENDIX A.

Three Body Kinematics.

The relativistic equations for energy-momentum conservation are:

$$\vec{P}_o = \vec{P}_1 + \vec{P}_2 + \vec{P}_3 \qquad \ldots\ldots\ldots\ldots\ldots\ldots(1)$$

$$E_T = E_1 + E_2 + E_3 = E_o + M \qquad \ldots\ldots\ldots(2)$$

where E_T is the total energy, with E_o referring to the incident particle, 1 refers to the particle detected on the left side of the beam looking downstream, 2 refers to the particle detected on the right side of the beam, and 3 refers to the particle which is undetected in these experiments. M is the mass of the stationary target and suffix T refers to the total energy in the initial or final state. In a three body final state reaction there are nine degrees of freedom and the kinematics of the third particle can be determined if at least five of the independent parameters are measured experimentally.

Appendix B.1 provides details of the coordinate systems used in the experiment. It is convenient to specify the event in a spherical coordinate system with its origin at the event vertex and its polar axis coinciding with the beam direction, This is shown in Fig.A.1. Azimuthal angles are measured relative to the plane con-

Figure A.1

The notation used in the text.

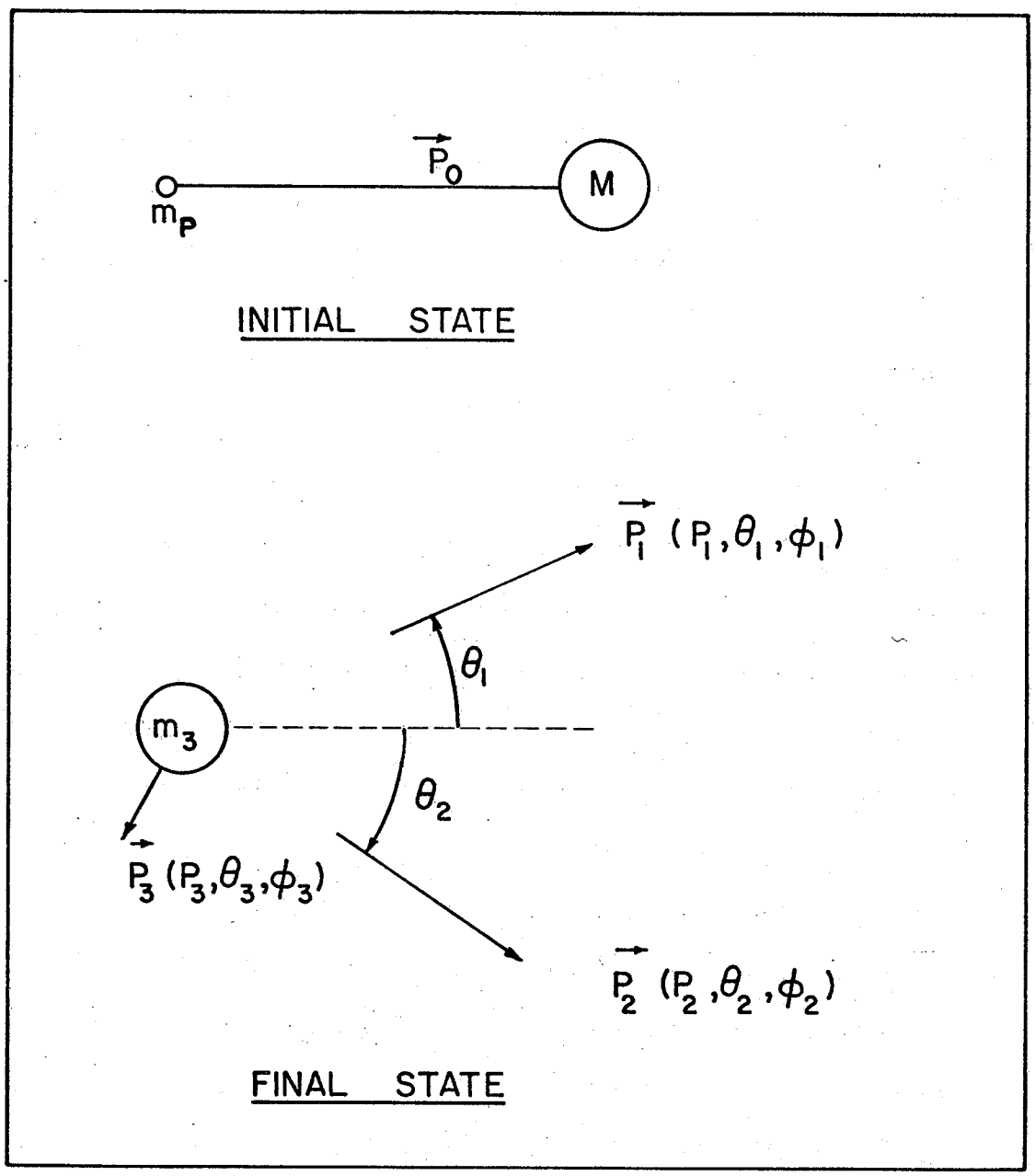
$\vec{P}_0$
M
m_P
INITIAL STATE
$\vec{P}_1$ (P_1, θ_1, ϕ_1)
θ_1
m_3
θ_2
$\vec{P}_3$ (P_3, θ_3, ϕ_3)
$\vec{P}_2$ (P_2, θ_2, ϕ_2)
FINAL STATE

taining the beam line and the centres of the hodoscope arms. The azimuthal angle, ϕ , is the angle between the median plane and the conponent of the velocity normal to the beam axis. A particle scattered to the left in the median plane has $\phi = 0$, while a particle scattered to the right in the median plane has $\phi = 180^{\circ}$. Azimuthal angles above the median plane are between 0° and 180° and angles below are between 180° and 360°.

When both detected final state particles have momentum vectors lying in a plane containing the beam axis then, $\phi_2 - \phi_1 = 180^{\circ}$, and the event is said to be coplanar. In the same way, an event in which the plane containing the beam axis and one of the detected particles but does not contain the other detected particle is said to be non-planar. The angle of non-coplanarity is given by

$$\bar{\phi} = \phi_2 - \phi_1 - 180^{\circ}$$

For PPB the relatively small amount of momentum carried away by the gamma ray imposes a limit on $\bar{\phi}$. This limit is a function of the polar angles observed. No such limit exists for the other (p,2p) reactions studied.

In component form, the momentum conservation equations are

$$P_1 \sin\theta_1 \cos\phi_1 + P_2 \sin\theta_2 \cos\phi_2 + P_3 \sin\theta_3 \cos\phi_3 = 0 \quad (3)$$

$$P_1 \sin\theta_1 \sin\phi_1 + P_2 \sin\theta_2 \sin\phi_2 + P_3 \sin\theta_3 \sin\phi_3 = 0 \quad (4)$$

$$P_1 \cos\theta_1 + P_2 \cos\theta_2 + P_3 \cos\theta_3 = P_0 \quad (5)$$

Energy conservation gives

$$\left(P_1^2 + m_1^2\right)^{\frac{1}{2}} + \left(P_2^2 + m_2^2\right)^{\frac{1}{2}} + \left(P_3^2 + m_3^2\right)^{\frac{1}{2}} = E_T \qquad (6)$$

Squaring (3) and (4) and adding we have

$$P_1^2 \sin^2\theta_1 + P_2^2 \sin^2\theta_2 + 2 P_1 P_2 \sin\theta_1 \sin\theta_2 \cos\left(\phi_1 - \phi_2\right) = P_3^2 \sin^2\theta_3 \qquad (7)$$

Also from (5)

$$\left(P_0 - P_1 \cos\theta_1 - P_2 \cos\theta_2\right)^2 = P_3^2 \cos^2\theta_3 \qquad (8)$$

Adding (6) and (7) then

$$\left(P_0 - P_1 \cos\theta_1 - P_2 \cos\theta_2\right)^2 + P_1^2 \sin^2\theta_1 + P_2^2 \sin^2\theta_2 + 2 P_1 P_2 \sin\theta_1 \sin\theta_2 \cos\left(\phi_1 - \phi_2\right) = P_3^2 \qquad (9)$$

Rearranging

$$P_0^2 + P_1^2 + P_2^2 - 2 P_0\left(P_1 \cos\theta_1 + P_2 \cos\theta_2\right) + 2 P_1 P_2\left(\cos\theta_1 \cos\theta_2 + \sin\theta_1 \sin\theta_2 \cos(\phi_1 - \phi_2)\right) = P_3^2 \qquad (10)$$

From (6)

$$\left(E_T - E_1 - E_2\right)^2 = P_3^2 + m_3^2$$

Substitution for P_3^2 gives

$$\left(E_0 + M - E_1 - E_2\right)^2 = E_T^2 + E_1^2 + E_2^2 - 3m_p^2 + m_3^2 - 2\left(E_0^2 - m_p^2\right)^{\frac{1}{2}} \left[\left(E_1^2 - m_p^2\right)^{\frac{1}{2}} \cos\theta_1 + \left(E_1^2 - m_p^2\right)^{\frac{1}{2}} \cos\theta_2\right] + 2\left(E_1^2 - m_p^2\right)^{\frac{1}{2}} \left(E_2^2 - m_p^2\right)^{\frac{1}{2}} \left[\cos\theta_1 \cos\theta_2 + \sin\theta_1 \sin\theta_2 \cos\left(\phi_1 - \phi_2\right)\right]$$

This equation is a relativistic equation of second order in the energy of one of the outgoing particles and may be solved numerically to give the allowed kinematic loci of the energies of the two final state protons.

Figure A.2

Kinematic curves of some (p,2p) reactions at an incident proton energy of 45 MeV. The closed curves are for the PPB reaction at various polar scattering angles (shown in pairs in the figure). The number close to each curve is the angle of non-coplanarity, ϕ.
The diagonal curves are for symmetric polar scattering angles of 30° and $\phi = 0$.

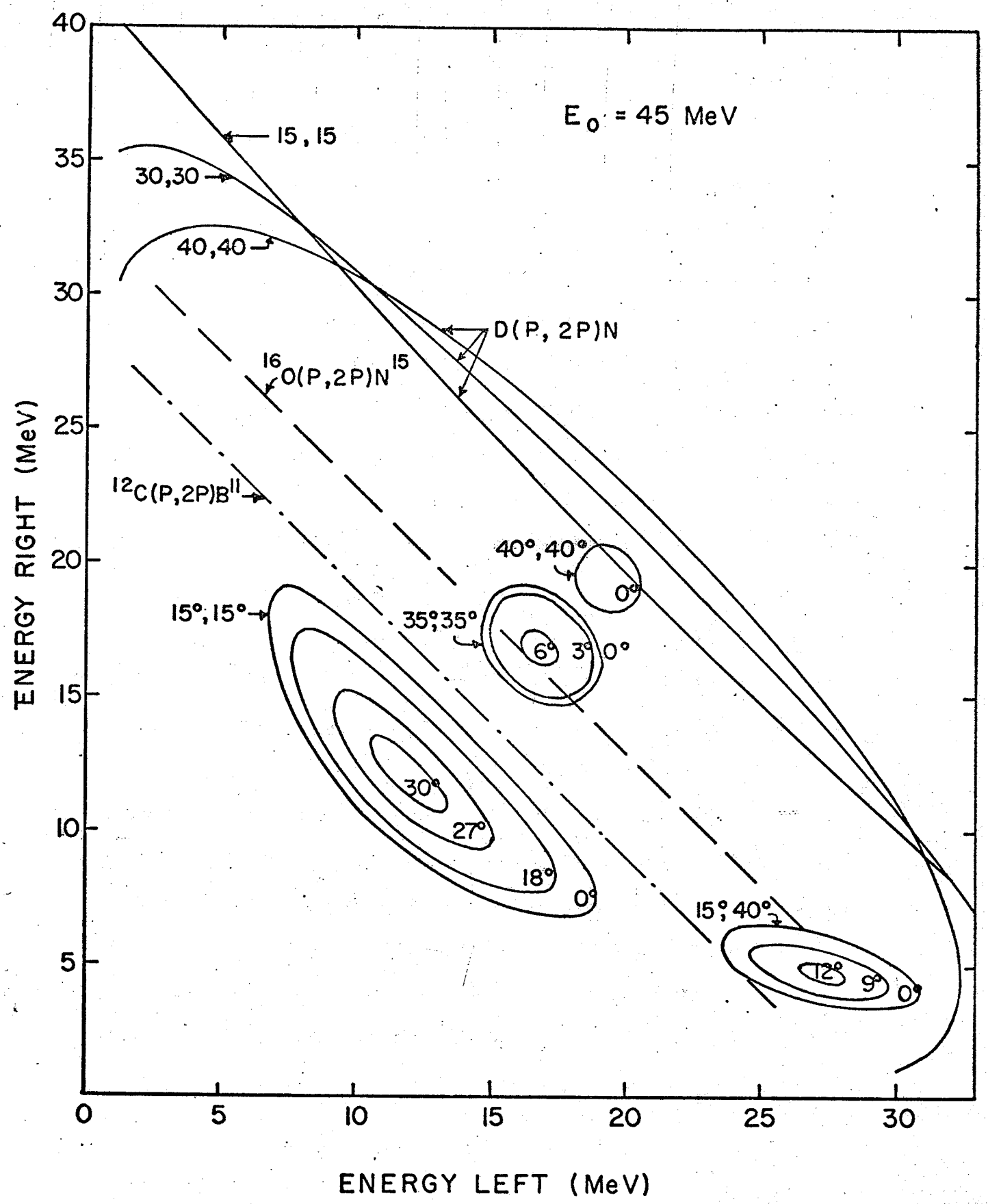
E_0 = 45 MeV
15, 15
30,30
40,40
D(P, 2P)N
^{16}O(P,2P)N^{15}
^{12}C(P,2P)B^{11}
40°,40°
0°
15°,15°
35°,35°
6°
3°
0°
30°
27°
18°
0°
15°,40°
12°
9°
0°
ENERGY RIGHT (MeV)
ENERGY LEFT (MeV)
0
5
10
15
20
25
30
35
40

In Fig.A.2 some typical solutions are given for coplanar events from the reactions $D(p,2p)N$, $^{16}O(p,2p)N^{15}$ and $C^{12}(p,2p)B^{11}$ to the ground state of the third particle and for coplanar and non-coplanar PPB events. Solutions exist for PPB only for a restricted range of proton energies. In this range with one proton energy fixed, say E_1, the energy of the other proton, E_2, is always double valued. If these two values of E_2 are plotted as a function of E_1 a smooth closed curve is obtained. For the reaction $D(p,2p)N$, E_2 is always either a single valued or a double valued function of E_1. In this experiment whenever E_2 was double valued the lower energy E_2^- was below the detection threshold of the scintillation counters. Therefore, all measurements reported in this thesis for this reaction represents either the larger of the two possible values of E_2 (when E_2 is double valued) or the unique value of E_2 (when E_2 is single valued).

For PPB the outermost curve is coplanar and the inner curves have been drawn for varying angles of non-coplanarity. Here each point on the curve specifies a unique gamma ray energy and direction. Only in the coplanar case will the range of θ_γ extend over the full range between 0° and 180°, the range falling off as $\bar{\phi}$ increases until a unique value is obtained at the kinematic limit.

APPENDIX B.

Geometric Calculations used in Analysis.

B.1 Definition of Coordinate Systems.

The geometry for the spectrometer shown schematically in Fig.B.1 is specified in four coordinate frames namely :-

(i) the left hodoscope frame L_1, L_2, L_3.

(ii) the right hodoscope frame R_1, R_2, R_3.

(iii) the beam cartesian frame X,Y,Z.

(iv) the spherical coordinate frame.

Frames (i) and (ii) are right angled coordinate frames having one axis normal to the plane of the wire chambers and (iii) is a conventional cartesian system with one axis in the beam direction. The cartesian frames have a common origin but the event vertex is chosen as the origin for the spherical coordinate system.

Practical considerations govern this choice of representation for the spectrometer geometry. After the multiplicities (the number of adjacent cores flipped per spark) are extracted, the proton trajectories are calculated at PDP-9 level directly from wire numbers. It is natural therefore, that the central plane of the wire chamber should form two axes of a coordinate frame R_1, R_2, R_3 (for the right arm) such that R_1 and R_2 are the horizontal and vertical coordinates and R_3 is the normal to the plane

Figure B.1

Representation of the cartesian coordinate systems and notation used in Appendix B. to describe the geometric calculations performed by the VERTEX and KINEMATICS programs.

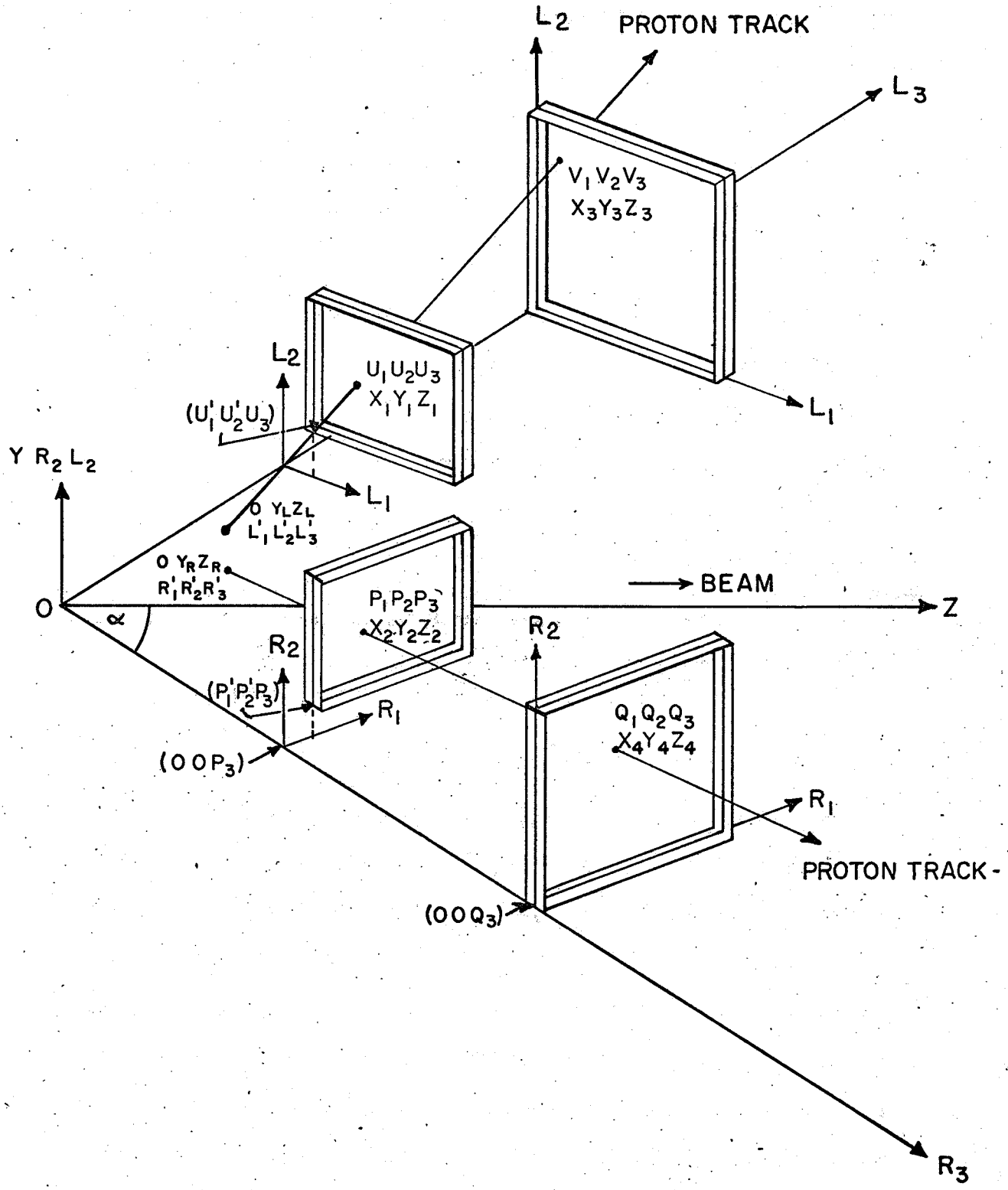
L2
PROTON TRACK
L3
V1 V2 V3
X3 Y3 Z3
L2
U1 U2 U3
X1 Y1 Z1
(U'1 U'2 U'3)
L1
Y R2 L2
O YL ZL
L'1 L'2 L'3
L1
O YR ZR
R'1 R'2 R'3
BEAM
O
α
Z
P1 P2 P3
X2 Y2 Z2
R2
R2
(P'1 P'2 P'3)
R1
Q1 Q2 Q3
X4 Y4 Z4
(00P3)
R1
PROTON TRACK
(00Q3)
R3

of the chamber passing through the origin of the rear wire chamber. This origin is taken to be 0.025"(one half wire spacing) outside the end wire appropriate to the plane origin considered. The common origin for the cartesian frames is the point of intersection of the ordinates L_3 and R_3 which for a symmetric system will be in the plane of the beam. The origin of the cartesian frame is therefore dependent on the position of the rear chamber. As shown in Fig.B.1 the coordinates of the origins of the front chambers (P_1', P_2') and (U_1', U_2') will in general be non-zero and will change when the rear chambers are translated in order to change the angular range. It is necessary therefore, to initialise the VERTEX program with the constants $P_1', P_2', U_1', U_2', P_3, Q_3, U_3$ and P_3 for the particular geometry in use.

B.2 Calculations in the VERTEX Program.

The PDP-9 VERTEX program reconstructs the particle trajectories in the hodoscope frames and tests for an event vertex in a beam cartesian frame. As the program is written in machine language the practical range of calculations is necessarily restricted. If the beam is defined to pass in a positive Z direction and the Y axis is vertical, then for an infinitely thin beam the event must originate in the Y-Z plane. Let the coordinates of this point be R_1', R_2', R_3' in the right hodoscope frame

and $(0, Y_R, Z_R)$ in the beam frame. Then, using the notation defined by Fig.B.1 the equation for the proton trajectory is

$$\frac{R_1' - P_1}{Q_1 - P_1} = \frac{R_2' - P_2}{Q_2 - P_2} = \frac{R_3' - P_3}{Q_3 - P_3} \qquad \ldots\ldots\ldots(1)$$

As R_1' lies on the Y-Z plane

$$R_3' = Z_R \cos\alpha$$

$$R_1' = R_3 \tan\alpha$$

$$R_2' = Y_R$$

Substitution into equation (1) and eliminating R_1, R_2 and R_3 gives

$$Z_R = \frac{P_1 Q_3 - P_3 Q_1}{\left[(Q_3 - P_3)\tan\alpha - (Q_1 - P_1)\right]\cos\alpha}$$

and

$$Y_R = \frac{(P_1 Q_3 - P_3 Q_2)\tan\alpha + (P_1 Q_2 - P_2 Q_1)}{\left[(Q_3 - P_3)\tan\alpha + P_1 - Q_1\right]}$$

Similarily consideration of the points in the left co-ordinate frame yields intercepts given by

$$Z_L = \frac{U_1 V_3 - U_3 V_1}{\left[(V_3 - U_3)\tan\alpha - (V_1 - U_1)\right]}$$

$$Y_L = \frac{(U_1 V_3 - U_3 V_2)\tan\alpha + (U_1 V_2 - U_2 V_1)}{\left[(V_3 - U_3)\tan\alpha + U_1 - V_1\right]}$$

The vertical vertex error ΔY is then defined to be

$$\Delta Y = Y_L - Y_R$$

and the horizontal vertex error ΔZ is defined to be

$$\Delta Z = Z_L - Z_R$$

B.3 Calculations in the Kinematics Programs.

Only the spark coordinates of events which pass the coarse vertex demand of the VERTEX program are sent to the kinematics program. It is a relatively simple matter to transform these points in space into the beam cartesian frame before specifying each event in a spherical coordinate system. Using odd subscripts for the left track and affecting a rotation, α, about the Y axis (see Fig.B.1), the coordinates in the front chamber (X_1, Y_1, Z_1) and the rear chamber (X_3, Y_3, Z_3) for the left track are given by

$$X_1 = U_3 \sin\alpha - U_1 \cos\alpha$$
$$Y_1 = U_2$$
$$Z_1 = U_3 \cos\alpha - U_1 \sin\alpha$$
$$X_3 = V_3 \sin\alpha \quad V_1 \cos\alpha$$
$$Y_3 = V_2$$
$$Z_3 = V_3 \cos\alpha + V_1 \sin\alpha$$

The equation for the left proton trajectory is

$$\frac{X_0 - X_1}{X_3 - X_1} = \frac{Y_0 - Y_1}{Y_3 - Y_1} = \frac{Z_0 - Z_1}{Z_3 - Z_1} = \eta$$

hence the intercept with Y-Z plane has coordinates (Y_L, Z_L) given by

$$Y_L = X_1 (Y_1 - Y_3) / (X_3 - X_1) + Y_1$$

$$Z_L = X_1 (Z_1 - Z_3) / (X_3 - X_1) + Z_1$$

where the suffix O(odd) refers to the left track and L indicates that these coordinates give the intercept of the left track in the Y-Z plane.

Using even values of subscripts for the right track the proton trajectory is given by

$$\frac{X_E - X_2}{X_4 - X_2} = \frac{Y_E - Y_2}{Y_4 - Y_2} = \frac{Z_E - Z_2}{Z_4 - Z_2} = \tau$$

and the intercepts with the Y-Z plane are given by

$$Y_R = X_2 (Y_2 - Y_4) / (X_4 - X_2) + Y_2$$

and

$$Z_R = X_2 (Z_2 - Z_4) / (X_4 - X_2) + Z_2$$

The two dimensional vertex errors are then defined as in subsection B.2 to be

$$\Delta Y = Y_L - Y_R$$

and

$$\Delta Z = Z_L - Z_R$$

A three dimensional vertex point is calculated by minimising the distance, d, between the lines.

We have

$$d^2 = (X_O - X_E)^2 + (Y_O - Y_E)^2 + (Z_O - Z_E)^2$$

and we have a vertex when

$$\frac{d\,(d^2)}{d\,\eta} = \frac{d\,(d^2)}{d\,\tau} = 0$$

Solution of this differential equation gives

$$\eta = \frac{DB + EC}{C^2 - AB}$$

$$\tau = \frac{EA + DC}{C^2 - AB}$$

where

$$A = (X_3 - X_1)^2 + (Y_3 - Y_1)^2 + (Z_3 - Z_1)^2$$

$$B = (X_4 - X_2)^2 + (Y_4 - Y_2)^2 + (Z_4 - Z_2)^2$$

$$C = (X_3 - X_1)(X_4 - X_2) + (Y_3 - Y_1)(Y_4 - Y_2) + (Z_3 - Z_1)(Z_4 - Z_2)$$

$$D = (X_3 - X_1)(X_1 - X_2) + (Y_3 - Y_1)(Y_1 - Y_2) + (Z_3 - Z_1)(Z_1 - Z_2)$$

$$E = (X_4 - X_2)(X_2 - X_1) + (Y_4 - Y_2)(Y_2 - Y_1) + (Z_4 - Z_2)(Z_2 - Z_1)$$

The coordinates $({}_3X_L, {}_3Y_L, {}_3Z_L)$ of the left track at the minimum distance are

$${}_3X_L = \eta\,(X_3 - X_1) + X_1$$

$${}_3Y_L = \eta\,(Y_3 - Y_1) + Y_1$$

$${}_3Z_L = \eta\,(Z_3 - Z_1) + Z_1$$

and the coordinates $({}_3X_R, {}_3Y_R, {}_3Z_R)$ of the right track at the minimum distance are

$${}_3X_R = \eta\,(X_4 - X_2) + X_2$$

$$ {}_3Y_R = \eta\,(Y_4 - Y_2) + Y_2 $$
$$ {}_3Z_R = \eta\,(Z_4 - Z_2) + Z_2 $$

The three dimensional vertex errors are defined by

$$ \Delta_3 X = {}_3X_L - {}_3X_R $$
$$ \Delta_3 Y = {}_3Y_L - {}_3Y_R $$
$$ \Delta_3 Z = {}_3Z_L - {}_3Z_R $$

and these can be combined to give a composite 3 dimensional vertex error, ΔV_3, defined by the equation

$$ \Delta V_3 = \left(\Delta_3 X^2 + \Delta_3 Y^2 + \Delta_3 Z^2\right)^{\frac{1}{2}} $$

The equations used to determine the direction of the proton trajectories in a spherical coordinate system with the event vertex as the origin are as follows :-

$$ \theta_1 = \tan^{-1}\left\{\left[X_3^2 + (Y_3 - Y_L)^2\right]^{\frac{1}{2}} \Big/ (Z_3 - Z_L)\right\} $$
$$ \theta_2 = \tan^{-1}\left\{\left[X_4^2 + (Y_4 - Y_R)^2\right]^{\frac{1}{2}} \Big/ (Z_4 - Z_R)\right\} $$
$$ \phi_1 = \tan^{-1}\left[(Y_3 - Y_1) \Big/ (X_3 - X_1)\right] $$
$$ \phi_2 = \tan^{-1}\left[(Y_4 - Y_2) \Big/ (X_4 - X_2)\right] $$
$$ \bar{\phi} = \phi_2 - \phi_1 - \pi $$

APPENDIX C

Determination of the momentum and the error in the momentum of the third particle.

From conservation of momentum, the momentum components of the third final state particle are

$$P_{3x} = -(P_{1x} + P_{2x})$$

$$P_{3y} = -(P_{1y} + P_{2y})$$

$$P_{3z} = P_0 - (P_{1z} + P_{2z})$$

where

$$P_{1x} = P_1 \sin\theta_1 \cos\phi_1 \qquad P_{2x} = P_2 \sin\theta_2 \cos\phi_2$$

$$P_{1y} = P_1 \sin\theta_1 \cos\phi_1 \qquad P_{2y} = P_2 \sin\theta_2 \sin\phi_2$$

$$P_{1z} = P_1 \cos\theta_1 \qquad P_{2z} = P_2 \cos\theta_2$$

The momentum, P_3, of the third particle is then given by

$$P_3 = \left[P_{3x}^2 + P_{3y}^2 + P_{3z}^2\right]^{\frac{1}{2}}$$

The error in the momentum of the third particle (see section 3.3(b) is given by

$$\Delta P_3^2 = \left(\frac{\partial P_3}{\partial E_1}\right)^2 \Delta E_1^2 + \left(\frac{\partial P_3}{\partial E_2}\right)^2 \Delta E_2^2 + \left(\frac{\partial P_3}{\partial \theta_1}\right)^2 \Delta \theta_1^2 + \left(\frac{\partial P_3}{\partial \theta_2}\right)^2 \Delta \theta_2^2$$

$$+ \left(\frac{\partial P_3}{\partial \phi_1}\right)^2 \Delta \phi_1^2 + \left(\frac{\partial P_3}{\partial \phi_2}\right)^2 \Delta \phi_2^2 + \left(\frac{\partial P_3}{\partial E_0}\right)^2 \Delta E_0^2 \quad \ldots\ldots(1)$$

Each partial derivative in equation (1) may be factorised into momentum components :-

$$\frac{\partial P_3}{\partial V_i} = \frac{1}{P_3}\left(P_{3x}\frac{\partial P_{3x}}{\partial V_i} + P_{3y}\frac{\partial P_{3y}}{\partial V_i} + P_{3z}\frac{\partial P_{3z}}{\partial V_i}\right) \quad \ldots\ldots(2)$$

Evaluation of the 'x' component of momentum for the third particle gives

$$P_{3x} = -\left(P_1 \sin\theta_1 \cos\phi_1 + P_2 \sin\theta_2 \cos\phi_2\right)$$

$$= -\left(E_1^2 - m_1^2\right)^{\frac{1}{2}} \sin\theta_1 \cos\phi_1 - \left(E_2^2 - m_2^2\right)^{\frac{1}{2}} \sin\theta_2 \cos\phi_2$$

Then

$$\frac{\partial P_{3x}}{\partial E_1} = -\frac{E_1}{P_1} \sin\theta_1 \cos\phi_1$$

Similar evaluation of the other components give the following equations for dependent variables of the left particle.

$$\frac{\partial P_{3y}}{\partial E_1} = -\frac{E_1}{P_1} \sin\theta_1 \sin\phi_1$$

$$\frac{\partial P_{3z}}{\partial E_1} = -\frac{E_1}{P_1} \cos\theta_1$$

$$\frac{\partial P_{3x}}{\partial E_0} = 0$$

$$\frac{\partial P_{3x}}{\partial \theta_1} = -P_1 \cos\theta_1 \cos\phi_1$$

$$\frac{\partial P_{3y}}{\partial \theta_1} = -P_1 \cos\theta_1 \sin\phi_1$$

$$\frac{\partial P_{3z}}{\partial \theta_1} = P_1 \sin\theta_1$$

$$\frac{\partial P_{3x}}{\partial \phi_1} = P_1 \sin\theta_1 \sin\phi_1$$

$$\frac{\partial P_{3y}}{\partial \phi_1} = -P_1 \sin\theta_1 \cos\phi_1$$

$$\frac{\partial P_{3z}}{\partial \phi_1} = 0$$

Equations for the partial derivatives of the variables specifying the particle on the right side of the beam are found in the same way.

If ΔE_o, ΔE_1, ΔE_2, $\Delta \theta_1$, $\Delta \theta_2$, $\Delta \phi_1$ and $\Delta \phi_2$ are determined experimentally then substitution of the calculated partial derivatives into equation (1) will yield the expected error in the momentum of the third particle.